Numerical Studies of Spray Atomization for Multiphase Flows

Fakhar Abbas

School of Aerospace, Mechanical and Mechatronic Engineering
Faculty of Engineering and IT
The University of Sydney

A thesis submitted in fulfilment of the requirements for the degree of
Doctor of Philosophy

2023

I would like to dedicate this thesis to my loving parents, sisters, wife and daughter...

Statement of Originality

I certify that the intellectual content of this thesis is the product of my own work and that all the assistance received in preparing this thesis and sources have been acknowledged. This thesis does not include a substantial part of the work that has been submitted as a requirement for any other degree in any university or educational institution.

Fakhar Abbas
2023

Authorship Attribution Statement

For the preparation of this document, previously published works are used in some chapters.

- The contents of some sections of Chapters 1, 2, 3 and 4 of this thesis are published as:

  Abbas, F., Wang, B., Cleary, M., Masri, A. (2021). Numerical convergence of volume of fluid based large eddy simulations of atomizing sprays. Physics of Fluids, 33(4), 42119.

  Abbas, F., Tretola, G., Cleary, M., Navarro-Martinez, S., Masri, A. (2020). On the use of LES-PDF form of the Eulerian-Lagrangian Spray Atomisation (ELSA) model to simulate air blast atomisation. 12th Asia-Pacific Conference on Combustion (ASPACC 2019), Fukuoka: The Combustion Institute.

  Abbas, F., Tretola, G., Cleary, M., Navarro-Martinez, S., Masri, A. (2019). Grid Sensitivity Study for Air Blast Atomisation Using an LES-PDF form of ELSA Model. Australian Combustion Symposium 2019, Sydney: The Combustion Institute Australia & New Zealand.

  I performed all the simulations and analysed the results included in this thesis. I contributed to extending the existing code's applicability and wrote the manuscript for the associated sections.

- The main body of Chapter 5 is published as:

  Abbas, F., Wang, B., Cleary, M., Masri, A. (2021). Numerical convergence of volume of fluid based large eddy simulations of atomizing sprays. Physics of Fluids, 33(4), 42119.

  I performed all the simulations, analysed the results and prepared the manuscript.

Fakhar Abbas
2023

Acknowledgements

This Thesis would not have been possible without the support of many people. First, I would like to thank my supervisors, A/Prof. Matthew Cleary and Prof. Assaad Masri for their outstanding and encouraging support and continuous supervision throughout this study. I cannot thank them enough for their guidance and help in overcoming the difficulties that arose while working on this project. Both have taught me the value of a well structured approach to science and the importance of collaboration to advance science. I am indebted for the opportunities to interact in international settings and share and learn from other researchers working in similar research areas.

I am also grateful to Dr Salvador Navarro-Martinez for sharing his LES-PDF code and expert guidance for the in-depth analysis. I would also appreciate the continuous support of Dr Giovanni Tretola and Dr Sebastian Galindo Lopez for the valuable discussions over time. I would also like to take the opportunity to thank Dr Bosen Wang for all his support and code development while working on the same project. I also owe a great deal to all other members of our research group for having a wonderful and memorable time together.

None of this would have been possible without the love and support of my family, especially my parents and wife. Thanks for their patience and unconditional encouragement when things were not going as expected and taking more time. I could not ask for better parents and a better life partner.

Finally, I acknowledge the financial support provided by the Australian Research Council (DP180104190). I am also grateful for the use of HPC facilities at the University of Sydney.

Abstract

The current study aims to investigate and develop numerical tools for the simulation of interfacial flows, including those with turbulence and primary spray atomization. In the past, many approaches were developed to track the interface of a multi-phase/immiscible flow system. Two of them, the volume of fluid (VoF) and the level set (LS), have shown promising findings and have been considered a benchmark for further research. VoF methods have proved good mass conservation behaviour during the advection of solution. However, LS methods have shown better interface representation when used for the calculations of interfacial flows. Most of the recent development in this context either originated from VoF, LS or a combination of both.

In the first part of this thesis importance of the current study is highlighted in detail, and an overview of the recent developments for the numerical solutions of immiscible flows is presented. A detailed description of interface-capturing methods and their development over time is presented in a systematic way, leading to the issues addressed in this study. A stochastic field PDF-LES solution of the VoF approach is analyzed against the Sydney needle spray measurements. Solution behaviour for different combinations of stochastic fields and LES grid cells are examined in detail.

In the second part of this work, three different LES treatment for unresolved sub-grid fluctuations, TFVoF, TF-AC and newly developed EVD, has been presented. The performance analysis of two already existing solutions, TFVoF and TF-AC, is compared with the EVD approach. Sydney needle spray measurements are used as a benchmark for this comparison. The suitability of the EVD approach is also tested for different flow conditions. Simulation results confirm that sub-grid surface tension plays an important role in the realistic prediction of the jet decay rate, and proper closure models to account for sub-grid surface tension are very necessary. An already existing sub-grid surface tension closure model is incorporated into OpenFOAM and tested for all three LES filtered solutions.

The findings of this work suggest that the newly developed EVD approach has shown promising improvements to produce more reliable and realistic solutions for multi-phase flow applications. Sub-volume surface tension closure model, following the EVD formulation, is helpful for more accurate jet decay rate predictions.

Table of Contents

List of Figures

List of Tables

Nomenclature

Acronyms

ACLS	Accurate Conservative Level Set
ALE	Arbitrary Lagrangian-Eulerian
AMR	Adaptive Mesh Refinement
CFL	Courant-Friedrich-Levy
CICSAM	Compressive Interface Capturing Scheme for Arbitrary Meshes
CLS	Conservative Level Set
CLSVOF	Coupled Level Set Volume of Fluid
CSF	Continuum Surface Force
DI	Diffuese-interface
DIC	Diagonal Incomplete-Cholesky
DICGaussSeidel	Diagonal Incomplete-Cholesky with Gauss-Seidel
DILU	Diagonal Incomplete-LU
DNS	Direct Numerical Simulation
ELSA	Eulerian-Lagrangian Spray Atomization
EVD	Explicit Volume Diffusion
FCT	Flux-corrected Transport
FMM	Fast Marching Method

FSM	Fast Sweeping Method
FSP	Flame Spray Pyrolysis
GAMG	Geometric-algebraic Multi-grid
GCI	Grid Convergence Index
GIV	Gaseous Image Velocimetry
HPLC	Hybrid Particle Level Set
ICM	Interface-capturing Mechanism
LDV	Laser Doppler Velocimeter
LES	Large Eddy Simulations
LS	Level Set
MAC	Marker and Cell
MEMS	Micro-electromechanical Systems
MULES	Multidimensional Universal Limiter for Explicit Solution
OpenFOAM	Open source Field Operation And Manipulation
OPLS	One-layer Partivle Level Set
PBiCG	Pre-conditioned Bi-conjugate Gradient
PCG	Pre-conditioned Conjugate Gradient
PDE	Partial Differential Equation
PDF	Probability Density Function
PIMPLE	Combination of both PISO and SIMPLE
PISO	Pressure-implicit Split Operator
PLIC	Piecewise-Linear Interface Calculation
PLS	Particle Level Set
RANS	Reynolds-averaged Navier-Stokes

RCLS	Robust Conservative Level Set
RLSG	Refined Level Set Grid
SDE	Stochastic Differential Equations
SIMPLE	Semi-implicit Method for Pressure-linked Equations
SLIC	Simple Line Interface Calculation
SMD	Sauter Mean Diameter
SPDE	Stochastic Partial Differential Equations
SPH	Smoothed Particle Hydrodynamics
TF-AC	Tturbulence Filtering and Artificial Compression
TFVoF	Turbulent Filtered Volume of Fluid
THINC-SW	Tangent of Hyperbola for Interface Capturing with Slope Weighting
TVD	Total Variation Diminishing
VoF	Volume of Fluid
WENO	Weighted Essentially Non-oscillatory

Greek Upper-case

Δ	LES filter size
Γ	Phase indicator function
Λ	Taylor microscale
Φ_f	Volumetric flux
Ψ	Interface smooth function
Σ	Surface density
Σ_{eq}	Equilibrium surface density
Σ_{min}	Minimum surface density

Greek Lower-case

κ	Interface curvature
α	Liquid volume fraction
δ^l	Fine-grained surface density
δ_g	Vorticity layer thickness
δ_s	Interface detecting function
δ_{ij}	Dirac Delta function
ε	Rate of energy dissipation
λ_{KH}	Kelvin-Helmholtz unstable wavelength
λ_{KH}	Rayleigh-Taylor unstable wavelength
μ	Dynamic viscosity
μ_g	Dynamic viscosity of gas
μ_l	Dynamic viscosity of liquid
ν_V	Explicit volume viscosity
ν_{sgs}	Sub-grid turbulent viscosity
ψ	Conservative level set function
ρ	Mixture density
ρ_g	Gas density
ρ_l	Liquid density
σ	Coefficient of surface tension force
τ	Turbulent time scale
τ_{ij}^{va}	Sub-volume stress
τ_{ij}	Viscous stresses
θ_1	Sample space vector for α
θ_2	Sample space vector for Σ

ε	Interface's thickness controlling factor
φ	Level Set function
ξ	Boundary layer thickness

Roman Upper-case

$\tau_{i,j}^{va}$	sub-volume stress
B	Sample space for the random variable α
C_{α}	Switching parameter
$C_{\alpha u}$	Modelling constant following EVD solution
C_{comp}	Scalar compression factor
C_{sf}	Modelling constant for sub-volume surface tension
C_{SL}	Smagorinsky-Lilly model constant
Co_f	Flow Courant number
Co_i	Interface Courant number
D	Air-blast diameter
D_f	Fractal dimension of the interface
D_g	Gas flow diameter
D_l	Liquid flow diameter
D_v	Explicit volume diffusion coefficient
D_{sgs}	Sub-grid diffusivity
E	Magnitude of a velocity gradient tensor
$F_{s,i}$	Surface tension force in ith direction
G	Spatial filter function
H	Heaviside function
IRQ_{κ}	Continuous interface indicator

J	Onsanger kinetic coefficient
$J^{tf}_{\alpha,i}$	sub-grid flux
$J^{va}_{\alpha,i}$	sub-volume flux
L	Represents differential operator
Oh	Ohnesorge number
P_{α}	PDF of volume fraction
$P_{\alpha,u}$	Joint PDF of volume fraction and velocity
P_{sgs}	Sub-grid joint probability density function
Q	Second invariant of the velocity gradient tensor
Re_{τ}	Turbulent Reynolds number
Re_g	Gas flow Reynolds number
Re_l	Liquid flow Reynolds number
S_d	Surface destruction
S_f	Outward-pointing cell face area vector
S_g	Generation of surface density
S_g	Surface generation
S_{ij}	Strain-rate tensor
Sc_t	Turbulent Schmidt number
T	Temperature
V	Volume
We	Weber number
We^*	Critical Weber number
We_h	Local Weber number
$We_{h,crt}$	Critical mesh Weber number

W_{ij}	Vorticity tensor

Roman Lower-case

C_{sharp}	Interface sharpening coefficient
d	Shortest distance to the free surface
d_j	Liquid jet diameter
dW^a	Wiener processes
g_i	Gravitational acceleration in *i*th direction
k	Kinetic energy
k_t	Turbulent kinetic energy
l_τ	Sub-grid length scale
l_t	Turbulent length scale
l_V	Physical volume length scale
n_i	Unit normal vector
p_g	Pressure values for quiescent air
p_{vap}	Pressure values for saturated vapours
t	Time
u_g	Gas velocity
u_i	Velocity in *i*th direction
u_j	Velocity in jth direction
u_l	Liquid velocity
u_r	Relative velocity
u_i'	Interface velocity
x_i	Spatial coordinate in *i*th direction

Superscripts

I	Evaluation at the liquid-gas interface
tf	Sub-grid component due to the filtering of turbulent fluctuations
va	Volume averaged

Subscripts

bkp	Break-up
col	Collision
den	Dense
f	Flow
g	Gas
i	Interface
l	Liquid

Operators

$\bar{\cdot}$	Conventional Reynolds or spatial filtering
∇	Spatial Gradient
∂	Partial derivative
$\sum$	Summation operator
$\widehat{\cdot}$	Reynolds volume averaging
$\widetilde{\cdot}$	Density weighted volume averaging
CIF	Cauchy's Integral Formula

Chapter 1

Introduction

Interfacial flows with moving free surfaces can be divided into different sub-categories like atomizing spray jets, bubbly flows, waves and liquid films. Each class has several physical real-life applications, e.g., liquid sprays play an essential role in automobile, power and manufacturing sectors; characteristics of liquid bubbles are important in various chemical applications; ocean waves are important in the design of maritime vessels and coastal structures; liquid films are significant in printing and coating industries. All these applications involve the interaction of the liquid with gas or air. Usually, experimental findings are considered the leading source of the necessary information regarding these two-fluid interactions. However, experimental investigations become challenging or sometimes impossible when the time and length scales are microscopic, or the conditions are too dangerous or expensive to replicate in a laboratory. Under these conditions, numerical modelling is the only option for the desired qualitative or quantitative physical analysis.

Spray jets can be nominally divided into three main regions [87, 91, 286, 259]:

(i) the dense, near-field, primary atomization region that can be treated as an interfacial flow with continuous liquid and gas streams that are unambiguously separated by an interface

(ii) the intermediate region where the liquid jet continues to break-up along with secondary atomization of discrete fragments

(iii) the far-field region where the spray becomes dilute.

The current study focuses on the dense and intermediate regions and therefore addresses two-phase flow conditions in which both interfacial and discrete flow conditions co-exist. Different approaches are available to have the solution of moving interfaces such as volume of fluid (VoF) [107], level set (LS) [251] and diffuse-interface (DI) [11]. The VoF based solutions have performed well in terms of mass conservation but remain sensitive to mesh resolution, which is a key challenge with these methods. Although fully resolved solutions with VoF are helpful in getting the fundamental insight [59, 102] the high computational requirement does not allow them for full-scale practical flows. Under resolved solutions such as large eddy simulations (LES) in combination with VoF have been applied in various studies [144, 46, 12]. In the present work, the performance analysis of two already existing approaches including the turbulent filtered VoF model (TFVoF) [144, 46] and a hybrid turbulence filtering and artificial compression model (TF-AC) [12] is conducted against a new explicit volume diffusion model (EVD) [270]. The three approaches are distinguished by different modelling strategies of unresolved fluctuations at the liquid-air interface of a two-phase flow. In general, these fluctuations can be due to interface dynamics and turbulence. All these treatments properly considered the large jumps of liquid density and viscosity across the interface to have the correct momentum balance in the interface region. As the surface tension force is significant and plays a crucial role in interface dynamics, its sub-grid effects are evaluated in detail. A new sub-grid surface tension model is also incorporated with OpenFOAM, and its results are analyzed and compared. Stochastic field solution coupled with turbulent filtered combined VoF and surface density model [184] is also evaluated for different numbers of stochastic fields.

1.1 Motivation

Atomization processes are widely used in various applications and play a vital role in driving the current modern society. They are very valuable and extensively used in the power, transportation and industrial sectors, i.e., engines and gas turbines, agriculture, nanomaterials [157] and medical [182] industries. According to the World Energy Outlook of 2017 [2], the central part of energy consumption is based on fossil fuels with a contribution of over 74%. Moreover, energy requirements continue to increase with an annual increment of around 2%. The principal constituent of this primary energy source is oil, along with coal and gas [1, 3]. Increasing focus on environmental sustainability encourages devices with a better design that have progressively higher efficiency and clean emissions. The increased utilization of renewable sources for energy requirements put extra pressure on these devices to be more environmentally friendly and energy-efficient [2]. In addition to theoretical interests in the physics involved behind the generation of these instabilities when the liquid-gas interaction comes into place, knowledge of primary atomization is fundamental in analyzing the spray phenomenon, droplet sizes and their distribution involved in various applications like propulsion devices, power generations, liquid metals, agricultural sprays, printing and food industry. This is a key element for the researchers to focus further both on the experimental and theoretical aspects of the atomization phenomenon.

The central focus of current research is to understand better the atomization phenomenon that can lead to better atomization devices. For example, in the field of combustion, better injection of liquid fuel can help reduce its impacts on the environment with the increased efficiency of fuel used. Concerning the contribution of combustions devices to the atmosphere and energy resources, a lot of focus is on redefining the design of devices to achieve fewer pollutant emissions and reduce fuel consumption by increasing their efficiency. In many combustion devices, fuel is directly injected into the combustion chamber. This could be done by forcing fuel into stagnant high-pressure air or injecting the liquid fuel comparatively flowing at a lower speed into high-speed co-flowing air. In both cases, the fluid injection process is of prime importance in the combustion sequence to have better control and clean combustion products. Liquid sprays are also helpful for the scalable synthesis of nanomaterials under the flame spray pyrolysis (FSP) [157] approach, which has been considered a preferred manufacturing route for the production of a wide range of products such as metal oxides, salts and metals [247] using metal-nitrates. These nanoparticles are of much importance to the industry because of having exceptionally promising potential for manufacturing catalysts, smart sensors, biomaterials and biomedical devices. Liquid evaporation and the rate of air mixing highly depend on the injection phenomenon. By a well-defined injection system, we can control the droplet sizes of liquid fuel and their distribution in the combustion chamber, which will help to investigate their effect on the combustion process. To optimize a complex turbulent injection system, reliable lower-order models are necessary. So far, these models are not capable enough because of the unavailability of comprehensive theoretical background related to primary atomization. Recent developments [271] in the X-ray techniques are helpful in capturing the near-field data but still struggling to overcome the complexity of mounting the high-pressure chamber inside the X-ray unit. Also, this technology is still costly and not within reach of most of the combustion research community. Considering all these limitations, numerical simulations can play a better role in investigating the near-field region of primary atomization. These are helpful in providing information related to the dense part of the fuel jet, for which limited experimental data is available so far.

The development of accurate and affordable spray atomization models is essential given the ubiquitous use of sprays in applications ranging from direct injection engines and gas turbines to agriculture, food drying, flame spray synthesis of nanostructured materials [157] and pharmaceutical sprays [182]. In all these reacting and non-reacting applications of sprays, one of the critical outstanding challenges lies in the ability to control the rate of fluid fragmentation and the resulting droplet distribution at the end of the secondary atomization zone. Existing capabilities to model and control sprays in practical devices rely on extensive experience and somewhat empirical correlations of key controlling dimensionless parameters such as the Weber and Ohnesorge numbers [168]. Reliable predictive tools for atomizing sprays will facilitate the optimization of injector designs, enabling a larger degree of control over the atomization process and the resulting droplets. However, achieving such objectives requires extensive development of physical modelling and numerical solution methods for atomization, which depends on extensive validation using reliable data.

1.2 Immiscible flows and atomization phenomenon

The immiscible condition happens when two or more fluids interact with each other but do not get mixed to have a homogeneous mixture. The atomization process is a perfect example of such flows where air, depending upon the flow conditions, helps to disintegrate the liquid jet first into ligaments and then droplets, but the liquid does not evaporate and mix with the air at the molecular level. The atomization phenomenon is a combination of several complex liquid-gas interactions. Near a liquid jet nozzle, the liquid is initially a continuous stream that experiences fundamental instabilities at the interface with the surrounding gas leading to breakages and the formation of discrete ligaments. These ligaments continue to break further, and the drops reduce in size and become increasingly spherical. The shape and size distributions of these drops are heavily related to the initial instabilities that have taken place in the primary atomization region [139, 153, 235, 236].

Several dimensionless parameters are involved in the primary atomization process that plays a key role in controlling the phenomenon [87]. Atomization strongly depends on the injector type and momentum difference between the liquid and air. When the liquid jet is injected into co-flowing air at a high relative velocity, the jet breaks up because of the kinetic energy transfer from the air/gas to the liquid. This type of break-up is known as air-blast or air-assisted atomization [48, 71, 142, 143]. There are several applications that are based on this co-axial atomization process; many of them are combustion devices. For example,liquid-propellant rocket systems [33] are composed of many co-axial atomizers, each of which carries a central jet of liquid oxygen surrounded by high-velocity hydrogen gas. The experimental studies [207, 208, 206, 162, 111, 70] are very helpful to understand the physical aspects behind this type of atomization process. These studies explain that in air-blast atomization, the liquid jet breaks up because of the instabilities occurring at the liquid-gas interface. The physical phenomenon, which is closely related to experimental findings, consists of a two-stage instability mechanism [80, 278]. Once liquid and gas streams leave the jet, the liquid jet undergoes Kelvin-Helmholtz instability. This instability grows and the most unstable wavelength λ_{KH} is determined by the vorticity layer thickness δ_g formed in the incoming gas flow inside the nozzle [206, 266] and density ratio of corresponding liquid and gas streams defined [266] as $\lambda_{KH} \propto \delta_g \sqrt{\frac{\rho_l}{\rho_g}}$. The work of Varga et al. [266] confirms that Kelvin-Helmholtz instability is independent of the liquid jet diameter. These primary waves then interact with a high-velocity gas stream, resulting in secondary interfacial instabilities. This gives rise to Rayleigh-Taylor instability with wavelength λ_{RT} depending on the in-flow conditions [111, 110, 265, 266, 10, 26]. This Rayleigh-Taylor instability undergoes a quick transverse modulation and causes the stripping of ligaments.

Comparatively, less consensus has been developed so far to identify the basic mechanism of primary break-up for a liquid injected into stagnant high-pressure air. The experimental observation of the liquid-gas interface characteristics is very challenging, and the dense spray, which surrounds the liquid jet, prevents detailed optical access [139, 153]. Moreover, length and time scales linked with the primary atomization are very small compared to the integral length and time scales [87]. Many inter-linked physical processes lead to velocity fluctuations of the flow inside the nozzle. These fluctuations lead to a nonlinear instability of the liquid jet exiting the nozzle. Experimental studies confirm that a list of relevant parameters contributes to this type of atomization process. These include the level of turbulence generated within the nozzle [73, 244], nozzle geometry, cavitation [43, 243] and unsteady injection velocity [63].

There are several dimensionless parameters that are very helpful in analyzing the characteristics of primary atomization [87]. In the case of air-blast atomization, these are Weber number ($We = \frac{\rho_g (u_g - u_l)^2 D_l}{\sigma}$); non-dimensional thickness of incoming boundary layer within the nozzle ($\frac{\delta_g}{(D_g - D_l)}$); ratio of Rayleigh-Taylor and Kelvin-Helmholtz unstable wavelengths ($\frac{\lambda_{RT}}{\lambda_{KH}}$); gas to liquid density ratio ($\frac{\rho_g}{\rho_l}$) ; gas to liquid mass ratio ($\frac{\rho_g u_g (D_g^2 - D_l^2)}{\rho_l u_l D_l^2}$); gas to liquid dynamic pressure ratio ($\frac{\rho_g u_g^2}{\rho_l u_l^2}$) and Ohnesorge number ($Oh = \frac{\mu_l}{\sqrt{\rho_l \sigma D_l}}$). Ohnesorge number indicates relative interfacial viscous stress in relation to the surface tension force. The Weber number is a relative measurement of dynamic pressure value with reference to the surface tension force and is the most valuable dimensionless number in characterizing atomization.

For the liquid injection in high-pressure quiescent air, the relevant non-dimensional parameters includes level of turbulence ($l_t/D_l, \sqrt{k_t}/u_l$) and cavitation number ($\frac{\rho_l u_l^2}{2(p_g - p_{vap})}$). Here l_t and k_t represent the turbulent length scale and turbulent kinetic energy respectively, p_g and p_{vap} are pressure values for quiescent air and saturated vapours respectively. Experimentally analyzing the effects of all these parameters in different atomization regimes under realistic operating conditions (like high velocity and pressure, inhomogeneous and dense three dimension liquid gas regions) is very challenging [74]. To overcome these difficulties, numerical solutions may be able to provide a better alternative.

1.3 Turbulence and its role in the atomization processes

In addition to the factors discussed in Section 1.2, the turbulence behaviour of a liquid jet also contributes to the break-up processes. The break-up length of the liquid jet can be significantly shortened [45, 190, 166] by changing the flow environment from laminar to turbulent. The turbulence level developed at the jet exit, initially started inside the nozzle, more dominantly controls the liquid jet atomization phenomenon and regimes, velocity fluctuations, droplet sizes and their distribution [274, 13, 220, 221]. Turbulent behaviour is considered the main driving force for the liquid stripping near the nozzle exit. Experimental findings helped develop the general correlation between the level of turbulence, jet break-up length and drop sizes. As experimental findings become more and more helpful in getting the desired details, numerical simulations are also considered a valuable investigation tool for studying the complexities involved in the atomization process.

Bianchi et al. [24, 23] performed the numerical simulations for the atomization of diesel jet. They found that the turbulence level generated within the injector strongly impacts jet penetration and break-up behaviour but weakly affects the drop sizes and their distribution. However, they did not report the grid independence of their solution, which questions the applicability and reliability of their approach.

Numerical solutions [24, 23, 134, 147] in combination with experimental findings are very helpful to analyse the turbulence effects on atomization behaviour. Various mechanisms involved in the disintegration of turbulent jets have been discussed in detail by Lefebvre and McDonell [147]. However, the physics involved in the break-up processes is still not very well understood. For example, it is still unclear whether atomization is primarily driven by aerodynamic interaction between the liquid and the gas or the break-up processes within the injector nozzle. However, experiments confirm that it is strongly affected by turbulence intensity at the jet exit. Inflow boundary conditions and level of turbulence generated inside the nozzle are strongly linked [245, 132, 133] to the primary break-up behaviour in the atomization process, whose complete understanding is still a challenge for researchers. Generating realistic boundary conditions similar to those of practical injectors is necessary for a more physical understanding of the atomization processes.

Over time many numerical modelling efforts [145, 154, 65, 131] have been made for the generation of inlet boundary data. The simplest way is to take a mean velocity profile with superimposed random fluctuations, and the resulting data is equally distributed over the whole wave-number range. This approach leads to excessive energy in the high wave-number zone resulting in the immediately damping of small-scale turbulence. Lee et al. [145] suggested an improvement by following an inverse Fourier Transform in the wave-number space. The programming required for implementing this method is rather complex, and using the Fourier

Transform needs specific grid requirements [134] that limit its applications. Lund et al. [154] approach is based on the cross-correlations of velocity components. The critical correlation factor is extracted from the experimental data.

The work of Klein et al.[134], usually termed Klein's digital filter, is based on digital filtering of random data and can reproduce the desired statistics with second-order accuracy along with auto-correlation functions. Its implementation is very convenient and can be easily linked with experimental data. It also helps to overcome the limitations of the classical approach using the inverse Fourier Transform concept. The length scale can be defined locally for each coordinate direction, and the output signal can be either periodic or non-periodic without any restrictions. Using the in-flow generating procedure helps achieve a better agreement with relevant experimental data. This approach is capable of producing consistent results [134] for various flow conditions, such as round jets and liquid sheets.

1.4 Overview of recent developments in numerical solutions

Massive improvements in high-performance computing are helping to advance the ability to resolve liquid-gas interfaces near the exit plane of injectors. Several approaches exist to simulate interfaces, including volume of fluid (VoF) [107], level set (LS) [251] and diffuse-interface (DI) [11] methods. The VoF approach conserves mass and can be applied with or without interface capturing or reconstructions methods [170, 272, 202, 109, 151] but remains sensitive to mesh resolution. LS and DI methods require additional corrections to satisfy mass conservation [60, 282, 171]. VoF based methods are the focus here. A continuity equation is solved for the liquid volume fraction, α, which has values of unity in the pure liquid stream and zero in the pure gas stream. Interface sharpening, e.g., by artificial compression [272], is commonly used in an attempt to reduce the inherent numerical diffusion, which is a dominant term in the absence of volume fraction molecular diffusion. Note that in standard VoF computational models, α values other than zero or one are only produced due to numerical diffusion and represent a kind of grid average. A beneficial consequence is that the computational volume fraction is a continuous field; however, unlike actual flows, the interface is not perfectly sharp. Highly resolved grids are generally required to minimize numerical diffusion and to resolve the vital topological features of the interface which determine the atomization modes.

Direct numerical simulation (DNS) with VoF is useful for fundamental studies [59, 102, 57], but application to practical flows is generally not possible due to the very large computational expense. Only two dimensional DNS under conditions similar to those of practical injectors was reported in [26, 81], while three dimensional DNS studies remain limited in scope [60, 144, 101, 21]. Large-eddy simulations (LES) have the potential to fill this gap with much lower resolution requirements while resolving many of the large scale physical phenomena that affect primary atomization. The key challenge with LES is to accurately model the liquid-gas interface, which has a characteristic scale far smaller than the filter width or grid size. Most of the existing LES for turbulent interfacial flows have simply applied a conventional turbulence filter to the VoF transport equations, and the sub-grid near-interface processes have been modelled using the well-known sub-grid models that were developed for the turbulent characteristics prevalent in single-phase flows [34, 54, 47, 184, 130]. Some significant physics is neglected with this conventional turbulence filtering approach because: (i) inertial range turbulent eddies and the energy cascade are not statistically universal across an interface with a large density ratio; (ii) the one-fluid assumption, which is the basis of VoF methods, is compromised when the cell or filter size is large; and (iii) for turbulent but low Reynolds number interfacial flows the sub-grid turbulent diffusivity is too small and takes no account of the significant inhomogeneities induced by the dynamics of the interface [275]. Additionally, numerical diffusion is significant, and grid sensitivity has rarely been tested. Hecht [98] and Anez et al. [12] proposed adding an artificial compression term to minimize numerical diffusion in flow regions adjacent to a continuous interface. In contrast, in regions of the flow with discontinuous interfaces, turbulent diffusion is used to model the dispersion of unresolved ligaments and droplets at the sub-grid scale. A criterion based on the grid resolved curvature is generally used to identify where the interface is continuous, but this itself can be grid sensitive.

Recently Wang et al. [270] developed a new VoF based approach called explicit volume diffusion (EVD), which is applicable to laminar and turbulent flows and compatible with LES. The EVD governing equations are formulated by averaging the VoF transport equations over an explicitly defined physical volume. Values of α between zero and one in this model have physical meaning and are not just numerical artefacts. Upon volume averaging, new sub-volume flux and sub-volume stress terms appear in the transport equations due to the inhomogeneity of the volume fraction and velocity fields at the sub-volume scales. These terms are closed by introducing sub-volume diffusive and viscous models, which were shown to be reasonably general over a wide range of laminar and turbulent Reynolds numbers and liquid/gas density ratios. A closure for the volume averaged surface tension force is also provided, which includes the effect of the sub-volume interface dynamics. The physical volume averaged equations are discretized on the LES grid. By refining the LES grid while keeping the volume scale constant, the explicit volume diffusion overwhelms the numerical diffusion, and thus, numerical convergence can be achieved.

1.5 Research aims and outline of the thesis

The purpose of this study is to investigate the existing numerical solutions used for the interfacial flows and to have a solution that is more reliable and can lead to better predictions. This study also focuses on the detailed analysis of sub-grid surface tension effects and how they control the atomization processes and subsequent liquid jet decay rate. In this Chapter, a brief description of immiscible flows is presented. The requirement for a better understanding of the atomization phenomenon is also discussed. The effects of turbulence and relevant non-dimensional parameters on the atomization behaviour are explained in detail. Chapter 2 includes a brief description of interface-capturing methods for interfacial flows with different numerical approaches developed over time. Key features and the relevant limitations are explained systematically, leading to the issues addressed in this study. The necessity of having a reliable, effective and economical under resolved solution to the problem is discussed comprehensively. Stochastic formulation of the Eulerian-Lagrangian spray atomization (ELSA) model for the combined VoF and surface density is described in the first half of Chapter 3. However, the second half mainly includes the behaviour of numerical convergence, jet penetration and jet decay rate to the number of stochastic fields for three different mesh sizes. Moreover, an analysis of probability density function (PDF) distribution for both liquid volume fraction and surface density is also conducted in the later part of Chapter 3. It is revealed that numerical convergence in the stochastic fields approach is illusive and that motivates a systematic study of other LES-based approaches in Chapter 4. The detailed mathematical formulation of models TFVoF, TF-AC and EVD is explained in Chapter 4 in the context of LES methodology. A comparison of two already existing models, the turbulent filtered volume of fluid (TFVoF) and hybrid turbulence filtering with artificial compression (TF-AC), with the newly developed solution termed as explicit volume diffusion (EVD), is discussed thoroughly. Special care is taken for the sub-grid fluctuations of surface tension force, and an improved sub-model is suggested based on the physical volume length scale. Additionally, a sub-grid surface tension model based on the pressure jump across the interface is also presented, which then is incorporated with all three TFVoF, TF-AC and EVD formulations in order to study the sub-grid surface tension force behaviour. Detailed numerical analysis of the three different turbulent modelling approaches, TFVoF, TF-AC and EVD, is presented in Chapter 5. Firstly, grid convergence behaviour and the effect of grid size on the jet penetration and decay rate are examined for each formulation using three different grid resolutions. Their numerical performance is evaluated following the Zalasek disk test case and the Richardson Extrapolation calculations. Secondly, the applicability of the EVD approach is evaluated against different physical length scales, and sub-grid surface tension effects are analyzed using the physical volume length scale concept. Lastly, the effects of pressure jump based solution for sub-grid surface tension are studied for all TFVoF, TF-AC and EVD turbulent solutions. A complete summary of current numerical findings, existing limitations and future possibilities are discussed at the end of this report in Chapter 6.

Chapter 2

Theoretical Background

Over time, many approaches developed for the numerical studies of immiscible flows and the desired solution is obtained by following either tracking or capturing of the interface. The interface-tracking method's drawback is not providing an exact solution for topological changes. Alternatively, detailed numerical solutions based on the interface-capturing technique got significant attention as it avoids the complexities [223] involved in interface-tracking solutions. Interface-capturing methods have been widely used and investigated for interfacial flows. With time, continuous improvements have been made to overcome the limitations [87] associated with them, but inherent shortcomings remain, especially concerning their strong grid dependence. Experimental findings and their limitations are briefly reviewed first, and then an overview of different numerical treatments for interfacial flows is presented in detail. The second half of this chapter presents a complete description of VoF and LS based interface-capturing approaches and their developments over time.

2.1 Experimental findings and limitations

Developments in diagnostics methods are helpful for the spray measurements to have detailed spray characterization, which is very useful in various applications. For better understanding, these measurements [17] can be categorized into three key sub-divisions: research, development/testing, and quality assurance. For research purposes, there is a need for much detailed information regarding the flow behaviour within the injector, initial instabilities taking place in the near field region leading to the jet break-up, breaking of the jet into ligaments, and finally, the drop sizes and their distribution.

For industrial purposes, the development and testing of atomizers are generally based on a comparatively simple approach where the effect of a change in design is analyzed based on the final spray measurements without getting insight into physical processes occurring in the near-field region of the atomization process. In the area of quality assurance, the consistency of processes involved in atomizer manufacturing needs to be measured and monitored. Most of the measurement needs for the last two applications are satisfactorily met with the currently available diagnostic resources. Lorenz-Mie light scattering and fluorescence are capable of having a rapid analysis of spray quality and pattern. Available shadowgraph imaging techniques are capable of providing critical information like spray cone angle, break-up length, and qualitative behaviour of spray [238]. Quantitative information on spray vapour can be gathered by laser-induced exciplex fluorescence imaging [169, 108].

However, the current availability of diagnostics is still incapable of a complete analysis of spray processes required to get the critical information needed to evolve vital physical concepts, strengthen the theoretical background, and numerical developments. For a thorough understanding of the physics involved in an atomization process, much more detailed information is necessary, which should be collected for the same injector under similar environments and conditions. This information loses authenticity, especially for theoretical and numerical needs, when some measurements are made with one injector and rest with another injector under different conditions. More details of internal flow fields within the atomizers would be beneficial in understanding the spray formation processes and providing accurate vital data to modellers. Electronic sensor-based techniques are helpful in measuring the internal flow details. For example, high-frequency pressure fluctuations can be measured with the help of miniature pressure transducers either within the injector or near the jet exit zone. Microsensors manufactured using MEMS technology [283, 187] can be made small enough to measure the mean and turbulent velocity fluctuations inside the atomizer. However, the key challenges are i) development cost is still very high that makes them out of reach for most of the research applications ii) occurrence of cavitation phenomenon makes the measurements unreliable.

Liquid velocity data can be successfully obtained using laser Doppler velocimetry (LDV) [159]. Double-pulsed holographic imaging and gaseous image velocimetry (GIV) are also helpful in studying the liquid sheets from the velocity data of ligaments and the corresponding flow field. Useful information like jet instabilities, waves spatial and temporal frequency, and liquid flow velocity can be obtained with imaging approaches such as high-speed shadow imaging [140] and ballistic imaging [68] when coupled with multiple exposures [38]. Jet break-up length [150] can be measured with the help of pulsed-laser imaging and tomographic analysis [92, 146]. Further downstream, accurate drop size measurement, their velocity and number density, and volume flux become important [18]. Local drop velocity for all size classes and gas phase can be measured in a polydisperse two-phase flow using planar laser-induced fluorescence and phase Doppler techniques [76]. The local slip velocity is approximated from the values of drop and gas velocities [142] but cannot be measured at a point simultaneously with the currently available resources. Change in diameter due to evaporation can be measured for a single stream of droplets following Smith et al. [239] but still not possible in the case of polydisperse evaporating spray field. Significant effort is required to improve these diagnostics to have a reliable data set, especially for turbulent two-phase flows with polydisperse drop size distribution.

Two air-blast acetone spray cases (designated N-AS2 and N-AS8) from the Sydney needle spray burner measurements [153] have been used to validate numerical solutions. The two-angle backlit imaging method [236] helps to have the mean volume fraction measurements along the flow axis. The improved postprocessing approach for analyzing the simultaneous images taken by two cameras at the same axial location helps have volume fraction measurements. Though there are still challenges having the experimental measurements in the radial direction of jet and limitation of the optical access in the dense region, numerical findings are helpful in analyzing the atomization phenomenon in more detail, such as volume fraction measurements in the radial direction, better representation of interfacial instabilities at the liquid gas interface especially in the near-field region, jet penetration and decay rate. Furthermore, experimentally validated numerical solutions have the potential to have solutions for those interfacial flows whose experimental measurements are more challenging or not possible with the available resources.

2.2 Numerical treatments for interfacial flows

Extensive literature is available to understand and investigate the numerical methods for interfacial flows. To achieve the comprehensive understanding of these approaches, the reader can benefit from the work of McHyman [114], Anderson et al. [11], Scardovelli and Zaleski [223], Floryan and Rasmussen [77], Shyy et al. [234], Sethian [227], Unverdi and Tryggvason [261], Sethian and Smereka [229], Smolianski [240] and Sussman et al. [249]. For a systematic understanding of all these available methods, computational modelling is usually categorized into five main sub-parts

i) treatment of flow fluid
ii) interface modelling
iii) interface and fluid flow coupling
iv) discretization schemes
v) flow equations solution

Fluid motion treatment can be further distinguished [240, 158] based on the numerical algorithm used in the specific two-phase problem. This can be either Eulerian [41, 240, 158] or Lagrangian [269]. In some cases, a combination of both Eulerian and Lagrangian [40, 69, 106] is also used. We have a stationary frame of reference in Eulerian methods, and in numerical solutions, the fluid moves from one computational cell to the next. However, in Lagrangian methods, the frame of reference moves with the fluid and the numerical methods involve tracking specific fluid elements along their pathlines. Motion of free surface between two fluids can be captured by either interface-tracking [167, 258] or interface-capturing [172]. Coupling of fluid flow and interface can be made by either solving the flow fields and interface simultaneously [50, 215, 218] or only the flow fields are solved while considering the interface as fixed [204, 253, 254, 277]. Numerical solutions are very sensitive to discretization schemes, and most commonly used for two-phase flows are finite difference [127], finite element [97, 186, 233] and finite volume [105, 107] methods. Solution of flow field variables can be obtained either following integrated [233] or segregated [105] approach.

2.2.1 Eulerian methods

In a fully Eulerian treatment of the two-phase problem, fluid flow calculations are performed with reference to a fixed coordinate system. Solution for the interface can be obtained by either capturing or tracking methodology.

Inetrface-tracking

The pioneering work of Harlow and Welch [93] explaining the marker and cell (MAC) method is considered as a benchmark for having the free surface flows solution. Marker particles were used to identify the spatial boundary of the fluid and adjacent free surface. The specific cell contains liquid if there are one or more marker particles; otherwise, the cell only has gas if it has no marker particles. The interface is obtained from cells with marker particles but adjacent to the empty cells. This approach was a major breakthrough in dealing with multi-fluid flows, especially for those having interfaces with large distortions. But there were some challenges, like, not having proper interface orientation, high computational cost, and difficulty in applying proper boundary conditions at the interface. These limitations became the motivation for later researchers [104, 185, 86, 167, 185, 205, 261], whose contribution helped to improve and extend this approach. The main contributors are: Hirt and Cook [104] who proposed an algorithm for the correct pressure predictions; Noh and Woodward [185] who helped in improving the interface reconstruction; Ramshaw and Trapp [205] who improved the algorithm for fluid convection; Glowinski et al. [86] who used the segregated fractional-step approach to solve the flow field and finite element method for the spatial discretization. The coupling of flow fields and the interface is made in a segregated way when interface-tracking solutions are followed.

Inetrface-capturing

In all interface-capturing methods, the interface modelling solution is based on some specific fluid properties; for example, the liquid volume fraction is used in the volume of fluid (VoF) methods, and a specific value of an implicit function is used in level set (LS) methods. Transport of that function or field variable is treated similarly to other flow field parameters. Interface, either based on discontinuous field variable or continuous implicit function, is advected with the fluid movement. Interface calculation is coupled to the momentum equation linked with local density, viscosity and surface tension forces. In sharp-interface mechanism [252, 84, 155], density and viscosity values have followed a big difference across the interface, while in diffuse-interface methods [61], these field variables are linearly linked to indicator function, which is liquid volume fraction in most of the cases. However, opposite to the interface-tracking approach, where interface calculation depends on the Lagrangian motion of particles, the interface-capturing approach is based on the Eulerian advection of the interface.

VoF method was first developed by Hirt and Nichols [107] and is based on the liquid volume fraction concept in a multi-fluid environment. Usually, the liquid phase is assigned the value of 1, and for the gas phase, its value is 0. The interface is present in those regions where this value is neither 1 nor 0. This type of interface representation behaves in a discontinuous manner which needs reconstruction at each time step. Initially, these reconstruction methods were first-order accurate,i.e., simple line interface calculation (SLIC) [185]; then improved with time to have higher-order solution accuracy and interface representation,i.e., piecewise linear interface construction approach [14, 201, 214, 193, 152].VoF behaves well in keeping the mass conserved and can be easily extended to three-dimensional problems but has an issue with interface diffusion. Different level of numerical diffusion associated with various grid sizes leads to grid sensitivity issue. Numerical treatment is required to have a sharper interface and to overcome grid sensitivity problems. Most of the VoF methods usually follow simultaneous solutions of flow fields and interface with finite volume or finite difference schemes for spatial discretization.

In LS methods, the interface is represented by a specific value of an implicit variable (the level set function) that is treated as a continuous function. Major advantages of this approach are a better representation of the free surface, interface normal and interface curvature. However, lack of mass conservation and difficulty in having accurate interface location are the main challenges associated with its implementation. The work of Sussman et al. [251] and Sethian [227] for the development of this approach applicable to incompressible flows is considered a major contribution to these methods. A detailed explanation of these methods and their applications to physical systems can be found in the book of Sethian [228]. Other useful contributions in the further development of these methods are by Sussman and Smereka [250], Sussman et al. [249], Sethian and Smereka cite [229],Sussman et al. [252] and Herrmann [102]. The implementation of this approach is similar to VoF methods like simultaneous calculations for flow field and interface, finite difference or finite volume based spatial discretization algorithms, but mass conservation is worse than VoF solutions.

2.2.2 Lagrangian methods

These methods are used in combination with interface-tracking algorithms, and the computational grid moves with the fluid flow. The flow field and interface solutions are computed separately. These methods are capable of precisely tracking the material interfaces and allow the application of interfacial boundary conditions in a more realistic way. Accurate Lagrangian description of the flow field and the interface can be found in the work of Okamoto and Kawahara [186] and Hayashi et al. [97]. Very few approaches are based on the Lagrangian tracking of fluid flow elements. To overcome the mesh distortion problems linked with these Lagrangian methods, a meshless approach based on the smoothed particle hydrodynamics (SPH) was a significant success. This approach was initially developed to deal with astro-dynamical issues [176] and later on successfully applied to fluid flow problems [173–175, 52, 51]. Though this approach has a remarkable capability to deal with complex flow fields, SPH based solutions are computationally more expensive than Eulerian approaches. Moreover, SPH methods do not represent the interface accurately because of insufficient resolution linked with improper clustering of particles.

2.2.3 Combined Eulerian-Lagrangian methods

Most of these methods solve the flow field with Eulerian grids, and the free surface solution is based on Lagrangian treatment. The arbitrary Lagrangian-Eulerian (ALE) method developed by Hirt et al. [106] is considered a pioneer work within the Eulerian-Lagrangian framework. Firstly, the solution is obtained with respect to an initial fluid domain which is then recalculated at each time step on the deformed grid following the fluid motion [64, 164, 75]. Significant challenges associated with this approach are the need to recalculate an elementary matrix for spatial derivative computations, and time derivative solutions are computationally more demanding. However, their flexibility to deal with the motion of mesh vertices makes them suitable for free surface flow calculations [20, 64, 164, 277, 204]. All these solutions employed finite element discretization with the segregated treatment of interface coupling. The Eulerian-Lagrangian approach has been used successfully for many fluid-structure interaction problems [89]in which fluid flow is treated as Eulerian and the structures as Lagrangian with consideration of moving fluid domain. Either finite element or finite difference approach is followed for discretization solutions with the modified meshes at each time step, and special treatment is needed to solve the equations on moving grids.

Another category of these Eulerian-Lagrangian methods deals with the integrated coupling of the flow equations and interface solution for both steady [215, 219] and unsteady [50, 218, 19] free surface flows. The solution is advected as a combined discretization of flow fields and interface solution. Either Newton or quasi-Newton iteration process is followed for the solution of resulting nonlinear algebraic equations. Compared to a segregated solution, this approach is capable of a fastly converged steady-state solution.

Eulerian-Lagrangian spray atomization (ELSA) model, initially developed by Vallet et al. [263] and Lebas et al. [144] in Reynolds-averaged Navier-Stokes (RANS) formulation, is widely used and investigated for spray atomization problems [46, 47, 69, 170, 184, 12]. ELSA solution is based on following an Eulerian description in the dense part of the spray, and a standard Lagrangian approach is followed in dispersed/dilute regions of spray. This approach utilizes the concept of interfacial surface density area calculated in each cell without indicating the shape of the corresponding fluid structures [47]. Chesnel et al. [46, 47] followed the ELSA approach to have a large-eddy simulation (LES) solution of liquid sprays with useful statistical findings in the context of two-phase flows. DNS studies of Duret et al. [69] based on ELSA formulation is very helpful for a better understanding of the atomization process. Most recently, Anez et al. [12] used this ELSA approach in combination with the interface-capturing mechanism (ICM) to have a more physical distinction between dense and dilute regions. ICM is only effective in dense regions to have a realistic interface representation of the corresponding two-phase problem.

2.3 Progress in interface-capturing approaches

Following the interface-capturing methodology explained in Section 2.2, the solution of the phase interface is obtained from the calculation of an additional scalar. Two main methods have been widely used in this category: volume of fluid (VoF) [107, 223] and level set (LS) [226, 251, 227]. For incompressible flows, continuity and momentum equations for the multi-phase environment in terms of single density component are written as

$$\frac{\partial \rho}{\partial t} + \frac{\partial \rho u_i}{\partial x_i} = 0, \tag{2.1}$$

$$\frac{\partial \rho u_i}{\partial t} + \frac{\partial \rho u_i u_j}{\partial x_i} = -\frac{\partial p}{\partial x_i} + \frac{\partial \tau_{ij}}{\partial x_i} + F_{s,i} + \rho g_i. \tag{2.2}$$

The solution of these equations can be based on either VoF or LS. In some cases, both VoF and LS are used in combination. Here ρ is the density of the mixture computed based on corresponding liquid and gas phases densities, g is gravitational acceleration to account for body force, $F_{s,i}$ accounts for surface tension force, u denotes velocity, p is pressure, t is time and x_i represents the spatial coordinate in the ith direction. For Newtonian fluids, the viscous stress is given by

$$\tau_{ij} = \mu \left[2S_{ij} - \frac{2}{3} \frac{\partial u_k}{\partial x_k} \delta_{ij} \right], \tag{2.3}$$

where

$$S_{ij} = \frac{1}{2} \left(\frac{\partial u_i}{\partial x_j} + \frac{\partial u_j}{\partial x_i} \right) \tag{2.4}$$

is the strain-rate tensor and δ_{ij} is a Dirac delta function. For immiscible fluids, the real interface is sharp, and a continuum surface tension model can be used [30] to capture the realistic surface tension effects, written as

$$F_{s,i} = \sigma \kappa n_i \delta_s, \tag{2.5}$$

where σ is the surface tension coefficient, $\kappa = -\nabla \cdot n$ is the interface curvature found through the unit normal vector n, and δ_s is an interface detecting function. The values of n and δ_s are calculated based on characteristic scalar function, which is liquid volume fraction when following VoF method and level set function value when following LS method.

2.3.1 Level set (LS)

In level set method [251, 227, 229] level set function φ is used to represent the liquid-gas interface. Generally, the interface is represented by the zero contours of a signed distance function. This distance is positive in one fluid region $(= +d)$ and negative in the other fluid region $(= -d)$ where d is the shortest distance of point (r, z) to the free surface. The movement of the interface is controlled by the advection of the differential equation for the level set function. Normally, positive value of level set function ($\varphi > 0$) represents the liquid region and a negative value ($\varphi < 0$) represents the gas region. The free surface is represented by having a level set function value equal to zero ($\varphi = 0$). The main advantage of the level set (LS) method is its simplicity, especially in calculating the solutions for interface normals and curvature. The unit normal vector n and curvature K are computed as follows

$$n = \frac{\nabla \varphi}{|\nabla \varphi|}, \tag{2.6}$$

$$K = \nabla . \frac{\nabla \varphi}{|\nabla \varphi|}. \tag{2.7}$$

The level set advection equation is written as

$$\frac{\partial \varphi}{\partial t} + u_i \frac{\partial \varphi}{\partial x_i} = 0. \tag{2.8}$$

Level set scalar value remains constant along a particular path. If the free surface is initially characterized by the zero value of the level set function, then this zero value will always represent the free surface throughout the advection solution. Density and viscosity for the flow fields are calculated from the level set function via the Heaviside function, written as

$$\rho(\varphi) = \rho_g(1 - H(\varphi)) + \rho_l H(\varphi), \tag{2.9}$$

$$\mu(\varphi) = \mu_g(1 - H(\varphi)) + \mu_l H(\varphi), \tag{2.10}$$

where H is a Heaviside function that behaves as a step function, and its value is

$$H(\varphi) = \begin{cases} 1 & \text{if } \varphi > 0 \\ 0 & \text{if } \varphi \leq 0 \end{cases}. \tag{2.11}$$

High-velocity gradients lead to the wide stretching of the interface, and the level set will no longer be a distance function [170]. To keep the level set function a signed distance function from the interface, level set methods also require re-initialization of the level set function φ, and the conventional approaches used for this purpose are computationally very challenging [172]. One major limitation of level set methods is that they are not mass conservative. For incompressible two-phase flows, loss or gain of mass makes them physically incorrect [188]. This loss or gain of mass is because of the numerical diffusion that occurs during the level set calculations, which is from the generation of artificial viscosity [255] during the stabilization of the re-initialization process. This artificial diffusion behaves inversely with the grid sizes. Sussman et al. [251, 248]) proposed a partial differential equation (PDE) based re-initialization solution that can be solved either following fast marching method (FMM) [49] or fast sweeping method (FSM) [284]. These methods help reduce the computational load for re-initialization purposes. However, there is an inherent difficulty in parallel implementation because of load balancing issues. It is found that this PDE based re-initialization method [251, 248] changes the interface position significantly [172], leading to a mass conservation problem. Russo and Smereka [216] used a sub-cell approach to have desired interface location and computed the fluxes with second-order accuracy for cells containing the interface. Chéné et al. [66] extended this method to have fourth-order accurate solution. The hybrid particle level set method (HPLC) [72] has proven very effective in reducing the mass loss during the advection process. However, the mass loss quantity reduces with mesh refinement [100, 85], which makes their solution grid-dependent.

Conservative level set

Initially, Olsson and Kreiss [188] developed this approach for multi-phase application, which holds the simplicity of the basic level set (LS) method and helps to reduce the mass loss within the acceptable limit. Later this method was used by Desjardins et al. [60, 59] for primary atomization studies. Their findings were promising in terms of interface curvature capturing and mass conservation. Still, they did not present the grid independence behaviour and drop size distribution for the liquid jet atomization. Olsson and Kreiss [188] used the hyperbolic tangent function approach, which is defined as

$$\psi = \frac{1}{2}(\tanh(\frac{\varphi}{2\varepsilon}) + 1), \tag{2.12}$$

where ε controls the interface's thickness, its value is usually considered as half of the mesh size [188]. Instead of representing the interface location by the iso-surface $\varphi = 0$, it is described by $\psi = 0.5$ iso-surface . The value of ψ is less than 0.5 for $\varphi < 0$ and greater than 0.5 for $\varphi > 0$.

$$\frac{\partial \psi}{\partial t} + u_i \frac{\partial \psi}{\partial x_i} = 0. \tag{2.13}$$

This method is successfully tested against a range of cases [60] and confirms its improved behaviour. The work of Desjardins et al. [60, 59] shows that the conservative level set approach helps to reduce the mass loss problem associated with conventional level set methods. Their accurate version of the conservative level set method [60] is capable of providing realistic interface transport alongside good mass conservation behaviour.

Refined level set grid

Another effort to overcome the limitation of the level set method in preserving the volume of each fluid in a multi-fluid problem is presented here. The mass conservation is directly linked with grid spacing and can be reduced by refining the grid resolution. Locally adaptive mesh refinement methods (AMR) [246, 241] could be an option. However, they introduce additional complexities in cases where a fine grid resolution is required over the entire interfacial region of a complex atomization problem.

Herrmann [99, 100] developed this approach and study the grid independence for primary atomization of fuels [101, 102, 181]. In an attempt to simulate the primary atomization of fuel, Herrmann was the first to do the grid independence check by using the fine grid resolution. He used the course grid for Navier-Strokes two-phase equations and a separated fine cartesian grid scheme called G-grid for the transport of all level set equations. As both flow solver grid and G-grid are treated separately, G-grid can be independently refined. This ensures the representation of a grid converged interface. The use of this equidistant G-grid mesh also allows the direct application of higher-order schemes such as the 5th-order WENO while maintaining their accuracy. The major limitation to this approach is the high computation requirement, as it requires the solution of both grids in parallel. Particularly the G-grid refinement makes it computationally challenging both in time and memory.

The refined level set grid method (RLSG) has been applied to a range of test cases [99]. Numerical findings confirm that RLSG is capable of providing better mass conservation solutions even for coarser resolutions. Furthermore, the use of this method has successfully extended [100–102, 181] to study the primary atomization of liquid jets in co-axial and cross-flow conditions. Gorokhovski and Herrmann [88] have presented an LES model for capturing the sub-grid phase interface dynamics of interfacial flows following the standard RLSG methodology.

Robust conservative level set

This approach [199] originally based on the work of Olsson et al. [188] and Desjardins et al. [60] is specifically tailored for industrial applications by using the three-dimensional unstructured meshes that make calculations possible for complex geometries. Pringuey and Cant [199] employed the OpenFOAM platform (an open-source CFD tool kit) and termed it as RCLSFoam. Special care needs to be taken in getting a reasonable compromise between accuracy of results, computational cost and robustness of the method.

Even the use of high order numerical schemes such as WENO [197, 198] will also diffuse the interface, and there is the requirement of re-initialization of the level set function to keep the thickness of the interface constant. This is achieved by applying a compressive flux in the normal direction to the interface in the interfacial regions. The compressive flux causes the reduction of interface thickness and makes it less robust. To avoid this, a diffusion term is added to the governing equation. Considering the interface normal "n" and artificial time "t" the original conservative level set equation Eq. (2.13) will take the form of

$$\frac{\partial \psi}{\partial t} + \frac{\partial}{\partial x_i}(\psi(1-\psi)n) = \frac{\partial}{\partial x_i}(\varepsilon(\frac{\partial \psi}{\partial x_i}.n)n), \tag{2.14}$$

where the second term on the left hand side ensures the sharpness of the interface. The term on the right hand side is responsible for the phase indicator's diffusion and ensures the desired characteristic thickness ε to be resolved on the given mesh. The above equation can be re-written as

$$\frac{\partial \psi}{\partial t} + \frac{\partial}{\partial x_i}((\psi(1-\psi)n - \varepsilon(\frac{\partial}{\partial x_i}\psi n))n) = 0. \tag{2.15}$$

The performance of the robust conservative level set (RCLS) method is tested against the VoF method of OpenFOAM termed as interFoam and the accurate conservative level set (ACLS) method of Desjardins et al.[60]. Canonical test cases have been used for this comparative analysis. Numerical findings confirm the better performance of the RCLS transport algorithm against the interFoam and ACLS calculations. Furthermore, RCLS also performs better on unstructured grids when compared with interFoam, and results are more stable and accurate [199].

One-layer particle level set

Most recently, a one-layer particle level set (OPLS) [285] method has been developed in which Lagrangian particles are employed to correct both advection and re-initialization. OPLS behaves better in terms of interface capturing and mass conservation. Compared with the particle level set (PLS) method [72], the number of particles is reduced comprehensively in the OPLS as the Lagrangian particles describe an accurate interface through only one layer of particles that helps to reduce the computational cost. In OPLS, particles are initially scattered on both sides of the interface and then attracted to the interface. Particle speed is interpolated linearly from the surrounding velocity field of the grid nodes. The third-order TVD-Runge-Kutta scheme [128] is used to evolve the particle positions forward in time as follows,

$$\varphi^{(1)} = \varphi^{(0)} + \Delta t L(\varphi^{(0)}), \tag{2.16}$$

where L stands for the differential operator, t for time and φ represents the level set function. Particles are used to modify the interface, and at each time step, both advection and re-initialization are modified as

$$\varphi^{(2)} = \frac{3}{4}\varphi^{(0)} + \frac{3}{4}(\varphi^{(1)} + \Delta t L(\varphi^{(1)})), \tag{2.17}$$

$$\varphi^{(3)} = \frac{1}{3}\varphi^{(0)} + \frac{2}{3}(\varphi^{(2)} + \Delta t L(\varphi^{(2)})). \tag{2.18}$$

This approach can handle complex topological changes more accurately, even during the interface merging or stretching. The OPLS method is tested against several benchmark cases, and the results show better mass conservation behaviour when compared with the standard LS method. Furthermore, OPLS has an accurate and sharp interface representation when tested against Zalesak's slotted disc problem.

Upon testing against different grid resolutions, the OPLS approach can produce acceptable solutions, even when the grid resolution is coarse. The performance of OPLS is also very satisfactory when tested against the merging and break-up of surfaces. During the canonical test of vortex in a box, the use of particles for interface calculations shows considerable improvement in curvature estimation compared to standard LS methods. Though OPLS can successfully capture the bubbles or droplets with better mass conservation and less shape distortion, its performance against the practical multi-phase problem still needs to be tested.

2.3.2 Volume of fluid (VoF)

The basic idea for the VoF method can be described by considering two fluids, say liquid and gas, in a given three-dimensional domain, and we want to capture the interface between those fluids. Suppose α represents the volume fraction of liquid in a given cell. Its value will be in the range of

$$0 \leq \alpha \leq 1. \tag{2.19}$$

The value of α is 0 in regions of pure gas and 1 in the pure liquid zone. In the absence of phase change, the volume fraction α is passively advected and satisfies the following advection equation.

$$\frac{\partial \rho \alpha}{\partial t} + \frac{\partial \rho u_i \alpha}{\partial x_i} = 0. \tag{2.20}$$

Equation (2.20) has no molecular diffusion term but numerical diffusion produces locations where $0 < \alpha < 1$ such that the interface is artificially smeared.

The VoF approach [107, 249] is based on volume fraction α of one fluid in multi-phase domain. The value of α represents the amount of the specific fluid present in the considered cell. Its value ranges from 0 to 1. If its value is 0 or 1 in a particular cell, then there is no interface present in that cell. Phase interface presents only in those cells where its value is between 0 and 1.

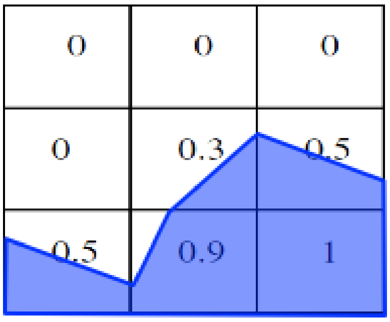

Fig. 2.1 Interface representation based on VoF approach

In VoF methods, two immiscible fluids can be modelled as a single fluid having singular values of density and dynamic viscosity at each point in space and time that are linear functions of the liquid volume fraction, α, written as

$$\rho = \rho_g(1-\alpha) + \rho_l \alpha, \tag{2.21}$$

$$\mu = \mu_g(1-\alpha) + \mu_l\alpha, \tag{2.22}$$

where μ_g and μ_l are the viscosities for gas and liquid phases, respectively.

Unlike LS based approaches, VoF methods do not require re-initialization solutions to keep the interface at the exact position that makes them able to have improved mass conservation solutions. Better representation of mass conservation is a major advantage of the VoF methods, making them a popular choice in interface-capturing methods. However, the interface represents a discontinuity with a change in density occurring over molecular scales that requires special geometric algorithms to avoid the unacceptable diffusion of α [210, 90]. Another critical issue with the VoF method is the discretization of advection term in Eq. 2.20. Lower-order schemes result in smearing of the interface due to numerical diffusion. However, higher-order schemes are computationally expensive and mostly unstable leading to numerical oscillations. Therefore, it is mandatory to have the advection solutions for the interfacial flows, which are reliable and can deal with sharp topological changes. Numerical limitations related to the interface calculation for the VoF approach are discussed in detail by Tryggvason et al. [259]. The position of the interface is highly affected by the numerical diffusion, which is directly dependent on mesh size [260]. Over time, several volume advection techniques have been proposed by many researchers. Some of these are, simple line interface calculation (SLIC) by [185], flux-corrected transport by [28], Lagrangian-PLIC by van Wachem and Schouten [264], CICSAM by Ubbink [260] and inter-gamma compressive scheme by Jasak and Weller [120].

Another way to reduce the numerical diffusion is by coupling the geometrical reconstruction with a geometrical approximation [213] of VoF advection. The interface position is determined from interface normal and points of intersection of interface with cell faces. Geometric VoF methods usually consist of two parts. Firstly, we get the reconstructed interface based on the volume fraction field within a computational cell. Secondly, the reconstructed interface is advected using the amount of volume flux crossing the cell boundaries. The most widely used method for interface reconstruction is the piece-wise linear interface calculation (PLIC) [56]. Other notable efforts in this category are based on least-square method [224, 16, 193]. Algorithms for interface advection can be based on split or un-split schemes. The split approach is relatively straightforward in implementation because it allows having a separate solution for each spatial direction. On the other hand, unsplit schemes are computationally expensive [123] as they involve the computation of complex flux polyhedra in interface containing cells. However, un-split methods require one-step advection and reconstruction, which makes them more suitable for three-dimensional (3D) unstructured meshes. The work of Pilliod and Puckett [193] confirms that the interfaces having sharp topological changes are better resolved following an un-split algorithm. However, all these solutions are sensitive to the grid resolution, and mesh size dependency is still a big challenge.

Volume of fluid and simple line interface calculation

The simple line interface calculation (SLIC) algorithm [185] is based on the alternating-direction approach for the geometric solutions of fluid interfaces in one, two and three-dimensional problems. Fluid surfaces are calculated locally based on the volume fraction of a specific fluid in multi-fluid regions, which are simply composed of straight lines, either parallel or perpendicular to a reference coordinate. Because of the locally one-dimensional description, it is easy to advance the interface solution in time. SLIC solution can accommodate the merging and break-up of the surfaces and re-evaluate the free surface solution accordingly.

Initially, this SLIC approach [185] was only able to resolve the fluid motion on the structured grid, and the applications were limited to simple geometries. Huang et al. [112] proposed a SLIC based solution for unstructured grids and successfully tested it against the original SLIC method. Huang et al. [112] solution is based on the unstructured triangular grids, and the line segment is set parallel with one edge of the interface containing cell based on the volume fraction values in the three neighbouring cells. After finalizing this initial direction and location of the interface, the volume fraction in the next time step is calculated via the geometrical calculation of volume flux. Similarly, the time-dependent reconstruction of the interface is carried out for every time step. The algorithm is examined under four different canonical test cases [112]. To make comparison with the original structured VoF–SLIC method [185], three different grid geometries [112] are used. The numerical solution confirms that this new approach can deal with all kinds of simple flows with comparable accuracy as of VoF–SLIC method on a structured grid.

Volume of fluid and piece-wise linear interface calculation

Piece-wise linear interface calculation (PLIC) algorithm was initially proposed by Youngs for orthogonal meshes in two dimensions (2D) [279] and three dimensions (3D) [280], which calculate the interface normal from the volume fraction gradient within a computational cell. The interface normal computed in Youngs' 2D algorithm will reproduce a line regardless of cell orientation, and is second-order accurate [192]. However, a 3D algorithm reproduces a plane and is not considered second-order accurate [192, 211]. Over time, considerable developments and improvements have been made since Youngs' initial contribution [279, 280]. Addessio et al. [8] helped to extend Youngs' 2D approach for non-orthogonal grids and complex geometries. Puckett and Saltzman [200] coupled an adaptive mesh refinement (AMR) algorithm with the original Youngs' 3D method. Kothe et al. [138] work extend Youngs' 3D method to unstructured grids. They used the second-order Runge-Kutta method for time integration. Pilliod and Pucket's work [193] is considered a major contribution to having an accurate second-order solution through an unsplit time integration scheme and improved interface normal calculation.

Initially, PLIC algorithms were effectively tested against high-speed hydrodynamic calculations. Later, they are successfully extended [138, 211, 201] for the incompressible multi-phase flow applications. Despite all these improvements, these methods were challenged when the fluid structures got smaller than the mesh size. However, the improvements made by Lopez et al.[152] to the already existing PLIC formulation helped to track the fluid elements thinner than the grid size.

[211]

Volume of fluid and interface compression

This version of the VoF methodology is based on interface compression through controlling the flux across the grids rather than geometric reconstruction of the interface. The solver is part of the open-source computational toolkit OpenFOAM [119, 118] under the name of interFoam [58]. Complete details of the algorithm, transport of the indicator scalar in terms of volume fraction and solution of Navier-Strokes equations in the context of two-phase flows can be found in the work of Deshpande et al. [58]. The indicator function (volume fraction) is advected by the following equation as

$$\frac{\partial \alpha}{\partial t} + u_i \frac{\partial \alpha}{\partial x_i} - \frac{\partial}{\partial x_i}\{u_r \alpha (1-\alpha)\} = 0, \tag{2.23}$$

where u_r is the relative velocity at the face of each mesh cell and is dependent on the maximum velocity at the interface and its direction, written as

$$u_r = min(C_{comp}\frac{|\Phi_f|}{|S_f|}, max\frac{|\Phi_f|}{|S_f|})(n.S_f), \tag{2.24}$$

where Φ_f is volumetric flux, S_f is outward-pointing cell face area vector, n is the outer normal and C_{comp} is the scalar compression factor for limiting the artificial compression velocity. The third term on the right hand side of Eq. (2.23) is responsible for the interface sharpening only in the regions of interfacial boundaries, and its effects are reduced to zero in pure liquid or gas zones.

The performance of this solver is tested against the PLIC method of Rider and Kothe [211], a hybrid approach of Aulisa et al. [15] and algebraic THINC-SW algorithm of Xiao et al. [276] using three different grid sizes, namely 32^2, 64^2 and 128^2. The errors with interFoam are higher and the convergence rate is lower compared to the relatively more complex geometric and hybrid schemes. Its performance is very encouraging in the case of inertia-dominated flows ($We >> 1$). Reasonable physics can be captured, even with the lower grid resolutions. Additionally, interFoam is also evaluated for the flows having higher surface tension effects, and the resulting predictions of this solver are comparable with the balanced force method of Francois et al. [79].

Modified volume of fluid and interface compression

This method [25] is an improved version of interFoam, a sub-solver of open-source OpenFOAM library [6, 58] and termed as interPore. This is based on the compressive treatment for the interface region to have a sharp interface. The interface compression as given by Eq. (2.23) results in the abrupt change of α, which can lead to a non-physical representation of interface normal and curvature. This situation can be avoided [83] by using the smooth value of α, which is calculated as

$$\alpha_{smooth} = \frac{\sum_{f=1}^{y} (\alpha_{i+1})_f S_f}{\sum_{f=1}^{y} S_f}, \tag{2.25}$$

where y indicates the number of smoothing loops and $(\alpha_{i+1})_f$ is obtained from the linear interpolation of face-centred values. This smoothing process results in the thickness of the interface, so extra care is required to avoid non-desired effects. In some cases, additional sharpening of the interface is required [203] to have the true representation of the interface, expressed as

$$\alpha_{sharp} = \frac{1}{1 - C_{sharp}} [min(max(\alpha, 1 - \frac{C_{sharp}}{2}), 1 - \frac{C_{sharp}}{2}) - \frac{C_{sharp}}{2}], \tag{2.26}$$

where C_{sharp} is the interface sharpening coefficient and controls the unphysical behaviour of the interface by controlling the α value. The condition, $C_{sharp} = 0$, reverts the criteria to the original VoF formulation and $C_{sharp} = 1$ results in the maximum sharpening of the interface.

In a static droplet test case [25], this approach can reduce the spurious currents generation and shows less dependency on the operating parameters. In a Rayleigh–Taylor test case, this method captures the formation of instabilities and their development with success. Aboukhedr et al. [7] proposed an adaptive algorithm for the interface compression to avoid the tuning required of the relevant parameters used in the smoothing and sharpening operations. They tested this approach against a wide range of cases, starting from static interfaces to moving interfaces and the bubble generation phenomenon. The combined effects of the adaptive compression and smoothing of the surface tension [7] lead to more accurate solutions and better grid convergence behaviour.

2.3.3 Coupled level set volume of fluid (CLSVOF)

This approach was first developed by Bourlioux [29] and later modified by Sussman and Puckett [249] by combining the level set and volume of fluid methods. However, Sussman and Puckett [249] approach for coupling the LS method with the VoF is different from Bourlioux [29]. Sussman and Puckett [249] also combined the CLSVOF solution with the incompressible two-phase flow equations. Here, the continuity and momentum equations Eqs. 2.1 and 2.2 are solved following the level set approach. The unit normal vector n and curvature K are computed following Eqs. 2.6 and 2.7. Mixture density and viscosity are also calculated using the level set scalar following Eqs. 2.9 and 2.10, and the surface tension force is conditioned with a level set value via the Heaviside function as

$$F_{s,i} = \sigma \kappa \frac{\partial H}{\partial x_i}, \tag{2.27}$$

where H is a Heaviside function that behaves as a unit step function, and is defined by Eq. (2.11). Here, the solution of $\frac{\partial H}{\partial x_i}$ is similar to that of Dirac delta function δ [179], and the expectations are that they both can be used interchangeably. However, numerical tests performed by Herrmann [100] show that they are not equivalent. In the continuum surface force (CSF) model of Brackbill et al.[30], surface forces are smeared over a few cells in the interfacial regions, and therefore a smeared version of the Dirac delta or Heaviside function is preferred. Herrmann [100], Montazeri et al. [177] and Montazeri and Ward [178] suggested that instead of using a delta function for interfacial flow solutions, the use of the gradient of the Heaviside step function is helpful to avoid the generation of spurious velocities near the interfacial boundary.

To combine the effects of both VoF and LS approaches, the volume fraction is linked with the level set function via the Heaviside step function as

$$\alpha = \frac{1}{\Delta r \Delta z} \int H(\varphi) r dr dz. \tag{2.28}$$

The transport equations for LS and VoF functions can be written as

$$\frac{\partial \varphi}{\partial t} + u_i \frac{\partial \varphi}{\partial x_i} = 0, \tag{2.29}$$

$$\frac{\partial \alpha}{\partial t} + u_i \frac{\partial \alpha}{\partial x_i} = 0, \tag{2.30}$$

where the liquid volume fraction α is used to represent the free surface, same as in VoF methods. At $t = 0$, liquid volume fraction value is initiated in each computational cell, and then the governing equations for both the level set Eq. 2.29 and volume of fluid Eq. 2.30 are solved simultaneously. The advantage of representing the free surface in terms of volume fraction has accurate algorithms for advecting the volume fraction function while keeping the mass conserved and having the sharp representation of the interface. For example, Pilliod and Puckett [193] developed a second-order advection solution for VoF methods that accurately compute the rotation of a slotted disk while maintaining mass conservation. However, it is difficult to have accurate local curvature computations from volume fractions, as the volume fraction value changes rapidly in the regions of the free surface. However, LS methods can better represent local curvatures as they are simply the Laplacian of the level set function.

The main aim behind this development was to produce a more accurate and reliable solution than the LS or VoF methods. CLSVOF approach is capable of better predictions for the flows where the surface tension and rapid changes in the topology of the free surface are prominent features. Furthermore, for problems with surface tension, the CLSVOF method behaves superior to the VOF methods [27], as level set function based interface calculations are more straightforward and accurate. This method overcomes the deficiency of the volume of fluid (VoF) method in having better interface representation and holds the better mass conservation property [27], which is a matter of concern with the standard level set (LS) method. The problem with the CLSVOF approach is that it requires the parallel implementation of model transport equations comprising Navier-Stokes, level set and volume of fluid, making it computationally very expensive in cost and time. The comparative study conducted by Boniou et al. [27] confirms that computational requirements for CLSVOF and accurate conservative level set method (ACLS) [60] is quite similar but more than two times when compared with standard VoF method. However, the numerical performance of CLSVOF is much better than both ACLS and VoF.

2.4 Summary

In the past, many approaches were developed to track or capture the interface of a multiphase/immiscible flow system. Two of them, the volume of fluid (VoF) and the level set (LS), have shown promising findings and have been considered a benchmark for further research. VoF behaves well in keeping the mass conservation but has an issue with interface diffusion and requires reconstruction of the interface. Different level of numerical diffusion associated with various grid sizes leads to grid sensitivity issue. Numerical treatment is needed to have a sharper interface and to overcome grid sensitivity problems. LS method has the capability of better interface representation, but it involves interface re-initialization, which makes it computationally very expensive. It does not hold the mass conservation property, especially at the interface. The conservative level set method behaves well compared to the level set (LS) but still has a mass loss/gain issue. To overcome these deficiencies, hybrid approaches such as coupled level set volume of fluid (CLSVOF), particle level set (PLS), and refined level set grid (RLSG) were introduced. However, these hybrid methods add computational time and cost, making them unfeasible for full practical scale injectors. Performance of the robust conservative level set (RCLS) method has shown considerable attraction, especially when having unstructured grids.

A combination of geometric interface reconstruction algorithms, either SLIC or PLIC, with the VoF approach helps to have realistic interface representation and advection. The improved PLIC method of Rider and Kothe [211], a hybrid approach of Aulisa et al. [15] and algebraic THINC-SW algorithm of Xiao et al. [276] is capable of providing an accurate second-order solution for interface calculations. The modified volume of fluid (VoF) combined with the interface capturing mechanism has shown promising improvements to overcome the shortcomings of the interFoam method. However, a fully resolved solution based on VoF or LS approach for practical applications is still out of reach considering the currently available computational resources, making the need for under resolved options more important.

Over time, considerable development has been made for the numerical solutions of interfacial flows. A recent comparative study by Boniou et al. [27] confirms that the performance of CLSVOF is better than all other available interface-capturing solutions. However, no conclusive findings have been reported regarding grid independence, which is still a big challenge. In this study, an effort has been made to have a more physical representation of the liquid/gas interface, realistic solutions for the liquid jet penetration and decay rate when compared with experimental measurements, and a numerically converged solution.

Chapter 3

Volume of Fluid with Stochastic Fields Formulation

Numerical solutions for the spray atomization phenomenon usually depend on the spray region. In the near-field region, relatively few droplets are observed, and an Eulerian–Eulerian formulation is more feasible to represent the interface dynamics accurately. Most of the work regarding the LES of primary atomization [55, 24, 23, 242] do not include the sub-grid interface dynamics, and their solution behaves as under resolved DNS as they resolve the interface at LES grid level. Findings of Chesnel et al. [46, 47], Abbas et al. [5] and Chapter 5 confirm that this sub-grid contribution is essential to capture the primary atomization accurately. Inclusion of surface density [46, 47, 184] helps in having a more physical representation of the primary break-up region. The highest value of the surface density indicates the liquid jet break-up location. Volume fraction and surface density are random variables in turbulent flows, and the Eulerian stochastic fields method provides a viable means of solving the joint probability density function (PDF) of these random variables. This Chapter presents the VoF method in combination stochastic fields transported-PDF approach, initially developed by Navarro-Martinez [184] that accounts for the sub-grid fluctuations of the surface density and liquid volume fraction. The first half includes a detailed mathematical formulation of stochastic fields representation of the VoF method. In the second half, comprehensive stochastic fields and grid sensitivity analysis is conducted for three grid resolutions combined with a different number of stochastic fields. Here the work of Navarro-Martinez [184] is extended for Sydney needle spray burner [153] measurements. The convergence behaviour of stochastic fields is observed by gradually increasing the number of stochastic fields while keeping the grid resolution constant. The solution comparison of three different grid resolutions for the same number of stochastic fields is also presented. Some equations regarding the VoF method and turbulent filtered solution which were presented previously in Chapter 2 are repeated here for completeness.

3.1 Volume fraction

The VoF method is based on the idea that two immiscible fluids can be modelled as a single fluid having a single value density and dynamic viscosity at each point in space and time that are linear functions of the liquid volume fraction value, α, given as

$$\rho = \rho_l \alpha + \rho_g (1 - \alpha), \tag{3.1}$$

$$\mu = \mu_l \alpha + \mu_g (1 - \alpha), \tag{3.2}$$

where the subscripts l and g indicate properties in the liquid and gas phases, respectively. In general form, the single fluid transport equations for continuity, momentum and volume fraction are

$$\frac{\partial \rho}{\partial t} + \frac{\partial \rho u_i}{\partial x_i} = 0, \tag{3.3}$$

$$\frac{\partial \rho u_i}{\partial t} + \frac{\partial \rho u_i u_j}{\partial x_i} = -\frac{\partial p}{\partial x_i} + \frac{\partial \tau_{ij}}{\partial x_i} + F_{s,i} + \rho g_i, \tag{3.4}$$

$$\frac{\partial \rho \alpha}{\partial t} + \frac{\partial \rho u_i \alpha}{\partial x_i} = 0. \tag{3.5}$$

Here, u, p and g denote velocity, pressure and gravitational acceleration, respectively. t is time and x_i is the spatial coordinate in the ith direction. For Newtonian fluids, the viscous stress is given by

$$\tau_{ij} = \mu \left[2S_{ij} - \frac{2}{3} \frac{\partial u_k}{\partial x_k} \delta_{ij} \right], \tag{3.6}$$

where

$$S_{ij} = \frac{1}{2} \left(\frac{\partial u_i}{\partial x_j} + \frac{\partial u_j}{\partial x_i} \right), \tag{3.7}$$

is the strain-rate tensor and δ_{ij} is a Dirac delta. The volume fraction takes the value of $\alpha = 1$ and $\alpha = 0$ in the liquid and gas phases, respectively, and for immiscible fluids the real interface is sharp. Eq. (3.5) has no molecular diffusion term but numerical diffusion produces locations where $0 < \alpha < 1$ such that the interface is artificially smeared. Then a continuum surface tension model can be used [30],

$$F_{s,i} = \sigma \kappa n_i \delta_s, \tag{3.8}$$

where σ is the surface tension coefficient, $\kappa = -\nabla \cdot \mathbf{n}$ is the interface curvature found through the unit normal vector $\mathbf{n} = \frac{\nabla\alpha}{|\nabla\alpha|}$, and $\delta_s = |\nabla\alpha|$ is an interface detecting function.

3.2 Surface density

During the last three decades, various solutions have been proposed to describe the spray regions uniformly. The Eulerian-Lagrangian spray atomization (ELSA) model developed initially by [263] is an important contribution to modelling the atomization phenomenon. It is beneficial in predicting the velocities and sizes of liquid droplets. However, the DNS findings of Lebas et al. [144] confirm that it is impossible to represent the liquid phase as a set of droplets in the primary break-up regions, and there is a need for relevant physical variables which can be used to characterize this near-field zone. Surface density, which is a direct measure of the local interfacial area, is an important physical parameter that can be applied for primary atomization characterization. Morel [180] defined the local surface density in terms of a generalized function which helps have a solution for the problem. Despite this theoretical progress, the general form of the surface density equation, in either filtered or averaged form, contains unclosed terms that require modelling. Initially, Vallet and Borghi [263] proposed an equation for the mean liquid surface density following the similar analogy proposed by Marble and Broadwell [160] for the flame surface density. Lebas et al. [144] suggested that the benefit of this surface density equation is to avoid any assumption concerning the shape of the liquid surface. So far, we do not have the proper closure models which are able to offer reasonable surface density solutions for all spray atomization regimes. The available solution to close the surface density equation considered that the spray drops are spherical in shape, and the corresponding diameter distribution is obtained via the classical models for break-up, collision and coalescence. The required surface density equation is obtained by integrating the second moment of this distribution [137]. Furthermore, these solutions also assume that all droplets are of identical shape, and their diameter distribution is obtained from the liquid volume fraction and the surface density values.

The ELSA solution is based on the surface density variable instead of droplet sizes. The model solves the two Eulerian equations: one for the liquid volume fraction and the second for the surface density. The ELSA formulation can provide the more relevant quantities for spray phenomena such as Sauter Mean Diameter (SMD) from the simple relations between surface density and liquid volume fraction. Chesnel et al. [47] presented an LES based variant of the ELSA approach that needs closure for the production and destruction of the filtered surface density. Turbulence behaviour, jet break-up and droplet collision can generate and destroy surfaces.

In three-dimensional immiscible flows, the liquid-gas interface can be represented by the root of a smooth function $\Psi(x,t)$. The interface normal based on this smoothed function can be calculated by $n = -\frac{\nabla\Psi}{|\nabla\Psi|}$, with the convention that the direction of the interface is considered towards the gas phase. The smoothed function Ψ follows a convective equation dependent on the interface velocity and is expressed as

$$\frac{\partial\Psi}{\partial t} + u'_i \frac{\partial\Psi}{\partial x_i} = 0, \tag{3.9}$$

where the interface velocity, u'_i, is defined as

$$u'_i.n = \frac{\partial\Psi/\partial t}{|\nabla\Psi|}. \tag{3.10}$$

A phase indicator function $\Gamma(x,t)$ in the form of Heaviside function, defined as

$$\Gamma = H(x-x'), \tag{3.11}$$

where x' indicates the interface location, H is a Heaviside function that behaves as a step function, and its value is

$$H(x-x') = \begin{cases} 1 & \text{if } (x-x') > 0 \\ 0 & \text{if } (x-x') \leq 0 \end{cases}. \tag{3.12}$$

The gradient of the indicator function defined above leads to

$$\nabla\Gamma = \nabla H(x-x') = -\delta(\Psi)\nabla\Psi, \tag{3.13}$$

where δ is the characteristic function. Considering the definition of n, Eq. (3.13) can be re-written as

$$\nabla\Gamma = -\delta(\Psi)n|\nabla\Psi| \rightarrow n.\nabla\Gamma = -\delta(\Psi)|\nabla\Psi|. \tag{3.14}$$

The fine-grained surface density termed as interface Dirac delta function is defined by

$$\delta^{l} \equiv -\delta \nabla \Gamma, \tag{3.15}$$

having units of m^{-1}. The governing equation for δ^{l} based on the flow field [161, 148] is written as

$$\frac{\partial \delta^{l}}{\partial t} + u_j \frac{\partial \delta^{l}}{\partial x_j} = -\delta^{l} n_i n_j \frac{\partial u_i}{\partial x_j}. \tag{3.16}$$

The surface density Σ can be obtained by integrating δ^{l} over the infinitesimal value of δV as

$$\Sigma(x,t) = \frac{1}{\delta V} \int_V \delta^{l} dV = \frac{1}{\delta V} \int_I dS = \frac{\delta S^{I}}{\delta V}. \tag{3.17}$$

Eq. (3.17) explains that surface density is the amount of spatial surface per unit volume at a given time and spatial position. This is based on the concept of Candel and Poinsot [36] used in the context of premixed combustion to define the volumetric flame surface density. The convolution of δ^{1} with any smooth function f leads to

$$\frac{1}{\delta V} \int_V \delta^{l} f(x,t) dV = \frac{1}{\delta V} f(x^{I},t) \delta S^{I} \equiv f^{I} \Sigma, \tag{3.18}$$

where the superscript I represents its evaluation at the liquid-gas interface. The interfacial surface density equation is obtained by integrating the Eq. (3.16) over a small volume and using Eq. (3.18) as

$$\frac{\partial \Sigma}{\partial t} + \frac{\partial u_j^{I} \Sigma}{\partial x_j} = -\frac{1}{\delta V} \int_V \delta^{l} n_i n_j \frac{\partial u_i}{\partial x_j} dV. \tag{3.19}$$

The integral part on the right hand side of Eq. (3.19) represents the stretching of the surface because of velocity gradients and interface curvature. As the interface normal is not a continuous function, its erratic behaviour would be visible in the liquid break-up, fragmentation and coalescence. It is recommended here [184] that the integral should be calculated over a very small volume which leads to no sub-volume velocity scales. Considering that no mass transfer across the interface will lead to $u = u^{I}$. Following [195, 268], the final equation for the surface density will take the form of

$$\frac{\partial \Sigma}{\partial t} + \frac{\partial u_j \Sigma}{\partial x_j} = -\Sigma n_i n_j \frac{\partial u_i}{\partial x_j}. \tag{3.20}$$

Eq. (3.20) along with Eq. (3.5) are the main governing equations solved here in this Chapter. A simple solution can be made for very dilute flow applications where droplet sizes are smaller than cell sizes. There are several formulations available in the literature provided by [137, 180, 129] for the solution of the Eq. (3.20), but those are limited to high Weber number flows. Using the spatial averaging operator $\widehat{.}$ in the averaged surface density solution leads to the necessity of new models to account for droplet break-up and coalescence. Nearly all the models available so far follow the similar closure, initially proposed by [115] and then tailored explicitly for the atomization phenomenon by [263], written as

$$\frac{\partial \widehat{\Sigma}}{\partial t} + \bar{u}_j \frac{\partial \widehat{\Sigma}}{\partial x_j} = S_g - S_d \equiv S, \tag{3.21}$$

here S_g represents the generation of surfaces as a result of the break-up process and S_d denotes the destruction of surfaces because of droplet collision, coalescence and amalgamation. The modelling of source term S is based on the correlation of turbulence phenomenon and related time scales. Jay et al.[122] presented a quadratic solution for this source term which is written as

$$S = a\widehat{\Sigma} - b\widehat{\Sigma}^2, \tag{3.22}$$

where coefficient a is the inverse of turbulent time scales, and coefficient b depends on the flow field, droplet volume and their orientations. The first term on the right side of the above equation corresponds to the generation of surfaces in near-field regions where the growth of instabilities takes place and is followed by non-linear processes as explained by Jay et al. [121, 122]. The second term accounts for the reduction of surface area in far-field regions because of droplet coalescence, collisions and amalgamation [144]. In context of equilibrium restoration [263, 144, 22], the source term expressed in Eq. (3.22) can be written as

$$S = \frac{\widehat{\Sigma}}{\tau}\left(1 - \frac{\widehat{\Sigma}}{\widehat{\Sigma}_{eq}}\right), \tag{3.23}$$

where $\widehat{\Sigma}_{eq}$ represents the equilibrium surface density and τ is the corresponding turbulent time scale. Estimation of $\widehat{\Sigma}_{eq}$ is based on the assumption of equilibrium of surface energy with the local kinetic energy. Considering the flows are isothermal and viscous stresses are negligible, locally equilibrium surface density can be written as

$$\widehat{\Sigma}_{eq} = \frac{\rho k \alpha}{\sigma}, \tag{3.24}$$

where k represents the kinetic energy. The value of critical Weber number $We^* = \frac{\rho k \alpha}{\sigma \widehat{\Sigma}_{eq}}$ for dense regions is considered as $We^*_{den} \approx 1$ as suggested by [263, 144]. However, some studies [156, 69] suggested that this value could be in the range of 1-3. In far-field (dilute) regions, where surface generation by the droplet break-up and destruction by coalescence take place, a relevant We^*_{bkp} is needed. Study performed by [209] confirms that its value is nearly constant, $We^*_{bkp} \approx 12$, for the low value of liquid Ohnersorge numbers, $Oh < 1$,. Similarly, we need the critical Weber number value We_{col} to account for droplet collisions and can be calculated from the Sauter mean diameter d_{32} [144]. From the analysis of various collision models [156], it is found in the range of $We^*_{col} \approx 12 - 15$ for spherical droplets and $We^*_{col} \approx 3.5$ for the case of non-spherical droplet collisions. It is found [47] that surface density depends on the critical value of Weber number We^*, and there is a need to have a single definite value.

Each phenomenon corresponding to the relevant surface generation during the break-up processes (S_{bkp}) or surface destruction because of collision of droplets (S_{col}) is dependent on the associated time scale. Turbulent break-up time scales are calculated as $\left(\frac{k_\tau}{\varepsilon}\right)$ in RANS context and as $||S_{ij}||^{-1}$ in LES calculations. Particle collision theory [263] is helpful to calculate the τ_{col}, whereas τ_{bkp} is calculated from Pilch and Erdman work [191]. In general ELSA-RANS spray formulation [22, 144] surface density is calculated based on dense region (S_{den}), collision (S_{col}) and beak-up (S_{bkp}) values. To combine all three into a single value, each phenomenon is related to an indicator function in order to distinguish dilute/dense regions. This indicator function is based on the local volume fraction value α.

The model explained in Eq. (3.23) does not behave well when the surface is at rest, which leads to zero value of equilibrium surface density Eq. (3.24) and the surface will be destroyed in no time. The presence of interface in an interfacial flow indicates that there should be a minimum surface present even at rest. Eq. (3.17) indicates that the minimum surface density is inversely proportional to the size of the integration kernel h. In their RANS simulations [263, 22], surface boundary condition were based on the condition of having the minimum surface density as $\Sigma_{min} \approx 1$. Lebas et al. [144] used the expression dependent on liquid volume fraction α and turbulent length scale l_τ, written as $\Sigma_{min} \approx \frac{\alpha(1-\alpha)}{l_\tau}$ with having an additional source term S_{int} in order to generate the surface at the boundaries. Later on Chesnel at el. [47] suggested that $\Sigma_{min} \propto \frac{\sqrt{\alpha(1-\alpha)}}{h}$ and use of S_{int} can be avoided by considering $\Sigma = \Sigma' + \Sigma_{min}$ leading to an improved equilibrium surface density relation, written as $\Sigma^*_{eq} = \Sigma_{eq} + \Sigma_{min}$. For near-field regions, the modified expression for equilibrium surface density is

$$\Sigma^*_{eq} = \frac{\rho k \alpha}{\sigma} + C_\Sigma \frac{\sqrt{\alpha(1-\alpha)}}{h}. \tag{3.25}$$

Based on his DNS findings, Chesnel [46] finds that the optimal value of constant C_Σ is 2.4. Eq. (3.25) indicates that $\Sigma_{min} > \Sigma_{eq}$ when the local Weber number, $We_h = \frac{\rho k h}{\sigma}$ is smaller than the critical mesh Weber number, $We_{h,crt} = C_\Sigma \frac{\sqrt{(1-\alpha)}}{\alpha}$. For near-field regions having value of liquid volume fraction $\alpha > 0.1$, the value for $We_{h,crt} \approx 7$. Both for *RANS* and *LES* atomization studies, $We_h >> We_{h,crt}$ and then Σ_{min} value becomes less important. However, in far-field regions having very dilute flow at a lower Weber number, Σ_{min} can not be neglected.

3.3 Joint probability density function approach for α and Σ

Following the transported PDF concepts reviewed in depth by Pope [194] and Haworth [96], Navarro-Martinez [184] extended this method for the solution of liquid volume fraction and surface density. Specifically, Navarro-Martinez [184] developed equations for the joint sub-grid PDF (sometimes called filtered density function, FDF) of these quantities. The starting point for the derivation is the concept of turbulence filtering and fine grained PDFs. To have the spatial filtering for a function $y = y(x,t)$ in terms of its convolution with a filter function,G, we can write

$$\bar{y} = \int_V y(x',t) G(x - x', t; \Delta) dV', \tag{3.26}$$

here Δ denotes the filter width corresponding to the filter function, which is considered positive to have positive filtered values of positive definite functions y. A fine-grained characteristic function following Klimenko and Bilger [135] can be defined as

$$\Psi(x,t;\bar{\theta}) = \delta[\theta_1 - \alpha(x,t)]\delta[\theta_2 - \Sigma(x,t)], \tag{3.27}$$

where $\bar{\theta} = (\theta_1, \theta_2)$ represents the sample space vector for both α and Σ respectively. Following the filtering operation expressed in Eq. (3.26), a sub-grid joint probability density function, P_{sgs}, of volume fraction α and surface density Σ is written as

$$P_{sgs}(x,t;\bar{\theta}) = \int_V \Psi(x',t)J(x-x',t;\Delta)dV', \tag{3.28}$$

where the term $P_{sgs}(\theta_1, \theta_2)d\theta_1 d\theta_2$ gives the probability of $\theta_1 < \alpha < \theta_1 + d\theta_1$ and $\theta_2 < \Sigma < \theta_2 + d\theta_2$ within the filter width at a given point in relavant space and time. Following the rule of differentiation for generalised functions [82, 268], a PDF equation can be derived from Eqs. (3.5) and (3.20), expressed as

$$\frac{\partial P_{sgs}}{\partial t} + \frac{\partial \overline{\langle u_j|\bar{\theta}\rangle} P_{sgs}}{\partial x_j} + \frac{S_k(\bar{\theta})P_{sgs}}{\partial \theta_k} = 0, \tag{3.29}$$

and the corresponding source terms are calculated from Eq. (3.20). A closure model is needed for the conditionally filtered velocity $\overline{\langle u|\bar{\theta}\rangle}$. This is achieved from the resultant of three contributions (filtered, turbulent diffusion and surface density), written as

$$\overline{\langle u_j|\bar{\theta}\rangle} P_{sgs} = \bar{u}_j P_{sgs} - D_{sgs}\frac{P_{sgs}}{\partial x_j} - u^s_j(\theta_2)P_{sgs}. \tag{3.30}$$

The above equation is based on the Herrman and Gorokhovski work [103] for the sub-grid velocity decomposition in LES modelling of multiphase flows. The first term on the right hand side of Eq. (3.30) represents PDF transport by the filtered velocity, and the second is the PDF transport by sub-grid turbulent diffusion based on the gradient model of Schmidt and Schumann [225]. This is considered a standard procedure in LES-PDF for combustion processes [126]. There are chances that this gradient model could not be perfect because of the sub-grid counter gradient transport, but currently, there are no alternatives available for the PDF solutions. Closures based on the Smagorinsky model could be inadequate [141] near the interface, and a scale similarity model [47] seems a good option. However, implementation of the similarity model along with PDF formulation is complex, and Smagorinsky model based closures are used here. It is also noted that the new EVD model presented in Chapter 5 provides a novel sub-grid closure that may be used within the context of PDF methods, but this is out of scope for the current project. Sub-grid diffusivity, D_{sgs}, is proportional to the sub-grid turbulent viscosity , ν_{sgs}, written as

$$D_{sgs} = \frac{\nu_{sgs}}{Sc_{sgs}}. \tag{3.31}$$

The last term on the right side of Eq. (3.30) accounts for restorative velocity, which is considered dependent on the surface density. Assuming that $u^s \approx B\overrightarrow{\nabla}\Sigma$, where $B = \frac{\sigma}{T}\sigma V J$ with σ is surface tension force, T is temperature, V is volume, and J is Onsanger kinetic coefficient between thermodynamic forces and fluxes [35], we can write

$$\frac{\partial u_j^s P_{sgs}}{\partial x_j} \approx \frac{\partial S_d P_{sgs}}{\partial \theta_2}. \tag{3.32}$$

Here $S_d = B(\nabla\Sigma)^2$ is an unclosed term which represents the destruction of surface density. This term behaves similar to micromixing or scalar dissipation which is based on the molecular diffusion [194] and becomes negligible when the surfaces are at equilibrium. In current studies, the same model is assumed for S_d as used for conventional ELSA formulations, written as

$$S_d(\theta_2) = \frac{1}{\tau}\left(\frac{\theta_2}{\Sigma_{eq}^*}\right)\theta_2, \tag{3.33}$$

where this model is directly linked with sample space θ_2 without considering the physical scales. It is assumed that the phase space is always in dense condition and the corresponding value of the critical Weber number is $We^* \approx 1$. Σ_{eq}^* is calculated using Eq. (3.25). The equilibrium time-scale τ is taken as the same as for S_g, written as

$$\frac{1}{\tau} = \frac{|S_g|}{\theta_2}. \tag{3.34}$$

We can only have considerable values for S_g and S_d if there is certainity of liquid volume $\theta_1 > 0$ and surface density $\theta_2 > 0$.The final transport equation for the sub-grid joint PDF, including both surface generations and surface destructions, is written as

$$\frac{\partial P_{sgs}}{\partial t}+\frac{\partial \bar{u}_j P_{sgs}}{\partial x_j}=\frac{\partial}{\partial x_j}\left[D_{sgs}\frac{\partial P_{sgs}}{\partial x_j}\right]-\frac{S_g(\bar{\theta})P_{sgs}}{\partial \theta_2}+\frac{S_d(\bar{\theta})P_{sgs}}{\partial \theta_2}. \tag{3.35}$$

The current study is based on a joint-scalar PDF approach and the formulation can be extended for evaporative flows by adding new terms, including the loss of liquid fraction and surface destruction because of the evaporation process.

3.4 Stochastic solution for joint PDF of α and Σ

Various solutions are possible for the joint sub-grid PDF given in Eq. (3.35), which can be treated similar to the Fokker-Planck equation. This equation can be solved directly following the Eulerian approach [78] by solving a small set of moments. Stochastic methods have been proved [67, 184, 44] as a better alternative as they are computationally less expensive. These stochastic solutions could be of Lagrangian nature, when the stochastic particles are tracked within the whole domain [196], or Eulerian, when the stochastic fields are solved on a finite difference / finite volume grid producing a differentiable solution in space, although not differentiable in time [262]. For the solution of multiphase flows, the stochastic field methods have been successfully applied to cavitating flows [67, 44] and atomization [184].

In the Lagrangian particle approach, we solve an equivalent set of Stochastic Differential Equations (SDE) for the Lagrangian particles, which have the same number of moments as of basic PDF system Eq. (3.35). However, in the Eulerian Stochastic Fields method, an equivalent set of Stochastic Partial Differential Equations (SPDE) is solved. The resultant moments are the same order as Eq. (3.35). Mustata et al. [183] developed this approach in LES context, and since then has been successfully used for a number of problems [125, 124, 32, 62, 67]. The computational cost for both stochastic fields and stochastic particles vary linearly and are cheaper than finite difference methods but about the same cost as each other. In the context of the Eulerian stochastic fields or Lagrangian stochastic particles approach, an equivalent PDF for the N fields can be written as

$$P_{sgs}=\frac{1}{N}\sum_{a=1}^{N}\delta\left[\theta_1-\alpha^a(x,t)\right]\delta\left[\theta_2-\Sigma^a(x,t)\right], \tag{3.36}$$

where α^a and Σ^a represent liquid volume fraction and surface density for each stochastic field. Two solutions are possible for the equivalent SPDE representation based on the interpretation of the stochastic integral. The first solution is obtained using the Ito approach as implemented by Valino [262], and the second possible solution can be made using the Stratonovich method as implemented by Sabel’nikov and Soulard [217]. The Ito formulation is adopted here, and the comparison of Ito-Stratonovich stochastic field implementation is beyond the scope of this study. The work of Jones and Navarro-Martinez [126] has shown little difference when applied in the context of turbulent combustion. Following the Ito based solution, corresponding stochastic fields transport equations are

$$\frac{d\alpha^a}{dt}+\bar{u}_j\frac{\partial \alpha^a}{\partial x_j}=\frac{\partial}{\partial x_j}\left[D_{sgs}\frac{\partial \alpha^a}{\partial x_j}\right]+\sqrt{2D_{sgs}}\frac{\partial \alpha^a}{\partial x_j}dW_j^a, \tag{3.37}$$

$$\frac{d\Sigma^a}{dt}+\bar{u}_j\frac{\partial \Sigma^a}{\partial x_j}=\frac{\partial}{\partial x_j}\left[D_{sgs}\frac{\partial \Sigma^a}{\partial x_j}\right]+\sqrt{2D_{sgs}}\frac{\partial \Sigma^a}{\partial x_j}dW_j^a+S_g^a-S_d^a, \tag{3.38}$$

where dW^a represents the Wiener processes having mean value of 0 and variance of $\sqrt{dt}$. The notation $d\alpha^a$ indicates that the stochastic fields are differentiable in space but are not continuous in time. Filtered values are obtained from the averaged stochastic fields solution, written as

$$\bar{\alpha}=\frac{1}{N}\sum_{a=1}^{N}\alpha^a. \tag{3.39}$$

Following a similar procedure, we can have higher moments of α and Σ. Stochastic fields solution given by Eqs. (3.37) and (3.38) can be transformed into Chesnel et al. [47] filtered transport equations by averaging over a large number of stochastic fields, written as

$$\frac{\partial \bar{\alpha}}{\partial t}+\bar{u}_j\frac{\partial \bar{\alpha}}{\partial x_j}=\frac{\partial}{\partial x_j}\left[D_{sgs}\frac{\partial \bar{\alpha}}{\partial x_j}\right], \tag{3.40}$$

$$\frac{\partial \bar{\Sigma}}{\partial t}+\bar{u}_j\frac{\partial \bar{\Sigma}}{\partial x_j}=\frac{\partial}{\partial x_j}\left[D_{sgs}\frac{\partial \bar{\Sigma}}{\partial x_j}\right]+\overline{S_g}-\overline{S_d}. \tag{3.41}$$

Calculating filtered moments from a stochastic solution incorporates an error that increases with the increase in sub-grid variance and decreases with the increase in the number of stochastic fields. Increasing the number of stochastic fields leads to the higher computational time required for the numerical solution [257, 256]. Computational cost limits the maximum number of stochastic fields used within each LES cell, increasing exponentially with the number of LES cells and linearly with the stochastic fields used. Using more stochastic fields permits a better statistical description of the sub-grid structures at a lower computational cost when compared with the grid refinement [257].

3.5 Turbulent filtering of Navier–Stokes equations

A conceptually simple and commonly adopted for the turbulent treatment of continuity and momentum equations [34, 54, 47, 184, 130] is to spatially filter Eqs. (3.3) and (3.4), and close the combined interfacial and turbulent sub-grid fluctuations through conventional turbulent viscosity models. Here, a basic top-hat filter [267] is used, and the filter size is set as the cube root of the grid volume, written as

$$\Delta = \sqrt[3]{\Delta_x \Delta_y \Delta_z}, \tag{3.42}$$

where the subscripts x, y, z represent the length of the grid cell in each direction of Cartesian space. Linking the LES filter to the grid introduces numerical dependence into the modelling, but with a few exceptions [53, 222], this is common in LES due to its numerical practicality.

After simplifying Eqs. (3.3) and (3.4) for incompressible flows in which the single fluid density is a linear combination of constant liquid and gas densities [107, 259], and then spatially filtering them over Δ, the filtered transport equations become

$$\frac{\partial \bar{u}_i}{\partial x_i} = 0, \tag{3.43}$$

$$\frac{\partial \bar{\rho} \bar{u}_i}{\partial t} + \frac{\partial \bar{\rho} \bar{u}_i \bar{u}_j}{\partial x_i} = -\frac{\partial \bar{p}}{\partial x_i} + \frac{\partial \bar{\tau}_{ij}}{\partial x_i} + \bar{F}_{s,i} + \bar{\rho} g_i - \frac{\partial \tau_{ij}^{tf}}{\partial x_i} + f_{\rho,i}^{tf} + f_{\mu,i}^{tf}. \tag{3.44}$$

Here, the overbar, $\bar{\cdot}$, denotes conventional Reynolds filtering. The first, second and fourth terms on the right hand side of Eq. (3.44) are in closed form with the resolved viscous stress expressed as

$$\bar{\tau}_{ij} = \overline{\mu} \left[2\bar{S}_{ij} - \frac{2}{3} \frac{\partial \bar{u}_k}{\partial x_k} \delta_{ij} \right]. \tag{3.45}$$

Closure models are required for the remaining terms in Eq. (4.6) along with the term on the right hand side of Eq. (4.7). The filtered surface tension force is decomposed into resolved and sub-grid parts as

$$\bar{F}_{s,i} = \sigma \bar{\kappa} \bar{n}_i \left| \nabla \bar{\alpha} \right| + F_{s,i}^{tf}, \tag{3.46}$$

where the superscript ^{tf} denotes the sub-grid component due to the filtering of turbulent fluctuations. $\bar{\kappa}$ and $\bar{n}_i$ denote the curvature and the ith component of the unit vector indicating the normal direction of the resolved interface with $\bar{\kappa} = -\nabla \cdot \bar{n}$ and $\bar{n} = \nabla\bar{\alpha}/\left|\nabla\bar{\alpha}\right|$, respectively. DNS data of spray atomization [46] has revealed that $\mathbf{F}_s^{tf}$ is generally small compared to the other terms in the momentum equation, and therefore the sub-grid part of the filtered surface tension force is usually neglected [47, 184, 12]. The sub-grid turbulent stress is closed with the gradient of the viscous term, written as

$$\tau_{ij}^{tf} = \overline{\rho u_i u_j} - \bar{\rho}\bar{u}_i\bar{u}_j = -2\bar{\rho}\nu_t\bar{S}_{ij}. \tag{3.47}$$

Various models are possible for ν_t. Here, the Smagorinsky model [237] has been usually used,

$$\nu_t = C_s\Delta^2\sqrt{2\bar{S}_{ij}\bar{S}_{ij}}, \tag{3.48}$$

with the constant $C_s = 0.0197$ [225]. The final two terms in Eq. (3.44) are correlations induced by sub-grid fluctuations of density and viscosity, written as

$$f_{\rho,i}^{tf} = \frac{(\partial\bar{\rho}\bar{u}_i - \overline{\rho u_i})}{\partial t}, \tag{3.49}$$

$$f_{\mu,i}^{tf} = \frac{\partial\left(\overline{2\mu S_{ij}} - 2\bar{\mu}\bar{S}_{ij}\right)}{\partial x_i}. \tag{3.50}$$

Usually, [47, 184, 12] these are neglected or considered to be encompassed by the model for sub-grid turbulent stress. To calculate the filtered values of density and viscosity and link them with the PDF solution, we can write

$$\bar{\rho} = \bar{\rho}_l\bar{\alpha} + \bar{\rho}_g(1-\bar{\alpha}), \tag{3.51}$$

$$\bar{\mu} = \bar{\mu}_l\bar{\alpha} + \bar{\mu}_g(1-\bar{\alpha}), \tag{3.52}$$

where the value of $\bar{\alpha}$ is obtained from the stochastic field solutions using Eq. (3.39).

3.6 Numerical solution and implementation

The solution of the model equations is dependent on the discretization process which could be based on finite difference [127], finite element [97, 186, 233] or finite volume [105, 107] methods. Considering each method's specific advantages and disadvantages, mathematical formulations for two-phase flows, possibilities for easy solver writing, transparent parallelization and availability of free access to basic code requirements, the cell-centered finite volume method is used [117]. The LES-PDF solution is implemented in OpenFOAM and Klein's digital filter [134] is used to generate realistic turbulent fields at the liquid and air injection planes. Klein's digital filter is based on the digital filtering of random data and can reproduce the desired statistics with second-order accuracy along with auto-correlation functions. In the test cases investigated here, the maximum interface Courant number is $Co_i = 0.25$, but since the numerical method integrates the volume fraction over four sub-steps, it is effectively 0.0625. At the same time the maximum flow Courant number is $Co_f = 0.75$. In this study PIMPLE algorithm is followed for pressure velocity coupling. The pressure equation is solved twice during each momentum correction operation, and this momentum correction takes place twice in each time step. Here, we have used a PCG solver pre-conditioned by DIC for volume fraction, a GAMG solver with smoother GaussSeidel for pressure calculations, and a PBiCGStab solver pre-conditioned by DILU for surface density, velocity, energy dissipation and viscosity fields.

The computational domain is a three-dimensional cylinder of length $L_x = 50$ mm and diameter $D_{in} = 5$ mm. The mean flow boundary conditions are set according to Table 3.1. The turbulence intensity of the air blast is $0.11U_g$, which is the same as the experimentally observed value. For the liquid jet, the turbulence intensity is $0.0525U_l$, which is a characteristic value for turbulent pipe flow. The integral length scales are prescribed as $0.125d_j$ and $0.125D$ for the liquid and air-blast flows, respectively. Note that to reduce the computational cost, the air-blast stream diameter in the computations is half the experimental diameter. However, to ensure that the atomization modelling is not unduly affected, the integral length scale in the simulations is based on the experimental air-blast diameter. Here, the LES grids are suggested to resolve the integral length scales of the air and liquid fluids [184], which is an equivalent standard for LES of single-phase flows [116]. Three LES meshes are used for testing numerical convergence. The liquid jet diameter is resolved by 14, 18 and 24 cells, respectively. The annular gap is resolved by 40, 50 and 62 cells, respectively, and the expansion ratio of the largest and smallest cell size is 1.5. This results in characteristic cell widths near the most important interface region being 49 μm, 38 μm and 30 μm. The domain length in the axial direction is discretized by 1000, 1250 and 1575 cells, respectively, that satisfy the cell lengths in the axial direction, almost the same as the characteristic cell widths near the interface region. This grid scheme leads to three LES meshes containing 1.1, 2.3 and 4.5 million cells, respectively. The schematic of the mesh with 2.3 million cells depicting the mesh resolutions is shown in Fig. 3.1. Twelve simulations are performed in total as set out in Table 3.2. Four simulations are performed for each mesh resolution with a combination of the different number of stochastic fields. They are named according to the number of LES cells and the number of stochastic fields.

Table 3.1 Flow parameters for the N-AS2 spray case.

Case	N-AS2
U_g [m/s]	36
U_l [m/s]	4.3
Re_g	21398
Re_l	7491
We	35

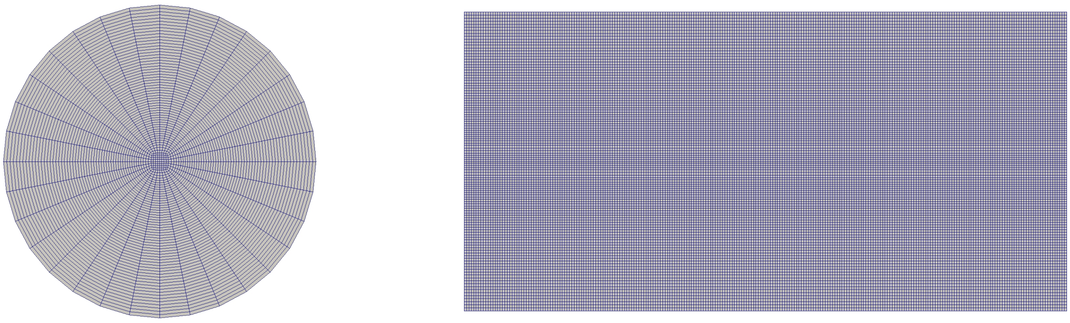
(a) Axial view

(b) Side view

Fig. 3.1 Axial and side views of the mesh scheme at the corresponding cross areas of the computational domain.

3.7 Experimental set-up and data selection for validation

The numerical computations are performed for air-blast acetone spray jets (designated N-AS2) that have been investigated experimentally on the Sydney needle spray burner [153] which is shown schematically in Fig. 3.2. High-quality experimental data is available for axial profiles of the mean volume fraction, which is measured by the two-angle backlit imaging method [236].

The burner has concentric liquid, air-blast and pilot streams. The pilot is not modelled in the present study of non-reacting atomization. The acetone is injected from a needle with a diameter of $d_j = 686\mu m$ and the air-blast tube has a diameter of $D = 10mm$. The needle can be recessed below the exit plane of the air-blast tube, but for the N-AS2 and N-AS8

Table 3.2 List of numerical simulations.

Number of cells in millions	Number of stochastic fileds	Case Name
1.1	4	1.1M,4SF
1.1	8	1.1M,8SF
1.1	16	1.1M,16SF
1.1	32	1.1M,32SF
2.3	4	2.3M,4SF
2.3	8	2.3M,8SF
2.3	16	2.3M,16SF
2.3	32	2.3M,32SF
4.5	4	4.5M,4SF
4.5	8	4.5M,8SF
4.5	16	4.5M,16SF
4.5	32	4.5M,32SF

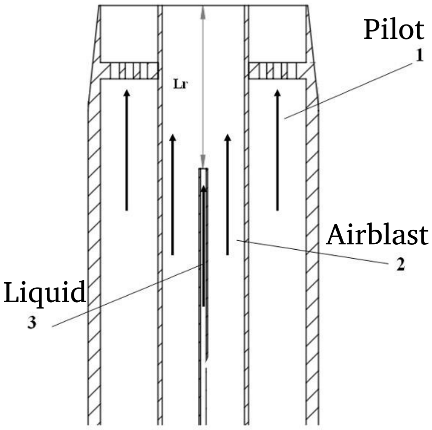

Fig. 3.2 Schematic drawing of the Sydney needle spray burner. Reprinted from Combustion and Flame, Vol 176, A. Lowe, A. Kourmatzis, A.R. Masri, Turbulent spray flames of intermediate density: Stability and near-field structure, Pages 511-520, Copyright (2017), with permission from Elsevier.

cases, the needle and air-blast exit planes are flush. The densities of air and liquid acetone are $\rho_g = 1.178$kg/m^3 and ρ_l= 784.5kg/m^3 and their kinematic viscosities are $\nu_g = 1.567$e-5m^2/s and $\nu_l = 3.938$e-7m^2/s. The flow parameters for the spray are given in Table 3.1. The mean burner exit plane velocities in the air-blast and acetone streams are U_g and U_l, respectively, while $Re_g = U_g\left(D-d_j\right)/\nu_g$ and $Re_l = U_l d_j/\nu_l$ are the corresponding Reynolds numbers, and $We = \rho_g\left(U_g-U_l\right)^2 d_j/\sigma$ is the jet Weber number based on the interfacial drift velocity. The surface tension coefficient of the acetone-air interface is specified as 0.023N/m.

3.8 Results

A detailed investigation of the grid resolution and stochastic field sensitivity for the three different resolutions is presented here in this Section. Comparisons are also made to the limited amount of available experimental data. Results are first presented for instantaneous volume fraction fields representing the jet penetration and decay rate, mean and rms values of liquid volume fraction, followed by surface density and velocity profiles. Results are also presented for the joint PDF volume fraction and surface density fields. For these calculations, three-dimensional rectangular regions are selected at five different locations along the jet having the width of two liquid jet diameters, 2d, and length of one air-blast diameter, 1D, conditioned with liquid volume fraction value as $0.01 \leq \alpha \leq 0.99$. In the end, the grid convergence behaviour for 1.1M, 2.3M and 4.5M LES cells resolution is presented using four combinations of stochastic fields.

3.8.1 Stochastic field sensitivity

1.1M LES cells

Figure 3.3 shows instantaneous snapshots of the filtered volume fraction fields on 1.1M LES grids for case N-AS2 with the 4,8,16 and 32 stochastic fields. The amplitude of the wave instability gradually increases, followed by the break-up of the jet and the evolution of discrete ligaments. With the increase in the number of stochastic fields, numerical diffusion is reduced. The interface is more diffusive, especially around the break-up location. The appearance of a discrete liquid structure arises a bit further upstream for a lesser number of stochastic fields. Here, we can observe the continuous structures even in the downstream regions for 32 stochastic fields. These instantaneous plots show that results are much more sensitive to stochastic fields and do not produce the converged solution up to 32 stochastic fields.

The mean and rms of volume fraction in the axial and radial directions for 1.1M cells resolution are shown in Fig. 3.4. The jet breaks up at around $x/D = 1$ for the case of 4 stochastic fields, and the location of jet break-up moves further downstream as the number of stochastic fields increases. For the case of 4 stochastic fields, the decay rate is faster in the regions of $(2 < x/D < 3.5)$ compared with other combinations of stochastic field numbers. The numerical results do not converge, and we have different profiles for all stochastic fields. This concludes that for the 1.1M cell case the number of stochastic fields is insufficient to have the converged solution.

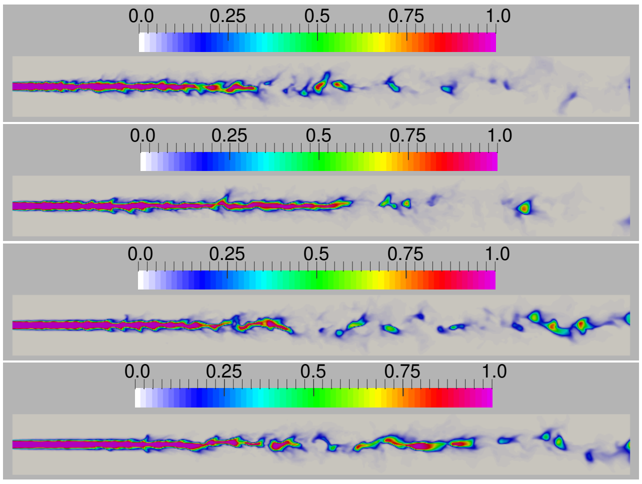

Fig. 3.3 Instantaneous volume fraction fields at the central plane of N-AS2 using the different number of stochastic fields. Top: 1.1M,4SF, Second: 1.1M,8SF, Third: 1.1M,16SF, Bottom: 1.1M,32SF.

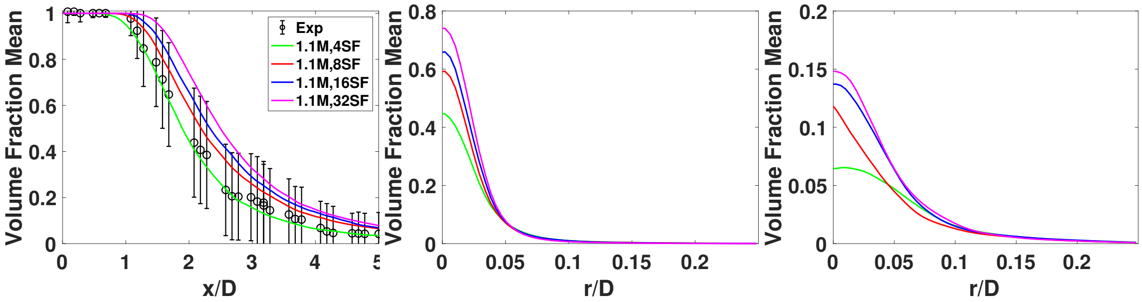

(a) Axial (b) $x/D = 2$ (c) $x/D = 4$

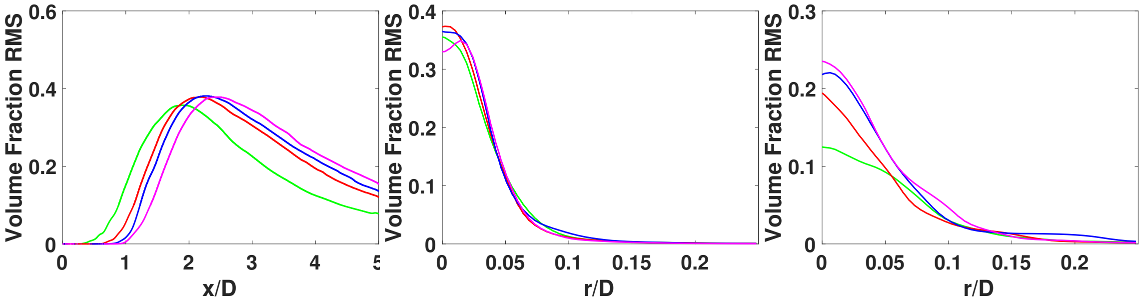

(d) Axial (e) $x/D = 2$ (f) $x/D = 4$

Fig. 3.4 Axial and radial profiles of mean (1st row) and rms (2nd row) of volume fraction for N-AS2 using different numbers of stochastic fields with 1.1 million LES cells. Radial profiles are shown at two axial stations. Experimental data [236] includes error bars.

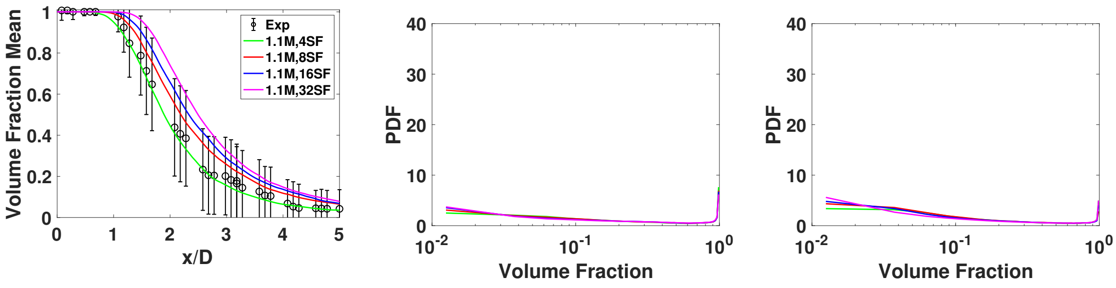

(a) Axial (b) $0 \leq x/D \leq 1$ (c) $1 \leq x/D \leq 2$

1

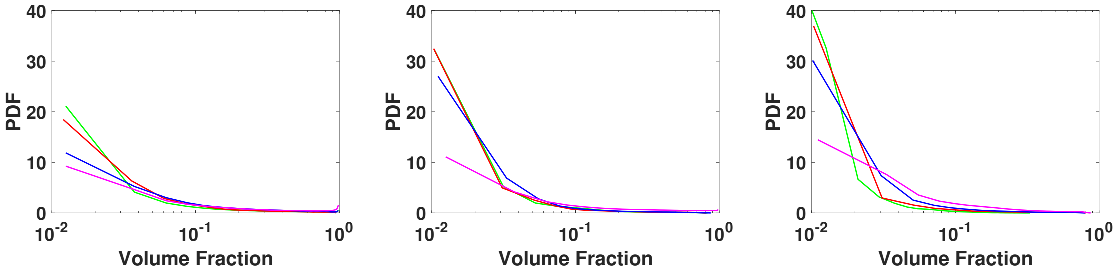

(d) $2 \leq x/D \leq 3$ (e) $3 \leq x/D \leq 4$ (f) $4 \leq x/D \leq 5$

Fig. 3.5 PDF calculations of volume fraction values for N-AS2 using the different number of stochastic fields in combination with axial profiles for mean volume fraction. Experimental data [236] includes error bars.

PDF of liquid volume fraction for 1.1M resolution case in combination with different stochastic fields is represented in Fig. 3.5. The calculations are made along the jet with imposing the condition on liquid volume fraction α as $0.01 \leq \alpha \leq 1$. In the near-field region $(x/D \leq 2)$ probability of liquid volume fraction for all combinations of stochastic fields is almost similar. Further downstream $(x/D \geq 2)$, these PDF measurements are sensitive to stochastic field numbers. Overall, numerical convergence observed here is consistent with the mean liquid volume fraction as shown in Fig. 3.4, and converged solution is not achieved for 1.1M LES cells in combination with increased stochastic fields up to 32 stochastic field numbers.

The axial and radial profiles for the mean and rms values of normalized surface density, $\bar{\Sigma}/\bar{\Sigma}_{min}$, are presented in Fig. 3.6. The results are consistent with the mean and rms values of volume fraction, and no evident convergence is found when the stochastic field numbers are increased gradually up to 32. In Fig. 3.6a, surface density increases very slowly from the nozzle exit as the surface wave evolves. From the jet break-up point, as determined in Fig. **??**, the surface density dramatically increases, and the peak value is located at the position where we have the highest rms value of volume fraction. Intermittency of the ligaments can be visualized in Fig. 3.3, which gradually grows downstream, leading to a smooth surface density reduction. In radial directions (see Figs. 3.6b and 3.6c), a peak value is observed that is supposed to be at the radius of the liquid jet. It decreases to the periphery with the same trend as the volume fraction profiles.

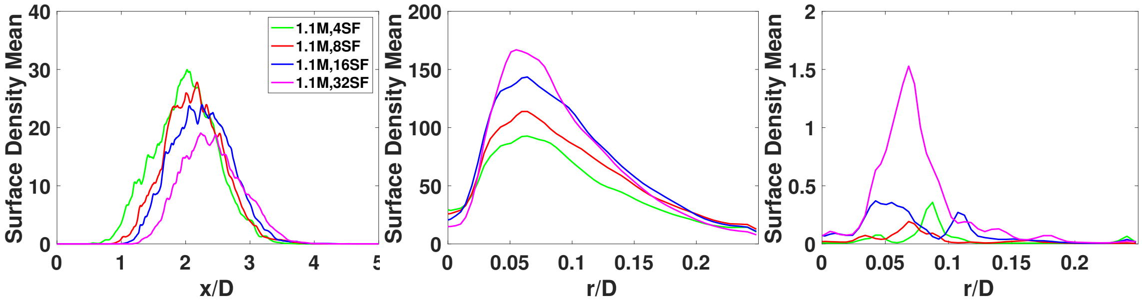

(a) Axial (b) $x/D = 2$ (c) $x/D = 4$

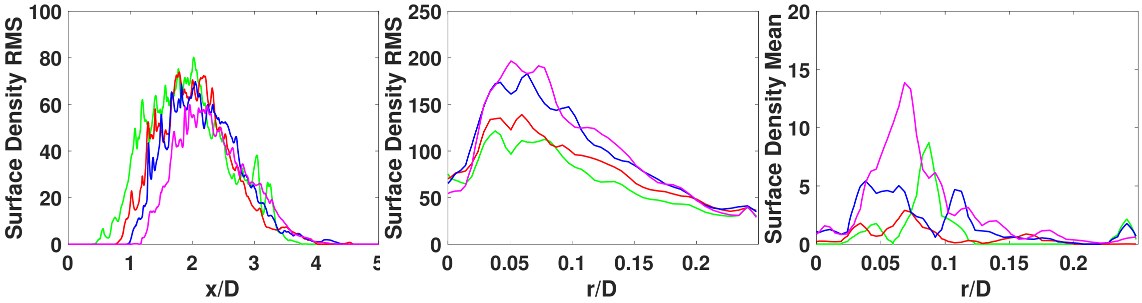

(d) Axial (e) $x/D = 2$ (f) $x/D = 4$

Fig. 3.6 Axial and radial profiles of mean (1st row) and rms (2nd row) of surface density for N-AS2 using different numbers of stochastic fields with 1.1 million LES cells. Radial profiles are shown at two axial stations.

PDF of liquid surface density for 1.1M resolution case in combination with different stochastic fields is represented in Fig. 3.7. The calculations are made along the jet with imposing the condition on liquid volume fraction α as $0.01 \leq \alpha \leq 1$. In the near-field region $(x/D \leq 3)$ probability of surface density has shown less sensitivity to the increase in stochastic fields. Further downstream $(x/D \geq 3)$, the PDF are more sensitive to stochastic field numbers. The numerical convergence observed here is consistent with the mean liquid volume fraction and mean liquid surface density as shown in Figs. 3.4 and 3.6.

The axial and radial profiles of mean and rms of the axial component of velocity, U_x, for 1.1M grid cells are presented in Fig. 3.8. In contradiction to the volume fraction and surface density results, the mean profiles of U_x present a mostly similar trend with the increase in the number of stochastic fields, and the results for the axial mean and rms of velocity profiles are pretty close to each other (see Figs. 3.8a and 3.8d). However, some visible divergence is evident in the radial profiles for both mean and rms values at $x/D = 2$.

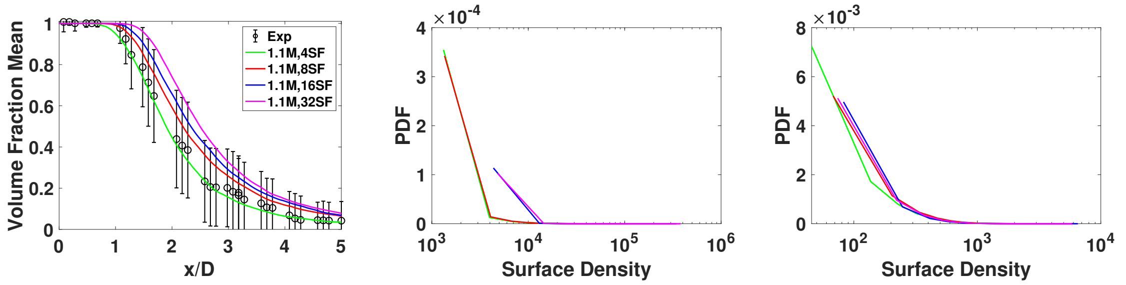

(a) Axial (b) $0 \leq x/D \leq 1$ (c) $1 \leq x/D \leq 2$

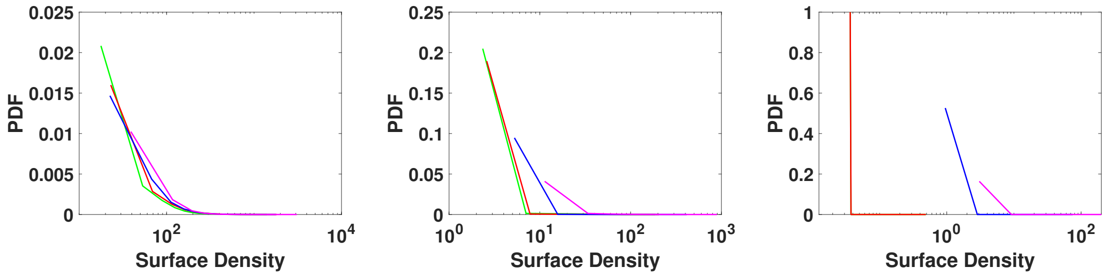

(d) $2 \leq x/D \leq 3$ (e) $3 \leq x/D \leq 4$ (f) $4 \leq x/D \leq 5$

Fig. 3.7 PDF calculations of surface density values for N-AS2 using the different number of stochastic fields in combination with axial profiles for mean volume fraction. Experimental data [236] includes error bars.

Overall, rigorous numerical convergence for 1.1M LES cells in the combination of increased stochastic fields is not achieved up to 32 stochastic field numbers. As the number of stochastic fields increases, the jet break-up location moves further downstream in the flow direction. The maximum value of normalized surface density for the case of 4 stochastic fields confirms the rapid jet break-up for less number of stochastic fields.

2.3M LES cells

Figure 3.9 shows instantaneous snapshots of the filtered volume fraction fields on 2.3M LES grids for case N-AS2 with the combination of 4,8,16 and 32 stochastic fields. Similar to 1.1M resolution cases (see Fig. 3.3), we can see the delay in jet break-up with the increase in the number of stochastic fields. However, the difference is comparatively small as we move from lesser to the higher value of stochastic field numbers and instantaneous liquid volume fractions fields for both 16 and 32 stochastic fields are quite similar. These instantaneous plots show that results are less sensitive to stochastic fields when compared with 1.1M LES grid cells. The mean and rms of volume fraction in the axial and radial directions for 2.3M cells resolution are shown in Fig. 3.10. The jet breaks up at around $x/D = 1$ for the case of 4 stochastic fields, and the location of jet break-up moves further downstream as the number of

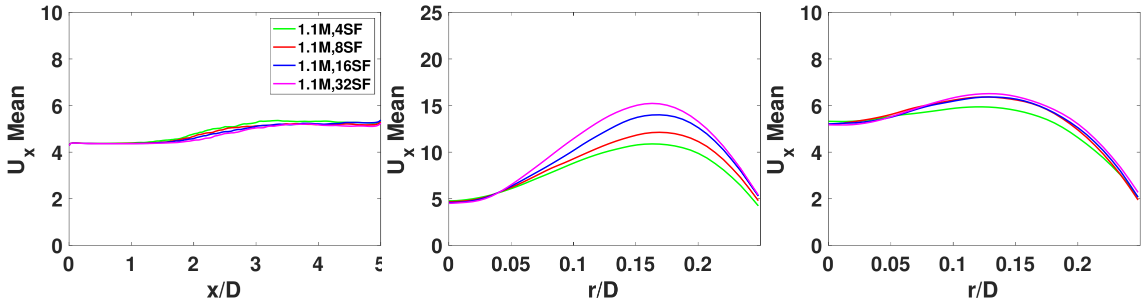

(a) Axial (b) $x/D = 2$ (c) $x/D = 4$

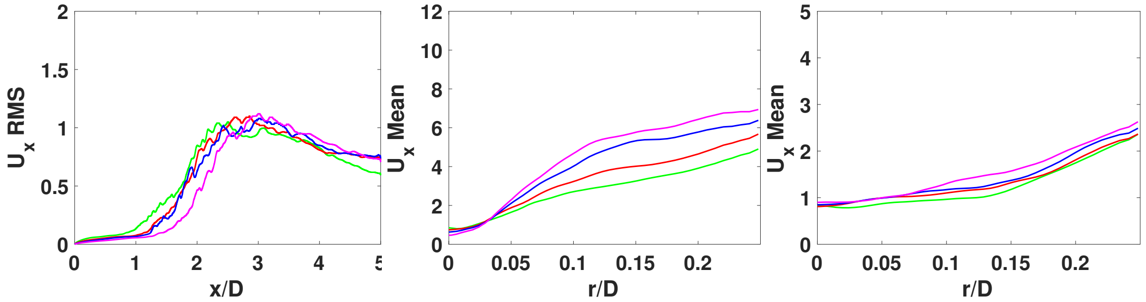

(d) Axial (e) $x/D = 2$ (f) $x/D = 4$

Fig. 3.8 Axial and radial profiles of mean (1st row) and rms (2nd row) of the axial component of velocity for N-AS2 using different number of stochastic fields with 1.1 million LES cells. Radial profiles are shown at two axial stations.

stochastic fields increases and the decay rate is faster for the case of 4 and 8 stochastic fields in the regions of ($2 < x/D < 3.5$) when compared with other combinations of stochastic field numbers. The numerical results seem to be converged as the mean liquid volume fraction values (see Fig. 3.10a) for both 16 and 32 stochastic fields are similar calculated along the jet centreline. This concludes that 16 stochastic fields are enough to have the converged solution for 2.3M cells resolution.

PDF of liquid volume fraction for 2.3M resolution case in combination with different stochastic fields is represented in Fig. 3.11. In the near-field region ($x/D \leq 2$) probability of liquid volume fraction for all combinations of stochastic fields is almost similar and does not show much difference when compared with 1.1M resolution. Further downstream ($x/D \geq 2$), the PDF measurement is sensitive to stochastic field numbers, but numbers for 16 and 32 stochastic fields are very similar, confirming the reach of stochastic field convergence. Overall, the numerical convergence observed here is consistent with the mean liquid volume fraction as shown in Fig. 3.10.

The axial and radial profiles for the mean and rms values of normalized surface density, $\bar{\Sigma}/\bar{\Sigma}_{min}$, for 2.3M resolution are presented in Fig. 3.12. The results are consistent with

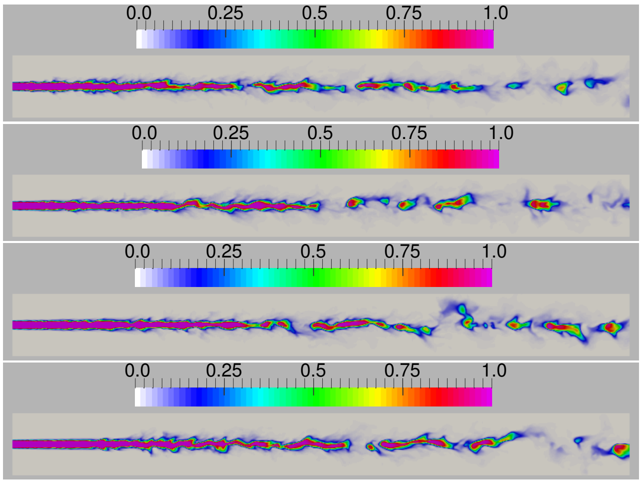

Fig. 3.9 Instantaneous volume fraction fields at the central plane of N-AS2 using the different number of stochastic fields. Top: 2.3M,4SF, Second: 2.3M,8SF, Third: 2.3M,16SF, Bottom: 2.3M,32SF.

the mean and rms values of volume fraction, and reasonable convergence is found when the stochastic field numbers are increased from 16 to 32. Consistent with the 1.1M LES cells, in Fig. 3.12a, surface density increases very slowly from the nozzle exit as the surface wave evolves. From the jet break-up point, as determined in Fig. 3.10a, the surface density dramatically increases, and the peak value is located at the position where we have the highest rms value of volume fraction. Intermittency of the ligaments can be visualized in Fig. 3.9, which gradually grows downstream, leading to a smooth reduction of surface density. In radial directions (see Figs. 3.12b and 3.12c), a peak value is observed that is supposed to be at the radius of the liquid jet. It decreases to the periphery with the same trend as the volume fraction profiles.

PDF of liquid surface density for 2.3M resolution case in combination with different stochastic fields is represented in Fig. 3.13. In the near-field region $(x/D \leq 3)$ probability of liquid surface density for combinations of 16 and 32 stochastic fields is almost similar, but further downstream $(x/D \geq 3)$, the PDF numbers are still sensitive to stochastic field numbers. However, the overall convergence behaviour of PDF for surface density is similar to what we have observed for the mean liquid surface density as shown in Fig. 3.12. The axial and radial profiles of mean and rms of the axial component of velocity, U_x, for 2.3M grid cells are presented in Fig. 3.14. Upon comparison with 1.1M resolution, we have found a different behaviour in the volume fraction and surface density results. However, the mean profiles of U_x present a mostly similar trend with the different number of stochastic fields, and the results for the axial mean and rms of velocity profiles are quite close to each other

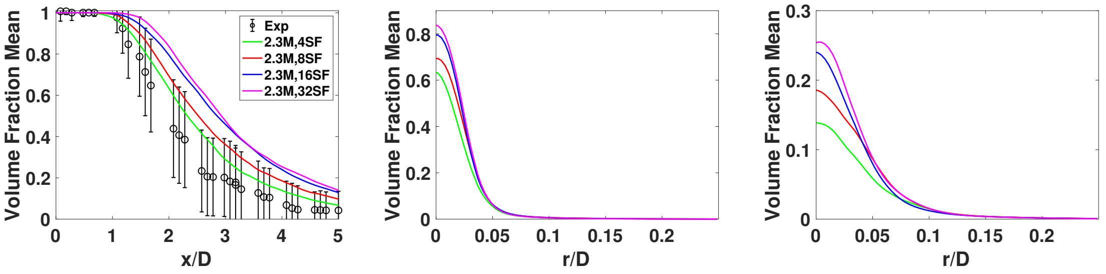

(a) Axial (b) $x/D = 2$ (c) $x/D = 4$

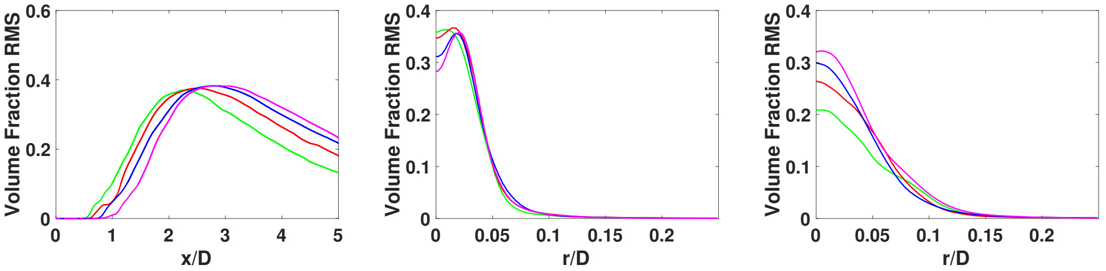

(d) Axial (e) $x/D = 2$ (f) $x/D = 4$

Fig. 3.10 Axial and radial profiles of mean (1st row) and rms (2nd row) of volume fraction for N-AS2 using different numbers of stochastic fields with 2.3 million LES cells. Radial profiles are shown at two axial stations. Experimental data [236] includes error bars.

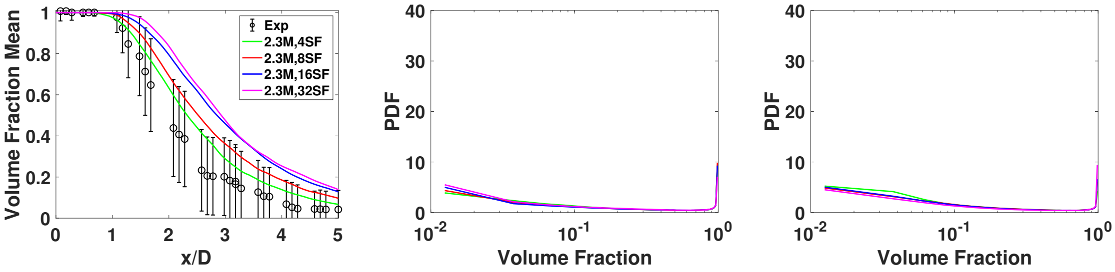

(a) Axial (b) $0 \leq x/D \leq 1$ (c) $1 \leq x/D \leq 2$

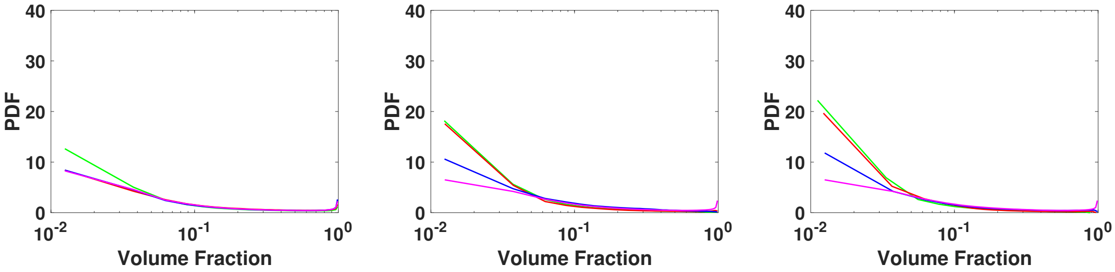

(d) $2 \leq x/D \leq 3$ (e) $3 \leq x/D \leq 4$ (f) $4 \leq x/D \leq 5$

Fig. 3.11 PDF calculations of volume fraction values for N-AS2 using the different number of stochastic fields in combination with axial profiles for mean volume fraction. Experimental data [236] includes error bars.

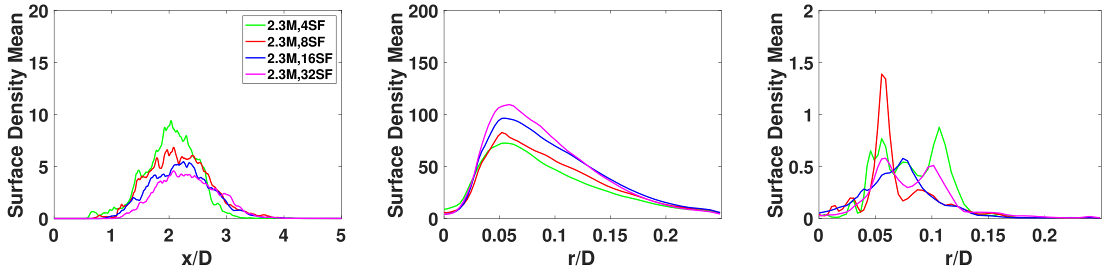

(a) Axial (b) $x/D = 2$ (c) $x/D = 4$

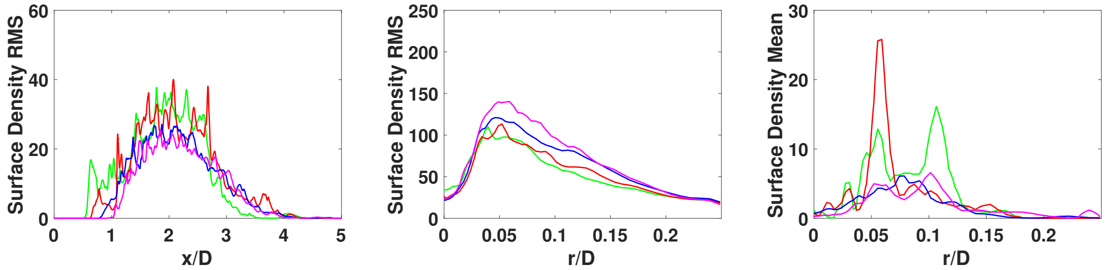

(d) Axial (e) $x/D = 2$ (f) $x/D = 4$

Fig. 3.12 Axial and radial profiles of mean (1st row) and rms (2nd row) of surface density for N-AS2 using different numbers of stochastic fields with 2.3 million LES cells. Radial profiles are shown at two axial stations.

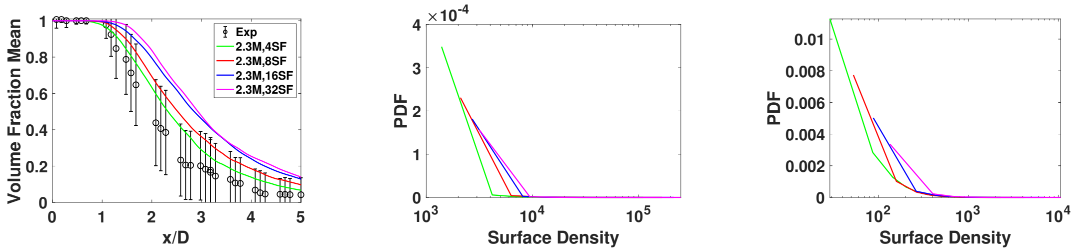

(a) Axial (b) $0 \leq x/D \leq 1$ (c) $1 \leq x/D \leq 2$

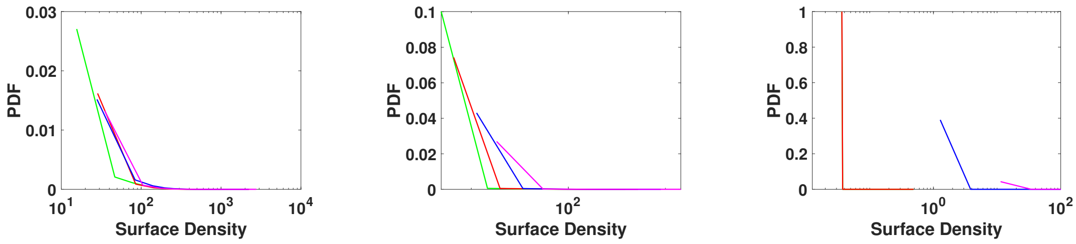

(d) $2 \leq x/D \leq 3$ (e) $3 \leq x/D \leq 4$ (f) $4 \leq x/D \leq 5$

Fig. 3.13 PDF calculations of surface density values for N-AS2 using the different number of stochastic fields in combination with axial profiles for mean volume fraction. Experimental data [236] includes error bars.

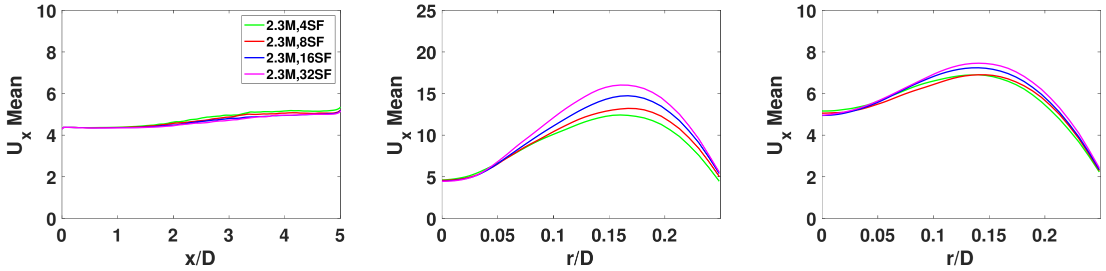

(a) Axial (b) $x/D = 2$ (c) $x/D = 4$

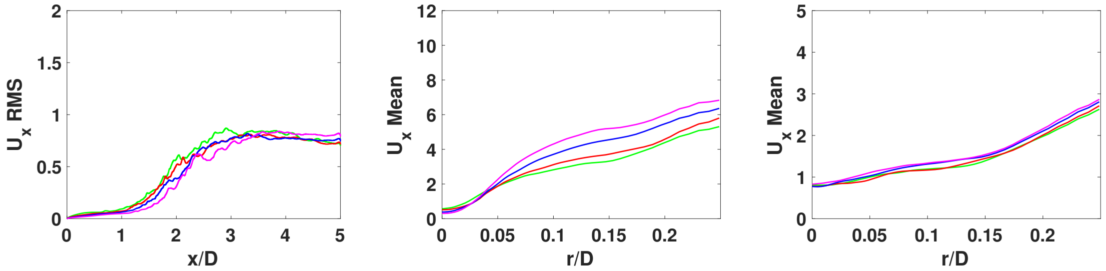

(d) Axial (e) $x/D = 2$ (f) $x/D = 4$

Fig. 3.14 Axial and radial profiles of mean (1st row) and rms (2nd row) of the axial component of the velocity for N-AS2 using different number of stochastic fields with 2.3 million LES cells. Radial profiles are shown at two axial stations.

(see Figs. 3.14a and 3.14d). A similar divergence is observed in the radial profiles for both mean and rms values at $x/D = 2$ as noticed for 1.1M LES grid numbers.

Overall, in the combination of increased stochastic fields, reasonable numerical convergence for 2.3M LES cells is achieved up to 32 stochastic field numbers. As the number of stochastic fields increases, the jet break-up location moves further downstream in the flow direction. The maximum value of normalized surface density for the case of 4 stochastic fields confirms the rapid jet break-up for less number of stochastic fields.

4.5M LES cells

Figure 3.15 shows instantaneous snapshots of the filtered volume fraction fields on 4.5M LES grids for case N-AS2 with the combination of 4,8,16 and 32 stochastic fields. Opposite to 1.1M and 2.3M resolution cases (see Figs. 3.3 and 3.9), we can see a similar jet penetration for all the stochastic field combinations. However, we have found a similar trend in the decay rate on increasing the number of stochastic fields, and a rapid decay rate is observed when four stochastic fields are used. The difference is minimal as we move from lesser to a higher value of stochastic field numbers, and instantaneous liquid volume fractions fields for 8, 16 and 32 stochastic field numbers are quite similar. These instantaneous plots show that results

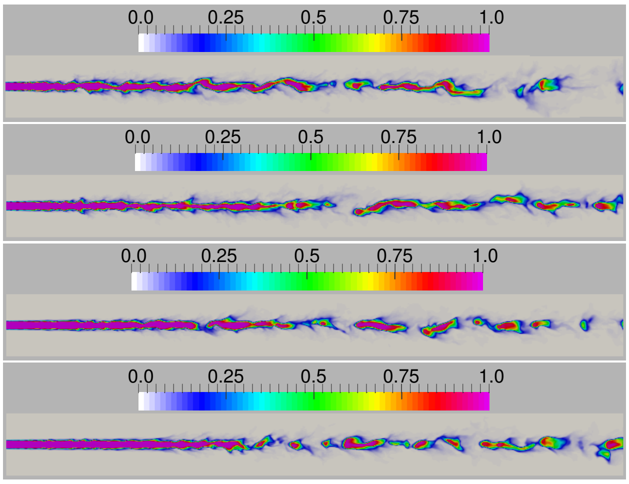

Fig. 3.15 Instantaneous volume fraction fields at the central plane of N-AS2 using the different number of stochastic fields. Top: 4.5M,4SF, Second: 4.5M,8SF, Third: 4.5M,16SF, Bottom: 4.5M,32SF.

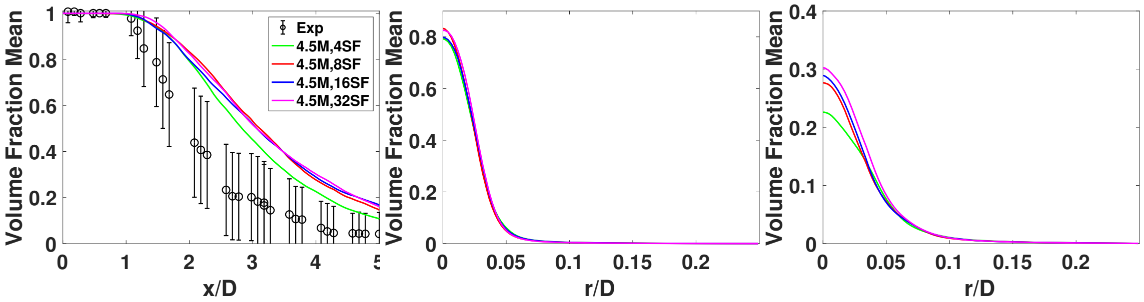

(a) Axial (b) $x/D = 2$ (c) $x/D = 4$

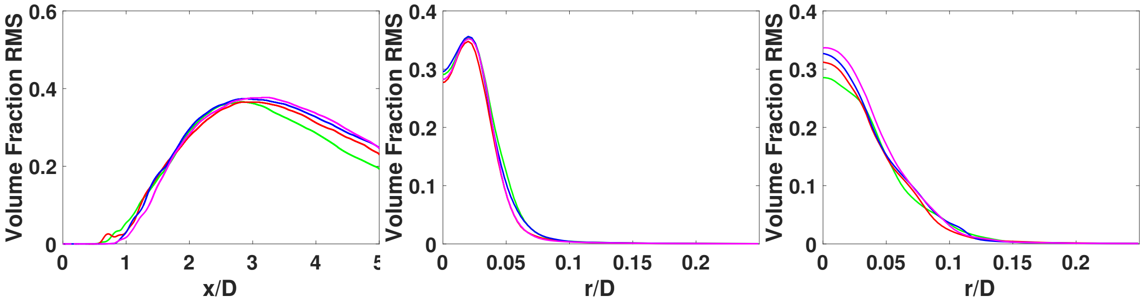

(d) Axial (e) $x/D = 2$ (f) $x/D = 4$

Fig. 3.16 Axial and radial profiles of mean (1st row) and rms (2nd row) of volume fraction for N-AS2 using different numbers of stochastic fields with 4.5 million LES cells. Radial profiles are shown at two axial stations. Experimental data [236] includes error bars.

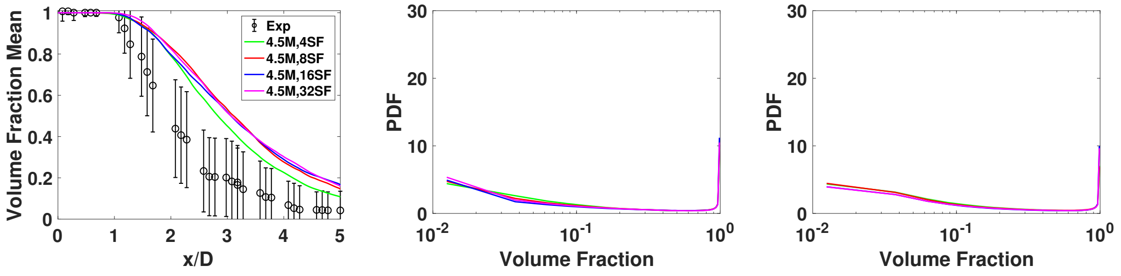

(a) Axial (b) $0 \leq x/D \leq 1$ (c) $1 \leq x/D \leq 2$

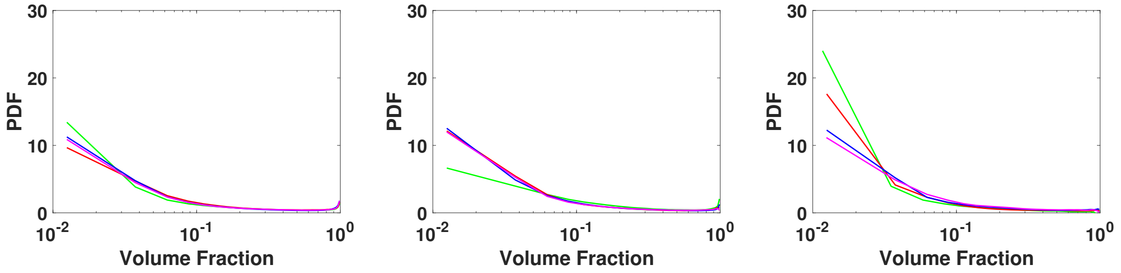

(d) $2 \leq x/D \leq 3$ (e) $3 \leq x/D \leq 4$ (f) $4 \leq x/D \leq 5$

Fig. 3.17 PDF calculations of volume fraction values for N-AS2 using the different number of stochastic fields in combination with axial profiles for mean volume fraction. Experimental data [236] includes error bars.

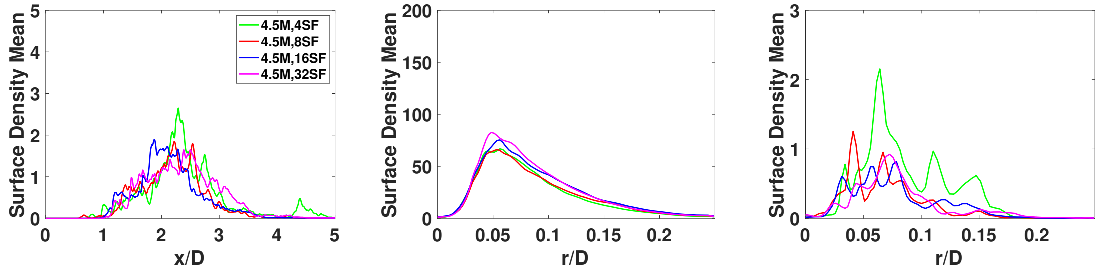

(a) Axial (b) $x/D = 2$ (c) $x/D = 4$

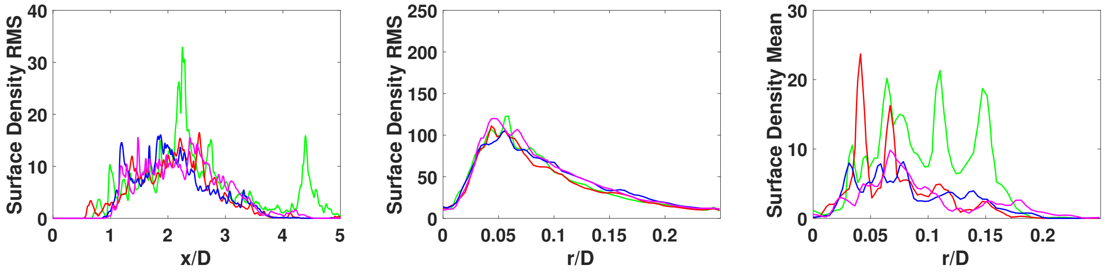

(d) Axial (e) $x/D = 2$ (f) $x/D = 4$

Fig. 3.18 Axial and radial profiles of mean (1st row) and rms (2nd row) of surface density for N-AS2 using different numbers of stochastic fields with 4.5 million LES cells. Radial profiles are shown at two axial stations.

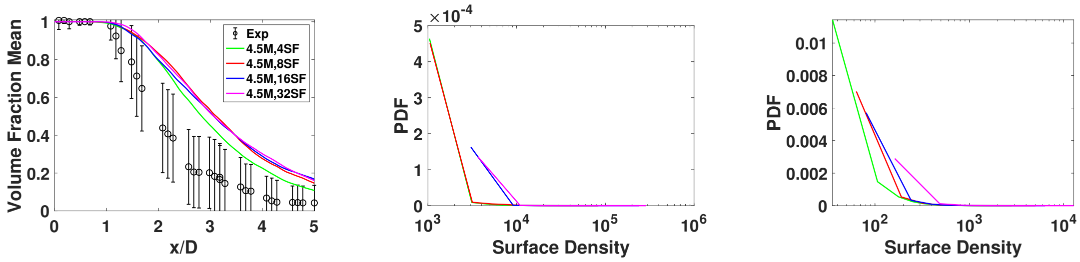

(a) Axial (b) $0 \leq x/D \leq 1$ (c) $1 \leq x/D \leq 2$

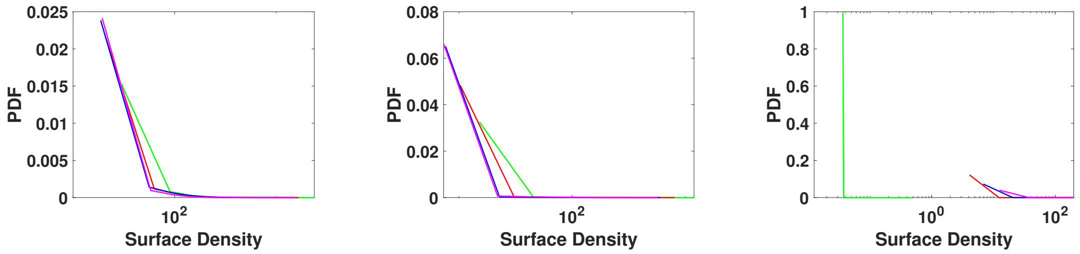

(d) $2 \leq x/D \leq 3$ (e) $3 \leq x/D \leq 4$ (f) $4 \leq x/D \leq 5$

Fig. 3.19 PDF calculations of surface density values for N-AS2 using the different number of stochastic fields in combination with axial profiles for mean volume fraction. Experimental data [236] includes error bars.

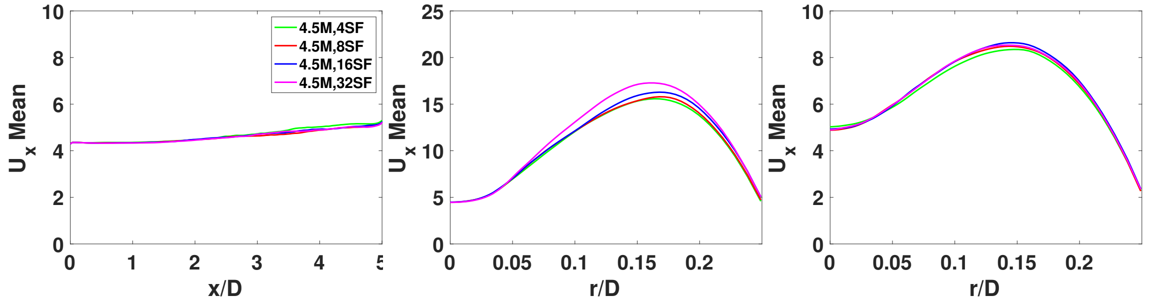

(a) Axial (b) $x/D = 2$ (c) $x/D = 4$

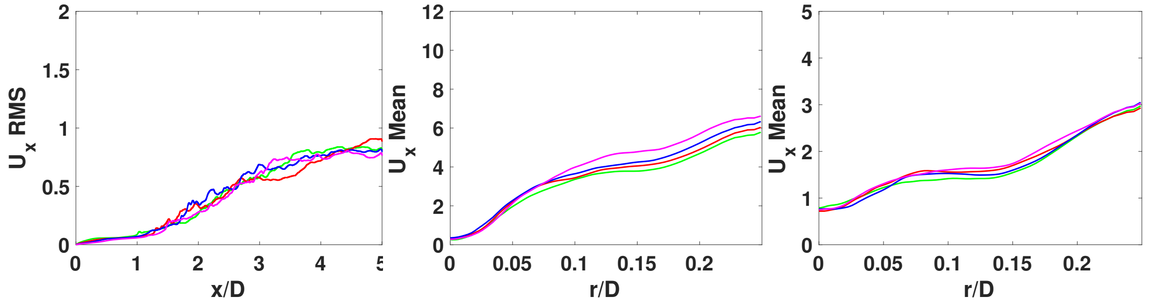

(d) Axial (e) $x/D = 2$ (f) $x/D = 4$

Fig. 3.20 Axial and radial profiles of mean (1st row) and rms (2nd row) of the axial component of velocity for N-AS2 using different number of stochastic fields with 4.5 million LES cells. Radial profiles are shown at two axial stations.

are much less sensitive to stochastic fields when compared with 1.1M and 2.3M LES grid cells.

The mean and rms of volume fraction in the axial and radial directions for 4.5M cells resolution are shown in Fig. 3.16. The jet breaks up at around $x/D = 1$ for all the stochastic field combinations, and the decay rate is faster for the case of 4 stochastic fields in the regions of $(2 < x/D < 3.5)$ when compared with other combinations of stochastic field numbers. The numerical results have shown an excellent converged behaviour as the mean liquid volume fraction values (see Fig. 3.16a for 8, 16 and 32 stochastic fields are almost overlapping each other. This concludes that eight stochastic fields are enough to have the converged solution for 4.5M cells resolution.

PDF of liquid volume fraction for 4.5M resolution case in combination with different stochastic fields is represented in Fig. 3.17. In the near-field region $(x/D \leq 2)$ probability of liquid volume fraction for all combinations of stochastic fields is very similar and does represent closer values when compared with 1.1M and 2.3M resolutions. Further downstream $(x/D \geq 2)$, the PDF numbers are sensitive to stochastic field numbers, and PDF values of liquid volume fraction and surface density for 8, 16 and 32 stochastic fields are very similar, confirming the reach of stochastic field convergence. Overall, the numerical convergence observed here is consistent with the mean liquid volume fraction as shown in Fig. 3.16.

The axial and radial profiles for the mean and rms values of normalized surface density, $\bar{\Sigma}/\bar{\Sigma}_{min}$, for 4.5M resolution are presented in Fig. 3.18. The results are consistent with the mean and rms values of volume fraction, and the same convergence behaviour is found when the stochastic field numbers are increased from 8 to 32. Consistent with the 1.1M and 2.3M LES cells, in Fig. 3.20a, surface density increases very slowly from the nozzle exit as the surface wave evolves. From the jet break-up point, as determined in Fig. 3.16a, the surface density dramatically increases, and the peak value is located at the position where we have the highest rms value of volume fraction. Intermittency of the ligaments can be visualized in Fig. 3.15, which gradually grows downstream, leading to a smooth reduction of surface density. In radial directions (see Figs. 3.18b and 3.18c), a peak value is observed that is supposed to be at the radius of the liquid jet which is similar as we have found for 1.1M and 2.3M LES cells (see Figs. 3.6b , 3.6c,3.12b and 3.12c). It decreases to the periphery with the same trend as the volume fraction profiles.

PDF of surface density for 4.5M resolution case in combination with different stochastic fields is represented in Fig. 3.19. Here, PDF values of surface density for all combinations of stochastic fields except for the case of 4 stochastic fields are very similar and represent closer values compared with 1.1M and 2.3M resolutions. However, this convergence behaviour is more evident for the liquid fraction PDF values when compared with surface density PDF data. Overall, the numerical convergence observed here is consistent with the mean liquid surface density as shown in Fig. 3.18.

The axial and radial profiles of mean and rms of the axial component of velocity, U_x, for 4.5M grid cells are presented in Fig. 3.20. As presented for 1.1M and 2.3M resolutions, we found a contradiction in the volume fraction and surface density results. The mean profiles of U_x present a similar trend with the different number of stochastic fields, and the results for the axial mean and axial rms of velocity profiles are quite close to each other (see Figs. 3.20a and 3.20d). A similar divergence is also observed in the radial profiles for both mean and rms values at $x/D = 2$ as found for 1.1M and 2.3M grid numbers.

Overall, excellent convergence behaviour can be observed for 4.5M LES cells when tested against a different number of stochastic fields. Opposite to 1.1M and 2.3M resolution cases, the jet break-up location seems less affected by the increase in stochastic field numbers.

3.8.2 Grid sensitity

The mean volume fraction in the axial and radial directions for 1.1M, 2.3M and 4.5M LES cells resolution of four combinations of stochastic fields is shown in Fig. 3.21. The jet breaks up at around $x/D = 1$ for the case of 4 stochastic fields, and the location of jet break-up moves further downstream as the number of stochastic fields increases. For the case of 4 and 8 stochastic fields, the decay rate is faster in the regions of $(2 < x/D < 3.5)$ for 1.1M and 2.3M cells when compared with 4.5M cells. However, a similar jet decay rate is observed for 2.3M and 4.5M cells when 16 or 32 stochastic fields are used. This is also evident in Fig. 3.21 that in LES-PDF simulation solution is dependent on the combination of LES grid size and the number of stochastic fields within each cell. For the case of 4 or 8 stochastic fields in each cell, the solution is more sensitive to the mesh resolution compared with 16 or 32 stochastic fields. The measurements in the radial directions confirm that LES-PDF is more sensitive to grid resolution in the far-field region, where the sub-grid scale effects are more dominant.

3.9 Summary

Convergence behaviour of the stochastic field numbers is analyzed for three different mesh sizes 1.1M, 2.3M and 4.5M. This has been measured in terms of different parameters like liquid jet penetration and decay rate, mean and rms of liquid volume fraction, mean and rms of surface density, mean and rm of liquid velocity, PDF calculations of volume fractions and surface density. Rigorous numerical convergence for 1.1M LES cells in the combination

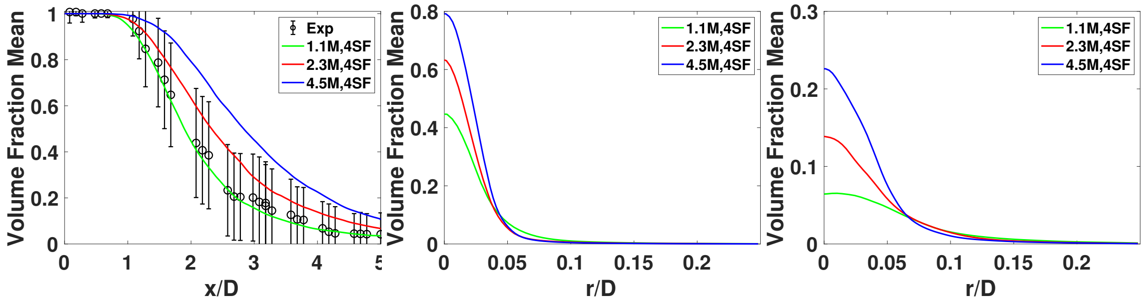

(a) Axial (b) $x/D = 2$ (c) $x/D = 4$

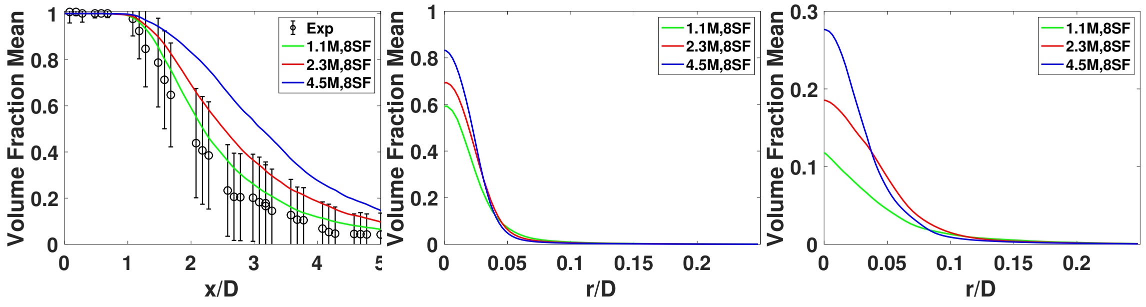

(d) Axial (e) $x/D = 2$ (f) $x/D = 4$

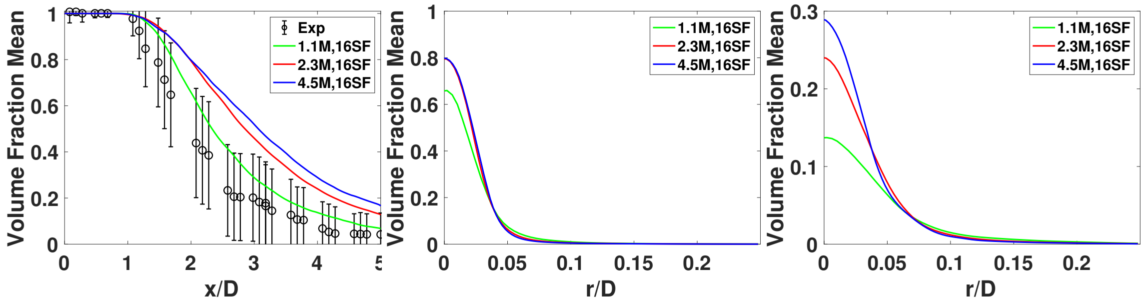

(g) Axial (h) $x/D = 2$ (i) $x/D = 4$

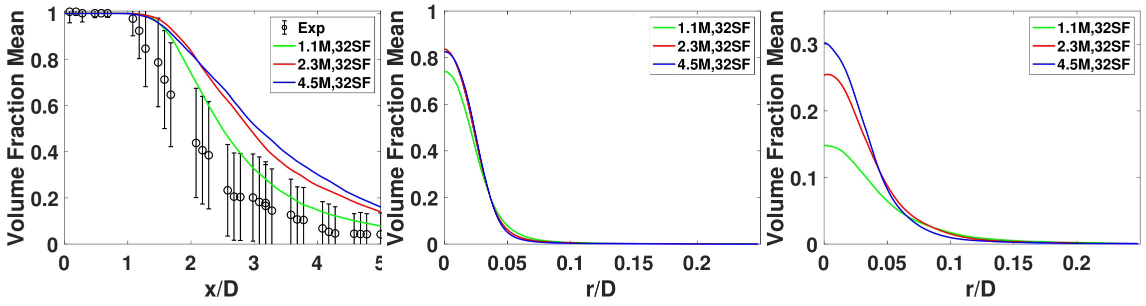

(j) Axial (k) $x/D = 2$ (l) $x/D = 4$

Fig. 3.21 Axial and radial profiles of mean volume fraction for N-AS2 using different numbers of stochastic fields and LES cells. Radial profiles are shown at two axial stations. Experimental data [236] includes error bars.

of increased stochastic fields is not achieved up to 32 stochastic field numbers. As the number of stochastic fields increases, the jet break-up location shifts further downstream. The maximum value of normalized surface density for the case of 4 stochastic fields confirms the rapid jet break-up for less number of stochastic fields. In the near-field region probability of liquid volume fraction for all stochastic fields is similar, but in downstream locations, the PDF values are sensitive to stochastic field numbers. Similar behaviour is observed in the surface density PDF data, where sensitivity to stochastic field numbers is more evident in the downstream regions. Overall, the numerical convergence observed for the PDF measurements is consistent with the mean liquid volume fraction and mean liquid surface density, and no obvious converged solution is obtained for 1.1M LES cells up to 32 stochastic field numbers.

However, reasonable numerical convergence is observed for 2.3M LES cells, and measured values of mean liquid volume fraction and normalized mean surface density for the 16 and 32 stochastic fields are very similar. Jet break-up location is also sensitive to the number of stochastic fields and moves in the downstream direction with the increased stochastic field numbers. PDF of liquid volume fraction shows a similar convergence trend as observed for mean liquid volume fraction. However, the PDF of surface density for 2.3M LES cells does not give a reasonable indication of stochastic field convergence. This might be because instantaneous values of surface density change rapidly along the flow direction, and convergence is not as evident as shown for the mean liquid volume fraction values.

Overall, very good convergence behaviour can be observed for 4.5M LES cells when measured for the different number of stochastic fields. Here, unlike 1.1M and 2.3M resolution cases, the jet break-up location is less sensitive to the increase in stochastic field numbers. Here, the maximum normalized surface density value is also measured for the least number of stochastic fields. That also confirms the rapid jet break-up behaviour for this case, as observed in the instantaneous liquid volume fraction fields. PDF of liquid volume fraction and surface density for 4.5M resolution case gives a similar convergence representation upon comparison with mean liquid volume fraction and mean surface density. However, this convergence behaviour is more evident for the liquid fraction PDF values when compared with surface density PDF data. Furthermore, this stochastic field convergence study combined with different mesh resolutions confirms that more stochastic fields are required to achieve a converged solution when a coarser resolution is used. However, convergence can be achieved with fewer stochastic fields for finer mesh resolution. This leads to the conclusion that the stochastic fields convergence behaviour depends on the mesh size.

Grid sensitivity is still an issue with the VoF based LES approaches, and the solution is dependent on the LES filter size. The numerical findings of the stochastic fields LES-PDF solution also confirm its grid-dependent behaviour. Using a higher number of stochastic fields in each LES cell has shown some improvements, but the simulation results are still sensitive to LES cell sizes.

Chapter 4

Large Eddy Simulation Solutions for Volume of Fluid

The first half of this Chapter describes the numerical implementation in OpenFOAM along with the discretization schemes and relevant solution solvers. The general VoF formulation is presented in Section 2.3. Here, three different LES solutions for the VoF method are presented, which differ in the treatment of unresolved liquid-air interface. Filtering produces sub-filter fluctuations, which must be modelled. If the filter is equal to the grid size, they are usually referred to as sub-grid fluctuations. In general numerical solutions of the filtered VoF equations, filter width is equal to the mesh size and the interface sharpens as the grid is refined, leading to variations in interface topology and flow dynamics. For practically affordable computations, the grid resolved interfacial properties represent a numerically dependent average of the sub-grid fields. When the flow is turbulent, there are additional unresolved fluctuations due to the random turbulent motions which exist within the interior of each fluid and at the interface. To be practically useful, VoF based LES should numerically converge as the grid is refined. In the previous Chapter numerical convergence of the stochastic fields implementation of the VoF/LES model was examined and it was found that numerical convergence with the refinement of the grid remained elusive, although convergence with the number of stochastic fields was achieved. In the present Chapter, the performance and numerical convergence of three alternative VoF/LES models are examined. Two are conventional models [34, 54, 47, 184, 130, 12] and the third, called Explicit Volume Diffusion (EVD), was recently presented by Wang et al. [270] and was specifically designed to overcome the shortcomings of other LES based methods. As this EVD approach is new, and for better understanding, a complete description of its formulation is presented here in this Chapter following the original work of Wang, Cleary and Masri [270].

4.1 Discretization schemes and system solutions

The solution of the model partial differential equations depends on the discretization process to have the maximum use of the available computational resources. There are many methods available for this purpose, but most popular choices for two-phase flows are finite difference [127], finite element [97, 186, 233] and finite volume [105, 107] methods. Considering each method's specific advantages and disadvantages, mathematical formulations for two-phase flows, possibilities for easy solver writing, transparent parallelization and availability of free access to basic code requirements, the cell-centered finite volume method is used [117]. The same numerical schemes are used for all solvers, and these have been previously validated for the interFoam solver [58]. The unsteady time derivative term is discretized using the forward Euler scheme. Second-order central difference schemes are used for the discretized convection and diffusion terms. The convection of volume fraction is an exception as it is solved using a multidimensional universal limiter for explicit solution (MULES) algorithm [163] which guarantees boundedness of volume fraction fields and numerical stability for immiscible interfaces with large liquid/gas density ratios. The computational time step for integration is determined following the Courant-Friedrich-Levy (CFL) condition, written as

$$CFL = \frac{k^{1/2}\Delta t}{\Delta x} < 1, \tag{4.1}$$

where Δt is computational time step, Δx is grid size and k is turbulent kinetic energy.

4.1.1 Multidimensional universal limiter for explicit solution (MULES)

Implementation of flux-corrected transport (FCT) theory of [28] in OpenFOAM is termed as MULES, which is based on Zalesak's limiter concept [281] but the determination process is rather iterative. The improvements made by Zalesak [281] to the original work of Boris and Book [28] ensure the solution boundedness of a hyperbolic problem and are considered the most trusted multidimensional high-resolution scheme. The Courant number Co needs to have a limitation depending on the choice of algorithm. For explicit MULES algorithm, an upper limit of $Co \approx 0.25$ is suitable in the region of the interfacial boundaries, and for semi-implicit MULES algorithm, it is specified by the MULESCorr keyword in the fvSolution file. The algorithm works in a way that each cell has a net flux, and maxima and minima calculations depend on the in-flow and the out-flow values. For the satisfaction of the boundedness requirement, MULES calculates the limited flux face by face via calculation of the weighted average of two fluxes for α [199]:

i) The flux computed with a first-order upwind scheme for the advection equation only, which has bounded values but is diffusive.

ii) The sum of the fluxes computed with the high-order scheme for both advection equation and the re-initialization requirements, and the net flux solution is higher-order accurate but not systematically bounded.

However, this weighted value differs for each face, which leads to the non-linear calculations of the FCT of limited flux. Use of the limiter factor concept and corrected flux approach [163, 199] is helpful to overcome this non-linearity problem. The calculation of the limiter factor is carried out iteratively to satisfy the boundedness of the solution, and the starting value is calculated based on Weller's algorithm [272].

Firstly, the calculation of correction fluxes for a particular cell is split into the sum of all out-flow and the sum of all in-flow corrected fluxes. Then, an average limiter factor is defined individually for all faces with in-flow and out-flow correction fluxes. The algorithm is designed in a way that the limiter factor for a particular face is selected based on a minimum of three values [199]:

a) The relevant average limiter factor in one of the adjacent cells for the out-flow correction flux if exiting.

b) The relevant average limiter factor in one of the adjacent cells for the in-flow correction flux if entering.

c) The limiter factor at the previous iteration.

The total number of iterations for the final limiter factor corresponding to each face of the mesh is defined by the user.

4.1.2 Pressure-velocity coupling

The discretization of the Navier-Stokes transport equations is based on the cell-centered finite volume approach. Pressure velocity coupling solution is obtained by either the pressure-implicit split operator (PISO), the semi-implicit method for pressure-linked equations (SIMPLE), or a combination of both, termed as PIMPLE algorithm. Most multi-phase applications use the PIMPLE solution for this purpose. The PIMPLE algorithm consists of the following steps:

i) Generation of a momentum matrix from the existing velocity fields.

ii) Developing a pressure matrix using the momentum matrix.

iii) Pressure calculation.

iv) Correction of the velocity fields with the new pressure values.

The transport equations are solved individually to have the converged solutions for pressure and velocity in a loop. The pressure is discretized at cell centres, and the velocities are calculated at cell faces. Initially, for the first time step, the flux is calculated from the velocity fields and then all the rest of the calculations are based on pressure-velocity loop calculations in the previous time step, which confirms the conservation of flux in the form of the continuity equation. The number of times the algorithm solves the pressure equation and the momentum corrector in each time step is adjusted externally in the fvSolution dictionary file depending upon the solution requirements. In this study PIMPLE algorithm is followed, the pressure equation is solved twice during each momentum correction operation, and this momentum correction takes place twice in each time step.

4.1.3 Solution solvers and tolerances

The discretization of the general advection and diffusion equations usually results in non-symmetric linear systems. However, in the case of the pressure equation, the discretization process results in symmetric systems. The symmetry of the matrix depends on the terms of the equation being solved. Time derivatives and Laplacian terms form coefficients of a symmetric matrix, whereas an advective derivative results in the asymmetry of the solution matrix. The solution of these systems is achieved by the use of iterative linear equation solvers for both symmetric and non-symmetric matrices [4], which include the pre-conditioned conjugate gradient (PCG), the diagonal incomplete-Cholesky (DIC) and diagonal incomplete-Cholesky with Gauss-Seidel (DICGaussSeidel) for the symmetric cases and the pre-conditioned bi-conjugate gradient (PBiCG), the Gauss-Seidel and the geometric-algebraic multi-grid (GAMG) for non-symmetric problems. Here, we have used a PCG solver pre-conditioned by DIC for volume fraction, a GAMG solver with smoother GaussSeidel for pressure calculations, and a PBiCGStab solver pre-conditioned by DILU for surface density and velocity fields.

Furthermore, these solution matrices are sparse, mostly including coefficients of 0 and have segregated, decoupled, finite volume numerics. As a result, the behaviour of these solvers is rather iterative, and the equation residuals are purposely reduced over the successive solutions. These residuals directly measure the solution accuracy, and the smaller values lead to a more accurate solution. These residuals are evaluated by substituting the existing solution into the relevant equation and calculating the difference in magnitudes between both sides of the equation. Normalized values are used to ensure that the answers are independent of the scale of the problem under consideration. The initial calculation of these residuals is made from the existing field values and then re-evaluated after each iteration. The solution stops if any of the following conditions happen:

a) The residual falls below the assigned tolerance value.

b) The ratio of current to initial residuals falls below the specified relative tolerance value.

c) The number of iterations exceeds the assigned maximum number.

To minimize the numerical diffusion, especially in the interfacial regions, we have selected a low value of tolerance, 10^-9, and zero relative tolerance for all field variables. The number of iterations is assigned sufficiently large to avoid the solution termination before the convergence is reached.

4.2 Conventional solutions for VoF approach

A conceptually simple and commonly adopted treatment for turbulent VoF simulations [34, 54, 47, 184, 130] is to spatially filter Eqs. (2.1), (2.2) and (2.20) and close the combined interfacial and turbulent sub-grid fluctuations through conventional turbulent viscosity models developed originally for turbulent single-phase flows. However, there is a fundamental difference between single-phase and two-phase turbulent flows, with the latter having sharp interfaces with a length scale much smaller than the well-known turbulent length scales in single-phase flows. Due to the immiscibility between the two phases, the Schmidt number for the liquid volume fraction is effectively infinity, and the Batchelor length scale approaches zero [37]. The conventional filtered VoF solution smooths the interface over grid cells through numerical diffusion and this diffusion is amplified for larger grid scales to create continuous fields [141] on which turbulence filtering is applied. Filtering is usually defined as the convolution of an arbitrary function $\Theta(x,t)$ in combination with a spatial filter function $G(x-x';\Delta(x))$. In LES, a spatial filtering operation with a width of Δ is applied to governing equations, separating into two groups based on scales larger than the filter size and smaller than the filter size. This results in the removal of all finer fluctuations in such a way that the resulting governing equations only describe the space-averaged fields. The filtering operation over a domain Ω is defined as

$$\bar{\Theta}(x) = \int_{\Omega} G(x-x';\Delta(x))\Theta(x',t)dx'. \tag{4.2}$$

Here, a basic top-hat filter [267] is used and the filter size is set as the cube root of the grid volume,

$$\Delta = \sqrt[3]{\Delta_x \Delta_y \Delta_z}, \tag{4.3}$$

where the subscripts x,y,z represent the length of the grid cell in each direction of Cartesian space. Linking the filter to the grid introduces numerical dependence into the modelling but, with a few exceptions [53, 222], this is common in LES due to its numerical practicality. The top-hat filter is the same as the grid filter, but the filter cuts off the values of the function larger than half of the filter width, defined as

$$G(x-x';\Delta)=\begin{cases}\Delta^{1/3} & \text{if } |x-x'|<\frac{\Delta}{2}\\ 0 & otherwise.\end{cases} \tag{4.4}$$

4.2.1 Turbulent filtered VoF model (TFVoF)

After simplifying Eqs. (2.1), (2.2) and (2.20) for incompressible flows in which the single fluid density is a linear combination of constant liquid and gas densities [107, 259], and then spatially filtering them over Δ, the TFVoF transport equations become

$$\frac{\partial \bar{u}_i}{\partial x_i}=0, \tag{4.5}$$

$$\frac{\partial \bar{\rho}\bar{u}_i}{\partial t}+\frac{\partial \bar{\rho}\bar{u}_i\bar{u}_j}{\partial x_i}=-\frac{\partial \bar{p}}{\partial x_i}+\frac{\partial \bar{\tau}_{ij}}{\partial x_i}+\bar{F}_{s,i}+\bar{\rho}g_i-\frac{\partial \tau_{ij}^{tf}}{\partial x_i}+f_{\rho,i}^{tf}+f_{\mu,i}^{tf}, \tag{4.6}$$

$$\frac{\partial \bar{\alpha}}{\partial t}+\frac{\partial \bar{u}_i\bar{\alpha}}{\partial x_i}=-\frac{\partial J_{\alpha,i}^{tf}}{\partial x_i}. \tag{4.7}$$

Here, the overbar, $\bar{\cdot}$, denotes conventional Reynolds filtering (i.e. not mass weighted). The first, second and fourth terms on the right side of Eq. (4.6) are in closed form with the resolved viscous stress expressed as

$$\bar{\tau}_{ij}=\bar{\mu}\left[2\bar{S}_{ij}-\frac{2}{3}\frac{\partial \bar{u}_k}{\partial x_k}\delta_{ij}\right]. \tag{4.8}$$

Closure models are required for the remaining terms in Eq. (4.6) along with the term on the right hand side of Eq. (4.7). The filtered surface tension force is decomposed into resolved and sub-grid parts as

$$\bar{F}_{s,i}=\sigma\bar{\kappa}\bar{n}_i|\nabla\bar{\alpha}|+F_{s,i}^{tf}, \tag{4.9}$$

where the superscript ^{tf} denotes the sub-grid component due to the filtering of turbulent fluctuations. $\bar{\kappa}$ and $\bar{n}_i$ denote the curvature and the ith component of the unit vector indicating the normal direction of the resolved interface with $\bar{\kappa}=-\nabla\cdot\bar{n}$ and $\bar{n}=\nabla\bar{\alpha}/|\nabla\bar{\alpha}|$, respectively. DNS data of spray atomization [46] has revealed that F_s^{tf} is generally small compared to the other terms in the momentum equation, and therefore the sub-grid part of the filtered surface tension force is usually neglected [47, 184, 12]. The sub-grid turbulent stress and sub-grid turbulent flux are closed with gradient viscous and diffusion terms,

$$\tau_{ij}^{tf} = \overline{\rho u_i u_j} - \bar{\rho}\bar{u}_i\bar{u}_j = -2\bar{\rho}\nu_t\bar{S}_{ij}, \tag{4.10}$$

$$J_{\alpha,i}^{tf} = \overline{u_i\alpha} - \bar{u}_i\bar{\alpha} = -D_t\frac{\partial\bar{\alpha}}{\partial x_i}. \tag{4.11}$$

Various models are possible for ν_t and D_t. Here, the Smagorinsky model [237] has been usually used,

$$\nu_t = C_s\Delta^2\sqrt{2\bar{S}_{ij}\bar{S}_{ij}}, \tag{4.12}$$

with the constant $C_s = 0.0197$ and $D_t = \nu_t Sc_t$ with $Sc_t = 1.43$ [225]. The final two terms in Eq. (4.6) are correlations induced by sub-grid fluctuations of density,

$$f_{\rho,i}^{tf} = \frac{(\partial\bar{\rho}\bar{u}_i - \overline{\rho u_i})}{\partial t}, \tag{4.13}$$

$$f_{\mu,i}^{tf} = \frac{\partial\left(2\overline{\mu S_{ij}} - 2\bar{\mu}\bar{S}_{ij}\right)}{\partial x_i}. \tag{4.14}$$

Usually, [47, 184, 12] these are neglected or considered to be encompassed by the model for sub-grid turbulent stress. Two significant conceptual shortcomings in the TFVoF model are presented in this Section. Firstly, the assumption that inertial range turbulent eddies and the energy cascade cross the interface with universal statistical behaviour is not credible. This is particularly relevant in the vicinity of continuous interfaces. Secondly, in regions of low turbulence where D_t is small, the numerical solutions for α and hence all other properties are subject to uncontrolled artificial diffusion due to the grid.

4.2.2 Hybrid turbulence filtering and artificial compression model (TF-AC)

Hecht [98] and subsequently Anez et al. [12] attempted to address the shortcomings in the TFVoF model by augmenting the filtered volume fraction equation with an additional artificial compression term to counteract numerical diffusion and sharpen the interface,

$$\frac{\partial\bar{\alpha}}{\partial t} + \frac{\partial\bar{u}_i\bar{\alpha}}{\partial x_i} + \frac{\partial}{\partial x_i}C_\alpha u_r\bar{\alpha}(1-\bar{\alpha}) = -\frac{\partial J_{\alpha,i}^{tf}}{\partial x_i}(1-C_\alpha). \tag{4.15}$$

The relative velocity,

$$u_r = C_r|\bar{u}_i|\frac{\nabla\bar{\alpha}}{|\nabla\bar{\alpha}|}, \tag{4.16}$$

is non-zero only at the interface where $\nabla\bar{\alpha}$ is finite. Weller [272] suggests that the model parameter C_r ranges from 1 to 4 dependent on the grid resolution. Here we use the standard value of $C_r = 1$. The original formulation was developed for application to laminar or fully resolved simulations [120, 272] and, therefore, sub-grid fluctuations of the artificial compression term have been neglected in Eq. (4.15). This is justified by the fact that the compression term is artificial, but a likely consequence of this simplification is that the impact of the term will be grid dependent. The other parameter C_α is used as a switch. Where the interface is continuous, it is sharpened by setting $C_\alpha = 1$ so that the artificial compression term is activated and turbulent diffusion is de-activated. Where the interface is discontinuous (i.e. where discrete liquid ligaments and droplets exist), $C_\alpha = 0$ and turbulent dispersion becomes dominant. Switching between $C_\alpha = 1$ and $C_\alpha = 0$ is based on a locally evaluated continuous interface indicator,

$$IRQ_\kappa = |\overline{\kappa}|\Delta = \left|\nabla\cdot\frac{\nabla\bar{\alpha}}{|\nabla\bar{\alpha}|}\right|\Delta. \tag{4.17}$$

In the continuous interface region, the magnitude of interface curvature, $\overline{\kappa}$, tends to have smaller values. A threshold value of IRQ_κ is chosen as the point where switching of C_α takes place. In the present study, the threshold is set so that

$$C_\alpha = \begin{cases} 1; & \text{for } IRQ_\kappa <= 0.15 \\ 0; & \text{for } IRQ_\kappa > 0.15 \end{cases},$$

which is similar to the suggestion by Hecht [98].

4.3 Explicit volume diffusion (EVD)

The purpose of developing explicit volume diffusion (EVD) formulation [270] is to have a VoF-type model that presents the interfacial dynamics in a physical manner, is numerically grid independent, and is not unnecessarily affected by numerical diffusion. The explicit volume diffusion model is based on the concept of averaging the VoF equations over explicitly defined physical volumes, which have length scale $l_V \sim V^{1/3}$. This length scale is independent of the grid-scale, Δ, with $\Delta \leq l_V$. The unresolved sub-grid scale interface dynamics are modelled through closures for the sub-volume flux and sub-volume stress. These closures are based on the diffusion coefficient linked with an explicit length scale, and thus this approach is termed as explicit volume diffusion (EVD). A closure for the volume averaged surface tension force is also developed to account for the sub-grid surface tension effects linked with the physically defined explicit length scale. In contrast to the other existing approaches, these closures are independent of the numerical grid scale. This EVD model is applicable to both laminar and turbulent flows. Variations in the fields at the sub-volume scale are filtered out by a physically derived explicit volume diffusion. Unlike turbulence filtering in the TFVoF and TF-AC models presented earlier, the volume averaging attenuates fluctuations due to both the dynamics of the phase interface and turbulent fluctuations (if they exist). Numerical convergence can be demonstrated by reducing Δ while keeping l_V constant so that the explicit volume diffusion remains essentially constant and overwhelms the numerical diffusion, which reduces with Δ.

Within a fixed volume centred at point $\boldsymbol{x_0}$, the volume averaged value is obtained by the spatial averaging of a field ϕ over a physical volume V, written as

$$\widehat{\phi} = \widehat{\phi(\boldsymbol{x_0},t)} = \frac{1}{V}\int_V \phi(\boldsymbol{x}',t)d\boldsymbol{x}', \tag{4.18}$$

where $\boldsymbol{x}'$ is a local coordinate centred at $\boldsymbol{x_0}$ and the integral is performed over all coordinate directions. $\widehat{\cdot}$ is a conventional (or Reynolds) volume average. As the volumes can encompass both fluids with vastly different densities, it is convenient for the derivation of subsequent sub-volume closures to introduce density weighted (Favre) volume averaging.

$$\widetilde{\phi} = \frac{1}{\rho V}\int_V \rho\phi dV = \frac{\widehat{\rho\phi}}{\widehat{\rho}}. \tag{4.19}$$

At the sub-volume scale, the fluctuations relative to the Reynolds and Favre volume averaged quantities are

$$\phi = \widehat{\phi} + \phi' \tag{4.20}$$

and

$$\phi = \widetilde{\phi} + \phi'', \tag{4.21}$$

respectively. Here ϕ' and ϕ'' represent the deviations from mean spatially and density weighted averaged quantities, respectively. Upon having the averaging volume large enough and use of fixed volumes centered at $\boldsymbol{x_0}$, deviations from the mean value are written as

$$\widehat{\widehat{\phi}} = \widehat{\phi}, \widehat{\phi}' = o, \tag{4.22}$$

$$\widetilde{\widetilde{\phi}} = \widetilde{\phi}, \widetilde{\phi}'' = o, \tag{4.23}$$

which leads to convenience in the subsequent manipulations as they avoid unclosed cross interactions between volume averaged fields and sub-volume fluctuations. The definition given by Eq. (4.18) is mathematically similar to a top-hat spatial filtering operation that is commonly used in LES of turbulent flows. The conceptual difference is that the volume averaging is not specifically linked to the filtering of turbulent frequencies above a certain cut-off value. Rather the volume averaging attenuates fluctuations that result from interfacial dynamics that can occur in both laminar and turbulent flows. The use of Favre averaging has the advantage of eliminating the problem associated with simple Reynolds volume averaged momentum transport equations in which additional unclosed terms involving sub-volume variations of density and dynamic viscosity appear. These were simply neglected in the previous work of Chesnel et al. [47], Navarro-Martinez [184] and Ketterl et al. [130], however a priori study by Chesnel [46] reveals that these contributions can in fact be significant. Favre averaging benefits because the governing equations do not contain correlations induced by density fluctuations at the sub-volume scale.

Applying the density weighted or Favre volume averaging operator to Eqs. (2.1), (2.2) and (2.20), finite volume based continuity, momentum and liquid volume fraction equations will take the form of [270]

$$\frac{\partial \widehat{\rho}}{\partial t} + \frac{\partial \widehat{\rho} \widetilde{u}_i}{\partial x_i} = 0, \tag{4.24}$$

$$\frac{\partial \widehat{\rho} \widetilde{u}_i}{\partial t} + \frac{\partial \widehat{\rho} \widetilde{u}_i \widetilde{u}_j}{\partial x_i} = -\frac{\partial \widehat{p}}{\partial x_i} + \frac{\partial \widehat{\tau_{ij}}}{\partial x_i} - \frac{\partial \tau_{ij}^{va}}{\partial x_i} + \widehat{F}_{s,i} + \widehat{\rho} g_i, \tag{4.25}$$

$$\frac{\partial \widehat{\rho}\widetilde{\alpha}}{\partial t} + \frac{\partial \widehat{\rho}\widetilde{\alpha}\widetilde{u_i}}{\partial x_i} = -\frac{\partial J^{va}_{\alpha,i}}{\partial x_i}. \tag{4.26}$$

Density filtered volume averaged viscous stress is written as

$$\widehat{\tau_{ij}} = \widehat{\mu}\left[2\widetilde{S_{ij}} - \frac{2}{3}\frac{\partial \widetilde{u_k}}{\partial x_k}\delta_{ij}\right], \tag{4.27}$$

here $\widetilde{S_{ij}}$ is the filtered strain rate tensor, defined as

$$\widetilde{S_{ij}} = \frac{1}{2}\left(\frac{\partial \widetilde{u_i}}{\partial x_j} + \frac{\partial \widetilde{u_j}}{\partial x_i}\right), \tag{4.28}$$

and δ_{ij} is the Kronecker delta function. Volume averaged single fluid density and dynamic viscosity are calculated by

$$\widehat{\rho} = \rho_g(1-\widehat{\alpha}) + \rho_l\widehat{\alpha} \tag{4.29}$$

and

$$\widehat{\mu} = \rho_g\nu_g(1-\widehat{\alpha}) + \rho_l\nu_l\widehat{\alpha}. \tag{4.30}$$

All the terms having Reynolds volume averages of density in Eqs. (4.24)-(4.26) are replaced with Favre volume averages through the use of Eqs. (4.18) and (4.19). Using the Favre averaged quantities helps eliminate the problems associated with Reynolds volume averaged momentum transport equations. Using the relations for mass conservation of the heavy fluid, the Favre volume averaged solutions to the above equations are easily converted to the physically meaningful Reynolds averaged forms that are of physical interest as

$$\widehat{\alpha} = \frac{\widehat{\rho}\widetilde{\alpha}}{\rho_l}. \tag{4.31}$$

Volume averaging of the transport equations introduced new terms such as sub-volume flux ($J^{va}_{\alpha,i}$), sub-volume stress ($\tau^{va}_{i,j}$) and volume averaged surface tension force ($\widehat{F_s}$), which are given by

$$J^{va}_{\alpha,i} = \widehat{\rho}\widetilde{\alpha'' u''_i}, \tag{4.32}$$

$$\tau^{va}_{ij} = \widehat{\rho}\widetilde{u''_i u''_j} \tag{4.33}$$

and

$$\widehat{F_s} = \widehat{\sigma\kappa\delta n}, \tag{4.34}$$

respectively. The formulations for their closures are presented in the following sections.

4.3.1 Sub-volume fluctuating flux

As the real interface between the two phases is infinitely thin, a bimodal probability density function (PDF) concept is applied here for the volume fraction field at the sub-volume scale to have a closure for the sub-volume flux. A similar approach has been used for modelling the unclosed sub-filter flux and stress for turbulent premixed flames based on a thin flame assumption [31]. The PDF of volume fraction is denoted by $P_\alpha(B)$ where B represents the sample space for the random variable α. The behaviour of $P_\alpha(B)$ is bimodal and its domain is bounded between zero and one. Applying the normalization constraint over the whole range of values, we get

$$\int_{-\infty}^{\infty} P_\alpha(B)dB = P_\alpha(B=1) + P_\alpha(B=0) = 1. \tag{4.35}$$

Similarly, following the same approach, a joint PDF of velocity and volume fraction can be written as

$$\int_{-\infty}^{\infty}\int_{-\infty}^{\infty} P_{\alpha,u}(V,B)dBdV = \int_{-\infty}^{\infty} P_{\alpha,u}(V,B=1)dV + \int_{-\infty}^{\infty} P_{\alpha,u}(V,B=0)dV = 1, \tag{4.36}$$

here V represents the sample space for the velocity variable u. Conditional PDF of u subjected to $\alpha = B$, can be written as

$$P_{u|\alpha}(V|B) = \frac{P_{\alpha,u}(V,B)}{P_\alpha(B)}. \tag{4.37}$$

Based on the bimodel nature of $P_\alpha(B)$, we can have finite values of $P_{u|\alpha}(U|B)$ only when $B = 1$ or $B = 0$, which leads to the sloution as

$$\int_{-\infty}^{\infty} P_{u|\alpha}(V|B=1)dV = \int_{-\infty}^{\infty} P_{u|\alpha}(V|B=0)dV = 1. \tag{4.38}$$

Using the properties of conditional PDF, the volume averaged velocity can be written as

$$\widetilde{u} = \widetilde{u}_g(1-\widetilde{\alpha}) + \widetilde{u}_l\widetilde{\alpha}. \tag{4.39}$$

Within the same fluid, the density is constant and the Favre volume averages are equivalent to the Reynolds values, such that $\widetilde{u}_l = \widehat{u}_l$ and $\widetilde{u}_g = \widehat{u}_g$. The conditional values for velocity in the liquid and gas regions are calculated as

$$\widetilde{u}_l = \int_{-\infty}^{\infty} P_{u|\alpha}(V|B=1)dV \tag{4.40}$$

and

$$\widetilde{u}_g = \int_{-\infty}^{\infty} P_{u|\alpha}(V|B=0)dV. \tag{4.41}$$

Following Eq. 4.39, the sub-volume correlation of the fluctuations of volume fraction and velocity can be written as

$$\widetilde{\alpha'' u_i''} = \widetilde{\alpha}\widetilde{\alpha'' u_i''}_l + (1-\widetilde{\alpha})\widetilde{\alpha'' u_i''}_g. \tag{4.42}$$

The terms $\widetilde{\alpha'' u_i''}_l$ and $\widetilde{\alpha'' u_i''}_g$ can be closed following Eqs. 4.40 and 4.41, written as

$$\widetilde{\alpha'' u_i''} = \widetilde{\alpha} \int_{-\infty}^{\infty} (1-\widetilde{\alpha})(u_i - \widetilde{u_i}) P_{u_i|\alpha}(V_i|B=1) dV_i + (1-\widetilde{\alpha}) \int_{-\infty}^{\infty} (0-\widetilde{\alpha})(u_i - \widetilde{u_i}) P_{u_i|\alpha}(V_i|B=0) dV_i. \tag{4.43}$$

Multiplying Eq. 4.43 by density leads to a solution for sub-volume flux, written as

$$J^{va}_{\alpha,i} = \widehat{\rho}\widetilde{\alpha'' u_i''} = \widehat{\rho}\widetilde{\alpha}(1-\widetilde{\alpha})(\widetilde{u}_{il} - \widetilde{u}_{ig}), \tag{4.44}$$

where $(\widetilde{u}_{il} - \widetilde{u}_{ig})$ represents the mean drift velocity and needs to be closed. Equation 4.44 confirms that sub-volume fluctuations of both the volume fraction and the drift velocity lead to sub-volume flux. These fluctuations are caused by interface dynamics which are present in both laminar and turbulent flows.

For the closure of Eq. 4.44, a gradient diffusion model is proposed, written as

$$J^{va}_{\alpha,i} = -\widehat{\rho} D_v \frac{\partial \widetilde{\alpha}}{\partial x_i}, \tag{4.45}$$

where D_v represents the explicit volume diffusion coefficient and considering the coherent structure of the interface, D_v scales as

$$D_V \approx \left|\frac{Q}{E}\right|^{3/2} \widetilde{\alpha}(1-\widetilde{\alpha}) \left|\widetilde{u}_{il} - \widetilde{u}_{ig}\right| \frac{1}{|\nabla \widetilde{\alpha}|}, \tag{4.46}$$

which implies that the mean drift velocity is modelled using the magnitude of the mean drift velocity vector and the normalized volume fraction gradient

$$\widetilde{u}_{il} - \widetilde{u}_{ig} = -\left|\frac{Q}{E}\right|^{3/2} \left|\widetilde{u}_{il} - \widetilde{u}_{ig}\right| \frac{1}{|\nabla \widetilde{\alpha}|} \frac{\partial \widetilde{\alpha}}{\partial x_i}, \tag{4.47}$$

where $\left|\frac{Q}{E}\right|$ represents the coherent structure function [113, 136] with Q indicates as second invariant of the velocity gradient tensor and E as the magnitude of a velocity gradient tensor, written as

$$Q = \frac{1}{2}\left(\widetilde{W_{ij}}\widetilde{W_{ij}} - \widetilde{S_{ij}}\widetilde{S_{ij}}\right), \tag{4.48}$$

$$E = \frac{1}{2}\left(\widetilde{W_{ij}}\widetilde{W_{ij}} + \widetilde{S_{ij}}\widetilde{S_{ij}}\right). \tag{4.49}$$

Here $\widetilde{W_{ij}}$ is the vorticity tensor, defined as

$$\widetilde{W_{ij}} = \frac{1}{2}\left(\frac{\partial \widetilde{u_i}}{\partial x_j} - \frac{\partial \widetilde{u_j}}{\partial x_i}\right), \tag{4.50}$$

and describes the rate of rotation. A coherent structure function defined as the normalized second invariant $\left|\frac{Q}{E}\right|$ characterizes the relative intensity of homogeneous vorticity to inhomogeneous strain rate in local flows and can be used to identify laminar flows and anisotropic interface flows [136]. High values of $\left|\frac{Q}{E}\right|$ indicate regions of high vorticity such as inhomogeneous or strong shear turbulence, and low values confirm the regions of low vorticity, which are typical in laminar or mildly turbulent flows. $\left|\frac{Q}{E}\right|$ also ensures the volume diffusion is zero for two parallel immiscible fluids corresponding to no divergence of sub-volume flux, and $\frac{\partial J^{va}_{\alpha,i}}{\partial x_i} = 0$ under this condition. This is especially important for a jet spray atomization case where no additional diffusion is induced for predictions of the spray break-up. The magnitude of the mean drift velocity $|u_{il} - u_{ig}|$ is correlated with the sub-volume velocity fluctuations. Applying the conditional PDF concept, the closure for u''can be derived as

$$\begin{aligned} \widetilde{u_i''^2} &= \widetilde{\alpha}\widehat{u_i''^2}_l + (1-\widetilde{\alpha})\,\widehat{u_i''^2}_g \\ = \widetilde{\alpha}\int_{-\infty}^{\infty}(u_i - \widetilde{u_i})^2 P_{\alpha|u}(V|B=1)dV &+ (1-\widetilde{\alpha})\int_{-\infty}^{\infty}(u_i - \widetilde{u_i})^2 P_{\alpha|u}(V|B=1)dV \\ &= \widetilde{\alpha}\,(1-\widetilde{\alpha})\left(\widetilde{u}_{il} - \widetilde{u}_{ig}\right)^2 + \widetilde{\alpha}\widetilde{u_i''^2}_l + (1-\widetilde{\alpha})\,\widetilde{u_i''^2}_g. \end{aligned} \tag{4.51}$$

Here, $u_l'' = u_l - \widetilde{u}_l$ and $u_g'' = u_g - \widetilde{u}_g$ are the velocity fluctuations of the corresponding fluids, and $\widetilde{u_i''^2}_l$ and $\widetilde{u_i''^2}_g$ are the sub-volume variances. Following the Eq. 4.51, the magnitude of drift velocity can be expressed as

$$\left|\widetilde{u}_{il}-\widetilde{u}_{ig}\right| = \frac{\sqrt{\widetilde{u_i''^2}-\widetilde{\alpha}\widetilde{u_i''^2}_l-(1-\widetilde{\alpha})\,\widetilde{u_i''^2}_g}}{\sqrt{\widetilde{\alpha}\,(1-\widetilde{\alpha})}}. \tag{4.52}$$

The above equation can be re-arranged as

$$\left|\widetilde{u}_{il}-\widetilde{u}_{ig}\right|\sqrt{\widetilde{\alpha}\,(1-\widetilde{\alpha})} = \sqrt{\widetilde{u_i''^2}-\widetilde{\alpha}\widetilde{u_i''^2}_l-(1-\widetilde{\alpha})\,\widetilde{u_i''^2}_g}. \tag{4.53}$$

The term on the right side of Eq. 4.53 explicitly indicates that the sub-volume velocity fluctuations conditional on being in the pure liquid and gas phases are subtracted from the total sub-volume velocity fluctuations to obtain the sub-volume velocity fluctuations due to interface dynamics alone.The fluctuating energy terms, $\widetilde{u_i''^2}$, $\widetilde{u_i''^2}_l$ and $\widetilde{u_i''^2}_g$ are still unclosed. Away from the interface within the pure liquid fluid stream, $\widetilde{u_i''^2}_l = \widetilde{u_i''}^2$, and within the pure gaseous fluid stream, $\widetilde{u_i''^2}_g = \widetilde{u_i''}^2$. The fluctuating energy terms, $\widetilde{u_i''^2}$, $\widetilde{u_i''^2}_l$ and $\widetilde{u_i''^2}_g$ are still unclosed. By applying limits, we get

$$\lim_{\widetilde{\alpha}\to 0}\sqrt{\widetilde{u_i''^2}-\widetilde{\alpha}\widetilde{u_i''^2}_l-(1-\widetilde{\alpha})\,\widetilde{u_i''^2}_g} = 0 \tag{4.54}$$

and

$$\lim_{\widetilde{\alpha}\to 1}\sqrt{\widetilde{u_i''^2}-\widetilde{\alpha}\widetilde{u_i''^2}_l-(1-\widetilde{\alpha})\,\widetilde{u_i''^2}_g} = 0, \tag{4.55}$$

which leads to the condition that D_v is non zero only at the interface. From empirical observation of interfacial regions of resolved flow simulations, Wang et al. [270] introduces the functional approximation, written as

$$\sqrt{\widetilde{u_i''^2}-\widetilde{\alpha}\widetilde{u_i''^2}_l-(1-\widetilde{\alpha})\,\widetilde{u_i''^2}_g} \approx \sqrt{\widetilde{\alpha}\,(1-\widetilde{\alpha})\,\widetilde{u_i''^2}} \approx \sqrt{\widetilde{\alpha}\,(1-\widetilde{\alpha})}\left|u_V''\right|. \tag{4.56}$$

The solution presented in Eq. 4.53 applies to both turbulent and laminar flows, and sub-volume velocity fluctuations are non zero within the interfacial regions. The sub-volume velocity fluctuating, $|u''_V|$, is suggested by Wang et al. [270] to be modeled following Smagorinsky-Lilly model [237, 149], written as

$$|u''_V| = C_{SL}\frac{\nu_V}{l_V} = C_{SL} l_V \sqrt{2\widetilde{S_{ij}}\widetilde{S_{ij}}}, \tag{4.57}$$

where the value of constant C_{SL} is taken as 0.33 for laminar and 0.66 for turbulent flows. These values are determined based on a priori analysis conducted by Wang et al. [270]. This model is inspired from sub-filter turbulence closures, but it covers fluctuations due to interface dynamics and turbulence (for the case of turbulent flows). Most importantly, the model for $|u''_V|$ is linked to the explicit volume length scale, l_V, and is strictly independent of the numerical grid scale. In the vicinity of a sharp interface, the sub-volume velocity fluctuations are highly anisotropic. This fact is not contradicted by Eq. 4.53, which implies only that the magnitude of the sub-volume velocity fluctuations scale with the volume averaged strain rate. This is physically plausible because both velocity fluctuations and strain rate positively correlate with the drift velocity between the phases.

However, $|\nabla\widetilde{\alpha}|$ which appears in the denominator in the solution of D_v, and can lead to the destabilized solution as its value is zero away from the interface. Therefore, the following approximation is employed to avoid this unnecessary destabilization, written as

$$|\nabla\widetilde{\alpha}| \approx \frac{\sqrt{|\alpha''|^2}}{l_V} = \frac{\sqrt{\widetilde{\alpha}\,(1-\widetilde{\alpha})}}{l_V}, \tag{4.58}$$

here $\sqrt{|\alpha''|^2} = \sqrt{\widetilde{\alpha}\,(1-\widetilde{\alpha})}$ is calculated following the similar conditional averaging as expressed in Eq. 4.43. Following the solutions provided n Eqs. 4.46, 4.52 and 4.56 - 4.58, we can have the final solution for explicit volume diffusion coefficient, written as

$$D_v = C_{\alpha u}\left|\frac{Q}{E}\right|^{3/2} l_V^2 \sqrt{\widetilde{\alpha}\,(1-\widetilde{\alpha})}\sqrt{2\widetilde{S_{ij}}\widetilde{S_{ij}}}, \tag{4.59}$$

where the modelling constant $C_{\alpha u}$ incorporates the constant C_{SL} and is calibrated using a priori analysis performed by [270]. The value for $C_{\alpha u}$ used here is 0.25.

4.3.2 Sub-volume stress

Following a similar derivation, as used for the sub-volume flux above, the closure for sub-volume stress is modelled as,

$$\begin{aligned}\tau_{ij}^{va} = \widehat{\rho}\widetilde{u''_i u''_j} = \widehat{\rho}\widetilde{\alpha}(1-\widetilde{\alpha})(\widetilde{u}_{il}-\widetilde{u}_{ig})(\widetilde{u}_{j_l}-\widetilde{u}_{j_g}) \\ +\widehat{\rho}\left[\widetilde{\alpha u'_{il}u'_{j_l}}+(1-\widetilde{\alpha})\widetilde{u'_{i_g}u'_{j_g}}\right].\end{aligned} \tag{4.60}$$

Eq. 4.60 for sub-volume stress has two parts where the first term on the right side is related to the sub-volume flux in the interface region and using the Boussinesq viscosity assumption described for free shear flows having turbulent and non-turbulent interfaces [273], the sub-volume stress is assumed to be proportional to the strain rate, written as

$$\widehat{\rho}\widetilde{\alpha}(1-\widetilde{\alpha})(\widetilde{u}_{il}-\widetilde{u}_{ig})(\widetilde{u}_{j_l}-\widetilde{u}_{j_g}) = -2\widehat{\rho}\nu_V\widetilde{S_{ij}}, \tag{4.61}$$

where ν_V is the explicit volume viscosity. In the regions where $0 < \widetilde{\alpha} < 1$, ν_V is calculated from the explicit volume diffusion coefficient via a Schmidt number as

$$\nu_V = Sc_V D_V. \tag{4.62}$$

Away from the interfacial regions, where $\alpha = 1$ or $\alpha = o$, sub-volume velocity fluctuations are not zero, specifically in the case of turbulent flows. Hence, the explicit volume viscosity away from the interface can be modelled by following the Smagorinsky model [237], expressed as

$$\nu_t = C_s l_V^2 \sqrt{2\widetilde{S_{ij}}\widetilde{S_{ij}}}, \tag{4.63}$$

where the value for constant C_s is used as 0.15. The second term on the right hand side of Eq. 4.60, $\widetilde{\alpha u'_{il}u'_{j_l}} + (1-\widetilde{\alpha})\widetilde{u'_{i_g}u'_{j_g}}$ is characterized by the fluctuations respect to the corresponding fluids. This term can be neglected in streams of laminar regimes. However, in turbulent flows, it is considered to be correlated with the sub-filter turbulence stress where the filter width is equivalent to the sub-volume length scale, written as

$$\begin{aligned}
&\left[\widetilde{\alpha}\widetilde{u'_{i_l}u'_{j_l}} + (1-\widetilde{\alpha})\widetilde{u'_{i_g}u'_{j_g}}\right] \\
&= \widetilde{\rho}\left[\widetilde{\alpha}\overline{u'_{i_l}u'_{j_l}} + (1-\widetilde{\alpha})\overline{u'_{i_g}u'_{j_g}}\right] \\
&\cong \widehat{\rho}\,[1-4\widetilde{\alpha}(1-\widetilde{\alpha})]\,\widetilde{u'_i u'_j} \\
&= -\widehat{\rho}\nu_t\,[1-4\widetilde{\alpha}(1-\widetilde{\alpha})]\left[2\widetilde{S_{ij}}\right].
\end{aligned} \tag{4.64}$$

Following the Eqs. 4.61, 4.62 and 4.64,sub-volume stress τ_{ij}^{va} is expressed as

$$\tau_{ij}^{va} = -2\widehat{\rho}(Sc_V D_V + \nu_t\,[1-4\widetilde{\alpha}(1-\widetilde{\alpha})])\widetilde{S_{ij}} \tag{4.65}$$

Based on the a priori analysis conducted by Wang et al. [270], the value of the explicit volume Schmidt number used in this study is $Sc_V = 3$.

4.3.3 Volume averaged surface tension force

The most common closure for surface tension force in VoF based formulations is based on the continuous surface force (CSF) method of Brackbill et al. [30], written as

$$\widehat{F_s} = \sigma\widehat{\kappa\delta n} = \sigma(\widehat{\kappa n|\nabla\alpha|}), \tag{4.66}$$

where σ is the surface tension coefficient, $\kappa = \nabla.n$ is the interface curvature calculated through the unit normal vector $n = \frac{\nabla\alpha}{|\nabla\alpha|}$ and δ is the Dirac delta function used for interface detection. Considering a volume, V, of fluid, the integral over the volume V of a function $f(x,t)$, weighted by the magnitude of the gradient of a scalar field, $|\nabla\phi(x,t)|$,can be shown to be equal to the sum over all the iso-surfaces defined by $\Psi = \phi(x,t)$ of the surface integral of the function $f(x,t)$. Following the $(n-1)$ dimensional Hausdorff approach [165], the volume integral can be transformed to the surface integral as

$$\int_V f(x,t)|\nabla\phi(x,t)|dV = \int_0^1 d\Psi \int_{A_\phi} f(x,t)dA(x). \tag{4.67}$$

The continuum surface tension model has been widely used [230, 94, 47, 184] for LES and DNS of spray atomization with and without considering the sub-grid surface tension effects, but having a suitable closure solution for the sub-grid fluctuations of surface tension is still a challenge. Following Eq. (4.67) and integrating Eq. (4.66) over an explicit volume and simplifying, we get

$$\begin{aligned}\widehat{F_s} = \sigma(\widehat{\kappa n|\nabla\alpha|}) = \sigma\frac{1}{V}\int_{A_s}\kappa n dA(x)\\ = \sigma\frac{1}{V}\langle\kappa n\rangle_s A_s = \sigma\langle\kappa n\rangle_s\Sigma \cong C_{sf}\sigma\widehat{\kappa}\widehat{n}\Sigma,\end{aligned} \tag{4.68}$$

where $\widehat{\kappa}$ and $\widehat{n}$ indicate the curvature and normal vector of the volume averaged interface curve, $\widehat{\kappa} = \nabla.\widehat{n}$ and $\widehat{n} = \frac{\nabla\widehat{\alpha}}{|\nabla\widehat{\alpha}|}$. A_s is the surface area of the interface and $\langle.\rangle_s$ indicates the surface mean value. Σ represents the surface density and is defined as

$$\Sigma = \frac{A_s}{V} = \frac{1}{V}\int_V \delta(\Psi - \alpha(x,t))|\nabla\alpha(x,t)|dV = \widehat{|\nabla\alpha|}. \tag{4.69}$$

The surface density is modelled by following the dynamic wrinkling concept used by Hawkes and Cant [95] and Charlette et al. [42], written as

$$\Sigma = \Xi|\nabla\widehat{\alpha}|. \tag{4.70}$$

The dynamic wrinkling factor,Ξ, can be defined by the fractal dimension concept [95, 42] by using the physical volume length scale, l_V , and the interface cut-off length scale, l_σ ,expressed as

$$\Xi = \left(1 + \frac{l_V}{l_\sigma}\right)^{D_f - 2}, \tag{4.71}$$

where D_f is the fractal dimension of the interface and is estimated as $7/3$ for mild wrinkling. The interface cut-off length scale,l_σ, where the surface tension on that scale balances inertia when the Weber number $We = \frac{\rho_h|u''|^2 l_\sigma}{\sigma} \cong 1$. Thus, the surface cut-off length scale is given by

$$l_\sigma = \frac{\sigma}{\rho_h|u''|^2}. \tag{4.72}$$

Now, the volume averaged surface tension force will take the form of

$$\widehat{F_s} = C_{sf} \left(1 + \frac{\Delta_V \rho_h |u''|^2}{\sigma} \right)^{1/3} \sigma \widehat{\kappa} \widehat{n} |\nabla \widehat{\alpha}|. \tag{4.73}$$

The modelling constant, C_{sf}, was calibrated by the resolved flow simulations conducted by Wang et al. [270]. In the vicinity of a sharp interface, the sub-volume velocity fluctuations are highly anisotropic. This fact is not contradicted by Eq. (4.57), which implies only that the magnitude of the sub-volume velocity fluctuations scale with the volume averaged strain rate. This is physically possible because both velocity fluctuations and strain rate are positively correlated with the drift velocity between the phases. A priori analysis against resolved flow simulations [270] suggests that $C_{SL} = 0.66$ and $C_{sf} = 1.8$.

The explicit volume length scale l_V is a physical scale that needs to be selected based on the physical flow parameters. These characteristic physical parameters related to the evolution of interfacial flows include wavelengths, wave amplitudes, interface boundary layer thicknesses and turbulence (for the case of turbulent flows). When the level of interfacial instabilities increases, explicit volume diffusion smears [270] the volume fraction in the direction normal to the interface and the explicit volume length scale l_V can be linked with the wave amplitude. Both the wavelength and amplitude of the interfacial instabilities depend on the interface boundary layer thickness that develops in both fluids normal to the interface. Findings of Marmottant and Villermaux [162] confirm that these instabilities mainly depend on the boundary layer thickness developed in the lighter fluid. For the laminar flow, it is calculated as

$$\xi \cong 5.6 Z Re_g^{-0.5}, \tag{4.74}$$

and for turbulent flow, calculated as

$$\xi \cong 74 Z Re_g^{-0.75}, \tag{4.75}$$

where, $Re_g = u_g Z / \nu_g$ with Z being the outer scale of the shear layer. u_g and ν_g are the velocity and kinematic viscosity of the light fluid, respectively. Wang et al. [270] suggest that l_V should be no larger than the boundary layer thickness on the gas side of the interface, for which some empirical approximations are available [162]. Additionally, numerical convergence is achieved when l_V is several times larger than the LES grid size, Δ. In combination, these two requirements ensure that the smearing of the boundary layer due to volume averaging is not excessive and that the explicit volume diffusion remains sufficiently large to overwhelm numerical diffusion. The details regarding the value of the explicit volume length scale, the experimentally estimated boundary layer thickness on the gas side of the interface and the LES grid size to explicit volume length scale ratios Δ/l_V are presented in Section 5.3.

4.4 Surface density

Another important parameter, surface density, is also solved for analysis to evaluate the numerical convergence of the three models for sub-volume interface dynamics. The complete details of surface density and physics involved in developing its governing equation are presented in Section 3.2. Following the previous work [47, 184, 12], TFVoF and TF-AC share the same approach to solve the surface density. The surface density, $\bar{\Sigma}$, is decomposed into an intrinsic minimum surface density referring to the static liquid-gas mixture and a dynamic component induced by turbulent flows. The minimum surface density can be approximated as [47, 184]

$$\bar{\Sigma}_{min} = C_{\Sigma}\sqrt{\bar{\alpha}\,(1-\bar{\alpha})}, \tag{4.76}$$

where $\bar{\Sigma}_{min}$ represents the minimum surface density. Based on his DNS findings, Chesnel [46] finds that the optimal value of constant C_{Σ} is 2.4. The dynamic component, $\bar{\Sigma}_t$, is solved by the transport equation

$$\frac{\partial \bar{\Sigma}_t}{\partial t} + \frac{\partial \bar{u}_i \bar{\Sigma}_t}{\partial x_i} = \frac{\partial}{\partial x_i} D_t \frac{\partial \bar{\Sigma}_t}{\partial x_i} + S_{\Sigma}. \tag{4.77}$$

The modelling of source term S_{Σ} is based on the correlation of turbulence phenomenon and related time scales. In context of equilibrium restoration [263, 144, 22], the source term expressed in Eq. (4.77) can be written as

$$S_{\Sigma} = \frac{\bar{\Sigma}}{\tau_t}\left(1 - \frac{\bar{\Sigma}}{\bar{\Sigma}_{eq}}\right), \tag{4.78}$$

where $\widehat{\Sigma}_{eq}$ represents the equilibrium surface density and τ is the corresponding turbulent time scale. Estimation of $\widehat{\Sigma}_{eq}$ is based on the assumption of equilibrium of surface energy with the local kinetic energy. The equilibrium surface density, $\bar{\Sigma}_{eq}$, can be decomposed into an intrinsic minimum part and a dynamic contribution in order to maintain model coherence, such that

$$\bar{\Sigma}_{eq} = \bar{\Sigma}_{min} + \bar{\Sigma}_{t,eq}. \tag{4.79}$$

$\bar{\Sigma}_{t,eq}$ is determined by liquid volume fraction, $\bar{\alpha}$, and sub-filter turbulent energy, k, [184] following Duret et al. [69], written as

$$\bar{\Sigma}_{t,eq} = \bar{\alpha}\,(1-\bar{\alpha})\,\frac{2\,(\rho_l+\rho_g)\,k}{\sigma We^*}, \tag{4.80}$$

where We^* is a critical Weber number and can be approximated as 1. Using the volume diffusion concept, the transport equation for the corresponding dynamic component, $\widetilde{\Sigma_t}$, is given by

$$\frac{\partial\widehat{\rho}\widetilde{\Sigma_t}}{\partial t}+\frac{\partial\widehat{\rho}\widetilde{u}_i\widetilde{\Sigma_t}}{\partial x_i}=\frac{\partial}{\partial x_i}\widehat{\rho}D_V\frac{\partial\widetilde{\Sigma_t}}{\partial x_i}+\frac{1}{\widehat{\rho}}S_\Sigma. \tag{4.81}$$

As the volumes can encompass both fluids with vastly different densities, it is convenient for the derivation of subsequent sub-volume closures to introduce density weighted (Favre) volume averaging following the Eq. (4.19), written as

$$\widetilde{\Sigma_t} = \widehat{\Sigma_t\rho}/\widehat{\rho}. \tag{4.82}$$

4.5 Sub-grid surface tension

As discussed in preceding Sections 4.2 and 4.3, sub-grid surface tension effects are neglected for both TFVoF and TF-AC formulations. However, the EVD approach is presented with and without considering the sub-volume contribution of the surface tension force. Here, a different approach, originally developed by Shirani et al. [232, 231], is followed to capture the sub-grid effects of pressure jump across the interface. As the accurate capturing of the sub-grid surface tension effects for the multi-phase flows is still in the early stages of development, another way of calculating the sub-grid surface tension is presented here. This formulation is used in combination with conventional solutions for the VoF approach presented in Section 4.2 and the newly developed EVD approach presented in Section 4.3. The comparison is made of the solutions with and without considering the sub-volume surface tension effects as presented in Section 4.3.3.

Considering a 2-D cell containing an interface between two fluids, as shown in Fig. 4.1. To derive the relation for the pressure jump across the interface, first, we will calculate the pressure force on the left side of the cell shown in Fig. 4.1, written as

$$P_{Fl} = P_{1l}\frac{L_1}{\Delta Y} + P_{2l}\left(\frac{\Delta Y - L_1}{\Delta Y}\right), \tag{4.83}$$

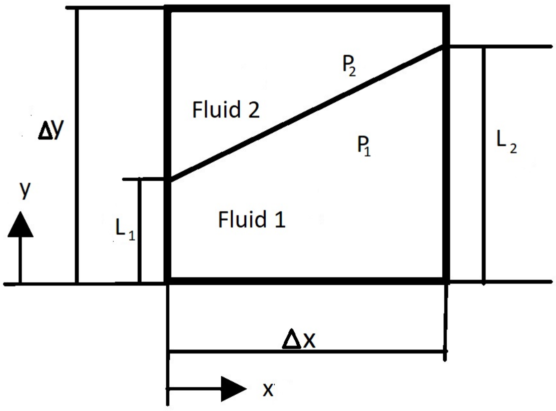

Fig. 4.1 Schematic diagram showing cell with interface

where P_{Fl} is the pressure force acting on the left side of the cell, P_{1l} is pressure force on the left wall because of fluid 1 and P_{2l} is pressure force on the left wall because of fluid 2. ΔY is cell length in the y direction, L_1 is the length of the left side of the cell in contact with fluid 1, and $\Delta Y - L_1$ is the corresponding length of the cell in contact with fluid 2. Suppose $Z_l = \frac{L_1}{\Delta Y}$ represents the ratio of the length filled with fluid 1, and indicates the location of the instantaneous interface location on the left side of the cell. The Eq. (4.83) will take the form of

$$P_l = Z_l P_{1l} + (1 - Z_l) P_{2l} = P_{2l} + Z_l (P_{1l} - P_{2l}), \tag{4.84}$$

where the second term on the right side of the above equation represents the pressure jump across the interface because of the surface tension. Similarly, we can have the relations of the pressure force for the right side, top and bottom of the cell. Generally, we can write

$$P = P_2 + Z(P_1 - P_2). \tag{4.85}$$

On applying the Reynolds averaging to the Eq. (4.85), we can get

$$\bar{p} = \bar{p_2} + \bar{Z}(\bar{p_1} - \bar{p_2}) + \overline{Z'(p'_1 - p'_2)} \tag{4.86}$$

As the surface tension forces at the interface cause this pressure jump across the interface, so Eq. (4.86) in terms of surface tension can be written as

$$\bar{p} = \bar{p_2} + \sigma\bar{\kappa}\bar{Z} + \sigma\overline{\kappa' Z'}. \tag{4.87}$$

This approach is based on modelling the instantaneous curvature of the fluctuating interface, and the term including the correlation of fluctuations of curvature and interface location $\overline{\kappa' Z'}$ needs to be modelled to include the sub-grid scale turbulent effects. Considering that L is a length scale linked with the mesh size and l is the turbulent integral length scale then the fluctuation of Z in a control volume is calculated as l'/L, where l' represents the instantaneous fluctuations of the interface thickness. Using the Taylor microscale Λ as the characteristic length scale for the curvature, this can be modelled as

$$\overline{\kappa' Z'} = C'(l/L\Lambda), \tag{4.88}$$

where C' is a positive correlation coefficient between Z' and κ' and is assumed to be constant. Considering the presence of homogeneous isotropic turbulence and the rate of decay for turbulent kinetic energy equal to the rate of dissipation, the Taylor microscale can be expressed as

$$\Lambda = (10\nu k/\varepsilon)^{1/2}. \tag{4.89}$$

Turbulent integral length scale, l, can be expressed in terms of k and ε

$$l = C_\mu(k^{3/2}/\varepsilon). \tag{4.90}$$

From Eqs. (4.89) and (4.90), we have

$$\Lambda/l = (10/Re_\tau)^{1/2}, \tag{4.91}$$

where $Re_\tau$is the turbulent Reynolds number, expressed as

$$Re_\tau = \sqrt{k}l/\nu = C_\mu(k^2/\nu\varepsilon) = \nu_\tau/\nu. \tag{4.92}$$

Here ν_τ represents the kinematic eddy viscosity. Combining Eqs. (4.91) and (4.88), we can get

$$\overline{\kappa' Z'} = C_p(Re_\tau^{1/2}/L) = C_p/L(\nu_\tau/\nu)^{1/2}, \tag{4.93}$$

where C_p is the model constant and can be replaced by correlation coefficient C', and its value needs to be determined. From the comparison of Eqs. (4.86), (4.87) and (4.93), we can have

$$\overline{Z'(p_1' - p_2')} = \sigma\overline{\kappa' Z'} = C'\sigma/L(\nu_\tau/\nu)^{1/2}. \tag{4.94}$$

As L is dependent on the mesh size x and the mean curvature has the maximum value of $2/x$,and we can replace the $1/L$ by the mean curvature $(1/L \approx \bar{\kappa})$, written as

$$\overline{Z'(p_1' - p_2')} = \sigma\overline{\kappa' Z'} = C'\sigma\bar{\kappa}(\nu_\tau/\nu)^{1/2}. \tag{4.95}$$

Alternatively, we can write

$$\overline{\kappa' Z'} = C'\bar{\kappa}(\nu_\tau/\nu)^{1/2}. \tag{4.96}$$

From above equation, we can conclude that sub-grid curvature fluctuations can be included by increasing the mean curvature $\bar{\kappa}$ by a factor $(\nu_\tau/\nu)^{1/2}$. This conclusion is consistent with Alajbegovic's findings [9] that the unresolved curvature should be proportional to the resolved curvature with a coefficient of proportionality that is dependent on the sub-grid stresses ν_τ. Similarly, considering the Eq. (4.95), we can say that the surface tension force in turbulent flows is increased by a factor of $(\nu_\tau/\nu)^{1/2}$ when the sub-grid effects are accounted. For both TFVoF and TF-AC, sub-grid surface tension can be expressed as

$$F_{s,i}^{tf} = \sigma\bar{\kappa}\bar{n}_i|\nabla\bar{\alpha}|(\nu_\tau/\nu)^{1/2}. \tag{4.97}$$

Combining Eqs. (4.9) and (4.97), we get

$$\bar{F}_{s,i} = \sigma\bar{\kappa}\bar{n}_i|\nabla\bar{\alpha}|(1+(\nu_\tau/\nu)^{1/2}). \tag{4.98}$$

Similarly, upon applying density weighted (Favre) volume averaging to the Eq. (4.85) and comparing it with the EVD formulation Eq. (5.3), we can have

$$\widehat{F_{s,i}} = \sigma\widehat{\kappa}\widehat{n_i}|\nabla\widehat{\alpha}|(1+(\nu_\tau/\nu)^{1/2}). \tag{4.99}$$

4.6 Summary

Three different LES treatment for unresolved sub-grid fluctuations TFVoF,TF-AC and EVD has been discussed in Sections 4.2 - 4.3, and the relevant LES description of surface density is explained in Section 4.4. These approaches are distinguished by different modelling strategies of unresolved fluctuations at the liquid-air interface of a two-phase flow. In general, these fluctuations can be due to interface dynamics and turbulence. TFVoF applies conventional turbulence filtering with a sub-grid turbulent viscosity model to the VoF equations to account for all sub-grid fluctuations. There are two significant conceptual shortcomings associated with TFVoF: i) the assumption that inertial range turbulent eddies and the energy cascade cross the interface with universal statistical behaviour is not valid for two-phase flows, ii) in regions of low turbulence where turbulent diffusion is small the numerical solutions are sensitive to artificial diffusion due to the grid. Moreover, linking the turbulence filter size with LES cell size leads to a grid-dependent value of turbulent viscosity. TF-AC attempts to account for more sub-grid interface dynamics by introducing additional artificial compression in the continuous interface region to counteract the numerical diffusion and thus sharpen the interface. However, a modelling constant C_r inherent in the artificial compression term is likely to depend on grid resolution. The conventional turbulent viscosity model is only activated in the discrete phase region. Additionally, the effects of sub-grid fluctuations of surface tension forces are also neglected in both TFVoF and TF-AC. The newly developed EVD [270] is based on averaging over explicitly defined physical volumes. The volume length scale, l_V, is independent of the grid scale and should not be larger than the boundary layer thickness on the gas side of the liquid-air interface. Sub-volume fluctuations due to inhomogeneous phase fields and mean drift velocity is modelled by a physically derived explicit volume diffusion coefficient and related explicit volume viscosity. As will be shown below in Section 5.4.3, the numerical convergence problem can be avoided by refining grids while keeping the physical volumes constant so that the explicit volume diffusion overwhelms the numerical diffusion, which reduces with the refinement of the grid. The EVD model also includes an improved volume averaged surface tension model based on fractal properties of wrinkled sub-volume interfaces.

Furthermore, a pressure difference based sub-grid surface tension solution is presented in Section 4.5, and to test the sensitivity of the models to the surface tension treatment, it will be incorporated in all three TFVoF, TF-AC and EVD modelling approach. The findings and behaviour of these three different LES formulations with and without sub-grid surface tension are presented in Chapter 5.

Chapter 5

Performance Analysis of Conventional VoF Methods and new EVD Approach

This chapter aims to perform a detailed comparison of the numerical convergence and accuracy of three VoF based methods for turbulent atomizing sprays; namely, the turbulent filtered VoF model (TFVoF), the hybrid turbulence filtering and artificial compression model (TF-AC), and the explicit volume diffusion model (EVD). Moreover, a detailed analysis of the sub-grid surface tension effects is also presented here. The formulation of these models and the relevant sub-grid surface tension sub-models is given in Chapter 4. The first half of this chapter describes the numerical implementation in OpenFOAM along with the discretization schemes and relevant solution solvers. The two experimental air-blast spray jet cases used for model comparison and the computational setup are also discussed here. Initially, results for all three LES approaches applied to the lower Weber number case ($We = 35$) are presented. Numerical convergence with the grid refinement is evaluated through a detailed comparison of axial and radial profiles of the mean and rms of volume fraction, velocity and surface density. The accuracy of volume fraction is assessed by comparison to the available experimental data. The numerical performance is also evaluated using the canonical Zalesak's disc experiment and Richardson Extrapolation analysis. Subsequently, an improved closure for the EVD surface tension force is tested for the $We = 35$ case. Implementation of the pressure difference based surface tension sub-model is tested for all three formulations. For the EVD approach, the sensitivity of the numerical performance to the variations in the explicit length scale is also conducted, which may be linked to the boundary layer thickness on the gaseous side of the interface. Finally, the EVD model with the optimum numerical parameters and surface tension model is further evaluated against experimental data for a higher Weber number test case ($We = 72$).

5.1 Numerical setup and implementation

The TFVoF, TF-AC and EVD models have been implemented in OpenFOAM and Klein's digital filter is used to generate realistic turbulent fields. The TFVoF and TF-AC schemes are relatively simple modifications of the interFoam solver [272] originally written for the unfiltered VoF equations with artificial compression. The modifications introduced here involve adding the sub-grid turbulent flux term on the right hand side of Eq. (4.15). For TFVoF simulations, $C_\alpha = 0$ is applied globally throughout the domain such that Eq. (4.15) reverts to Eq. (4.7). For TF-AC simulations, the switching criteria IRQ_κ given by Eq. (4.17) is implemented, and C_α takes locally and temporally determined values of either zero or one. The EVD model is implemented in a new solver called evdFoam. The volume averaged transport equations are solved on the LES mesh giving grid values of the properties, e.g. $\widehat{\rho}^\Delta$, $\widehat{\alpha}^\Delta$ and $\widehat{u_i}^\Delta$. A second mesh of length scale $l_V > \Delta$ is used for calculating the explicit volume diffusion coefficient D_V. This requires integrating each of the quantities in Eq. (4.59) over all LES cells inside each explicit volume. For example, the integrated volume fraction is given by

$$\widetilde{\alpha}^V = \frac{\int_V \widehat{\rho}^\Delta \widetilde{\alpha}^\Delta dV}{\widehat{\rho}}, \tag{5.1}$$

and the integrated velocity is

$$\widetilde{u_i}^V = \frac{\int_V \widehat{\rho}^\Delta \widetilde{u_i}^\Delta dV}{\widehat{\rho}}. \tag{5.2}$$

Once D_V^V is known, the values at the LES cells, D_V^Δ, that are needed to solve the transport equations are obtained by linear interpolation.

Some additional explanation is needed about including the surface tension force in the EVD simulations. To facilitate direct comparison to the TFVoF and TF-AC models, the surface tension on the LES grid neglecting the sub-grid fluctuations is implemented as

$$\widehat{F_{s,i}}^\Delta = \sigma \widehat{\kappa}^\Delta \widehat{n_i}^\Delta \left| \nabla \widehat{\alpha}^\Delta \right|. \tag{5.3}$$

In the simulations which use the improved volume averaged surface tension force given by Eq. (4.73), the magnitude of the force at each LES cell, $\widehat{F_s}^\Delta$, is obtained by linear interpolation from the integrated values on the explicit volume mesh, $\widehat{F_s}^V$. To better capture the interface dynamics, the direction of the force is given directly from the grid resolved interface normal direction. The turbulence filtering, artificial compression and volume averaging operations for the three approaches do not violate the mass conservation which is inherent to the VoF algorithm. In the test cases investigated here, the maximum interface Courant number is

$Co_i = 0.25$, but since the numerical method integrates the volume fraction over four sub-steps, it is effectively 0.0625. At the same time the maximum flow Courant number is $Co_f = 0.75$.

5.2 Zalesak's Disc test case analysis

The three approaches introduced in Sections 4.2.1, 4.2.2 and 4.3 are evaluated for the canonical two-phase flow called Zalesak's Disc, in which a slotted circle of heavy fluid moves in a pure rotating velocity field. Since no turbulence exists, sub-grid turbulence is eliminated, and the TFVoF and TF-AC revert to the standard VoF and AC models, respectively. However, sub-volume fluctuations in the EVD model due to laminar interface dynamics remain and cannot be neglected. In this particular test, the 2D computational domain 2 m × 2 m and centered at (0,0). The disc is initially positioned at (0,0.5) with a radius of 0.3 m. The height and width of the slot are 0.5 m and 0.1 m, respectively. The rotating velocity is given by $u = (-2\pi y, 2\pi x)$ where x and y denote the coordinates. The disc is filled with acetone and is surrounded by air. The results in a zoomed window after one third of rotation are presented in Fig. 5.1, two third of rotation are presented in Fig. 5.2 and one complete rotation are presented in Fig. 5.3. The first three rows show the grid sensitivity for VoF, AC and EVD, respectively, for three different mesh resolutions such as 400×400, 800×800 and 1600×1600. As expected, due to the dominance of numerical diffusion, the VoF results have a visible variation of the interface topology with grid resolution, especially on the corners of the slot. For AC, the numerical diffusion is (partially) counteracted by the numerical compression velocity leading to a significantly sharper interface and less variation with grid refinement, although differences remain near the corners. [281, 214].

The third row shows the volume averaged results for EVD where the explicit volume length scale is $l_V = 0.01$, and the ratios of the numerical grid scale are $\Delta / l_V = 1/4$, 1/8 and 1/16, respectively. The explicit volume diffusivity thickens the interface, as can be seen in comparison to the thickness of the VoF interface, which results only through numerical diffusion. The explicit volume diffusion is clearly much more significant. For EVD, the result appears to be numerically converged with only 800×800 cells. In the fourth row, l_V is increased by a factor of two relative to the third row. This increases explicit volume diffusion even further relative to numerical diffusion, accelerating convergence such that it is achieved with the mesh resolution of 400×400.

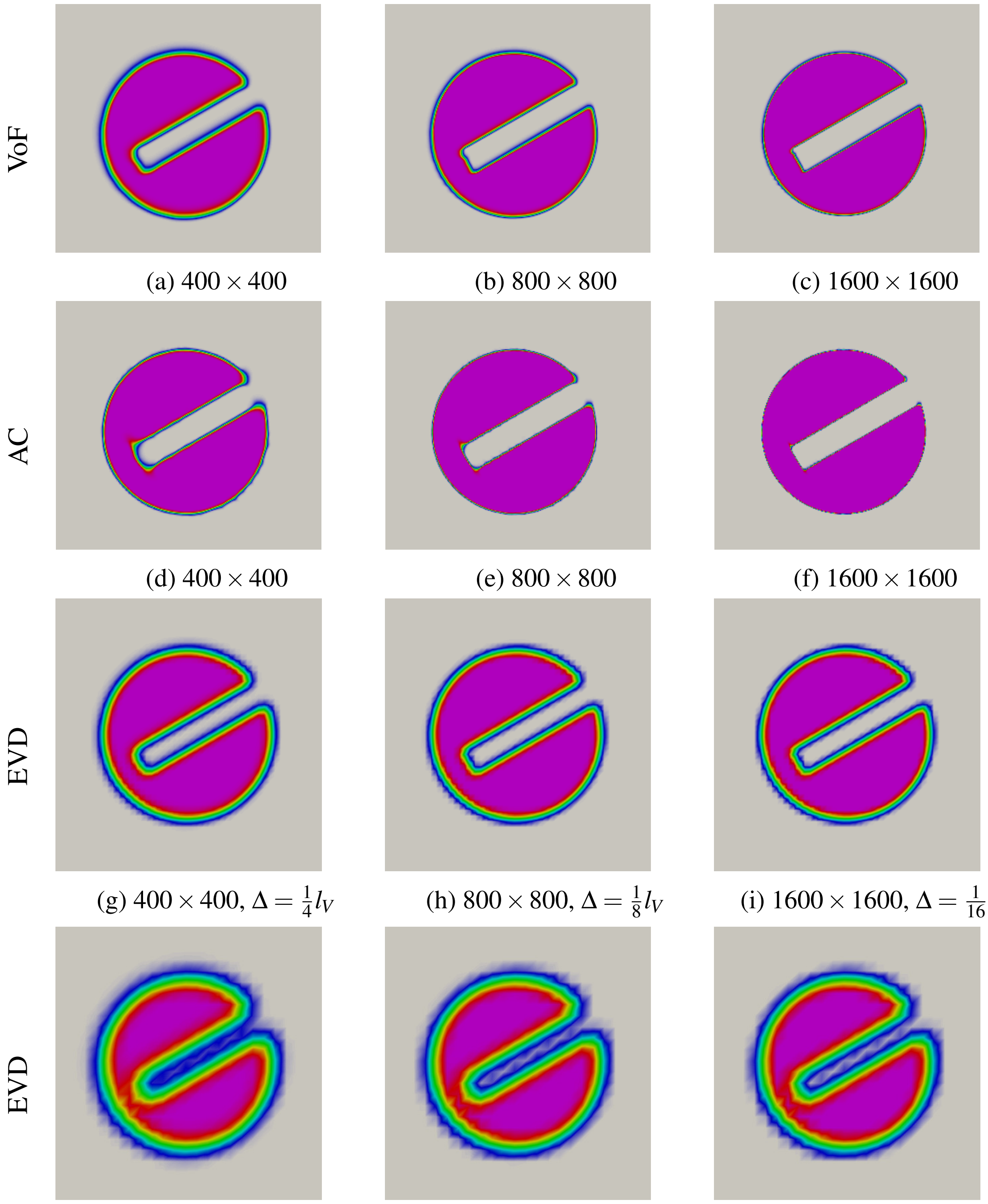

(a) 400×400 (b) 800×800 (c) 1600×1600

(d) 400×400 (e) 800×800 (f) 1600×1600

(g) 400×400, $\Delta = \frac{1}{4} l_V$ (h) 800×800, $\Delta = \frac{1}{8} l_V$ (i) 1600×1600, $\Delta = \frac{1}{16} l_V$

(j) 200×200, $\Delta = \frac{1}{4} l_V$ (k) 400×400, $\Delta = \frac{1}{8} l_V$ (l) 800×800, $\Delta = \frac{1}{16} l_V$

Fig. 5.1 Volume fraction fields after one third rotation of the disc.

5.3 Experimental set-up and data selection for validation

The numerical computations are performed for two air-blast acetone spray jets (designated N-AS2 and N-AS8) that have been investigated experimentally on the Sydney needle spray

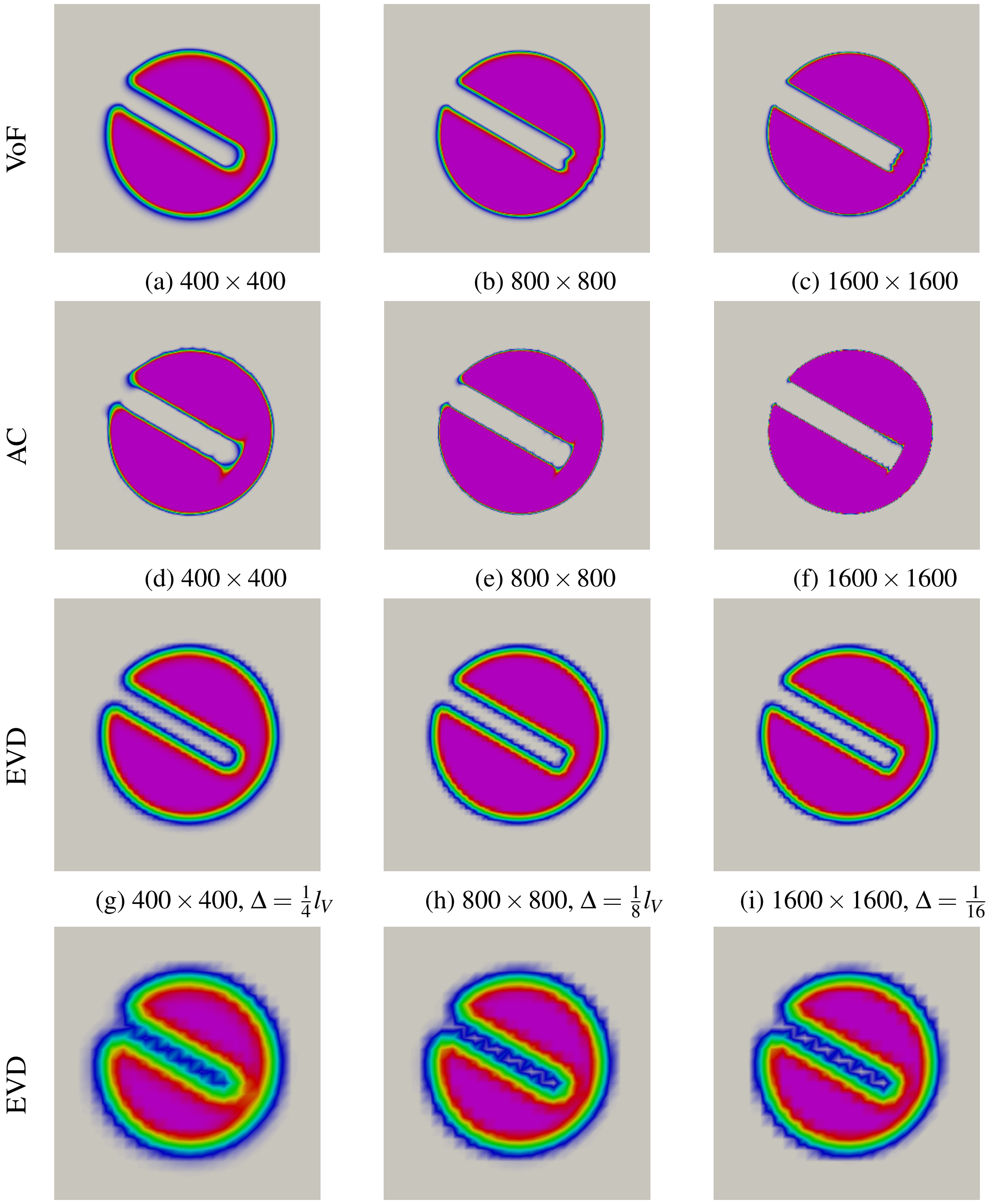

(a) 400×400 (b) 800×800 (c) 1600×1600

(d) 400×400 (e) 800×800 (f) 1600×1600

(g) 400×400, $\Delta = \frac{1}{4} l_V$ (h) 800×800, $\Delta = \frac{1}{8} l_V$ (i) 1600×1600, $\Delta = \frac{1}{16} l_V$

(j) 200×200, $\Delta = \frac{1}{4} l_V$ (k) 400×400, $\Delta = \frac{1}{8} l_V$ (l) 800×800, $\Delta = \frac{1}{16} l_V$

Fig. 5.2 Volume fraction fields after two third rotation of the disc.

burner [153] which is shown schematically in Fig. 5.4. High-quality experimental data is available for axial profiles of the mean volume fraction, measured by the two-angle backlit imaging method [236].

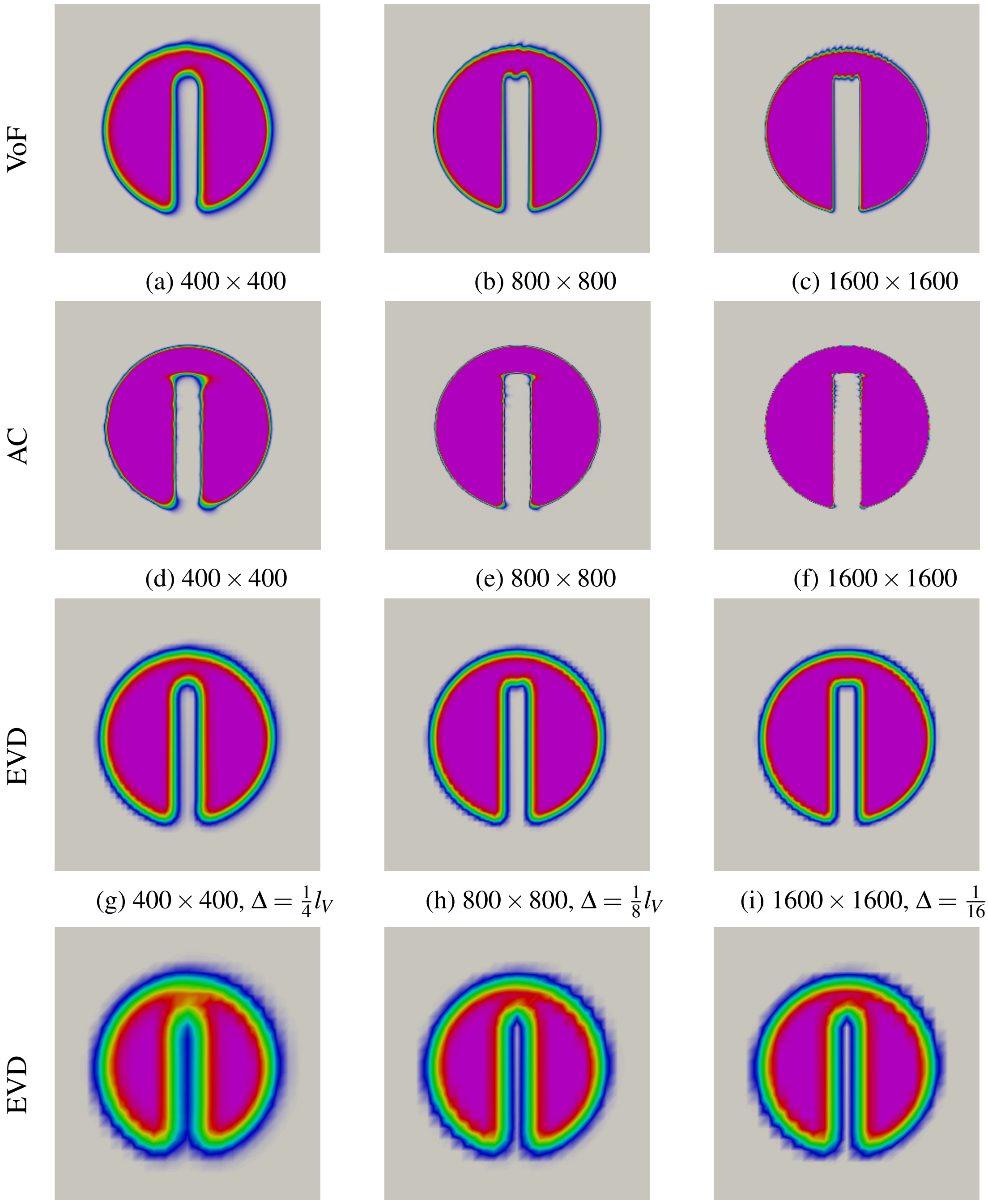

(a) 400×400 (b) 800×800 (c) 1600×1600

(d) 400×400 (e) 800×800 (f) 1600×1600

(g) 400×400, $\Delta = \frac{1}{4} l_V$ (h) 800×800, $\Delta = \frac{1}{8} l_V$ (i) 1600×1600, $\Delta = \frac{1}{16} l_V$

(j) 200×200, $\Delta = \frac{1}{4} l_V$ (k) 400×400, $\Delta = \frac{1}{8} l_V$ (l) 800×800, $\Delta = \frac{1}{16} l_V$

Fig. 5.3 Volume fraction fields after one rotation of the disc.

The burner has concentric liquid, air-blast and pilot streams. The pilot is not modelled in the present study of non-reacting atomization. The acetone is injected from a needle with a diameter of $d_j = 686\mu m$, and the air-blast tube has a diameter of $D = 10mm$. The needle can be recessed below the exit plane of the air-blast tube, but for the N-AS2 and N-AS8 cases,

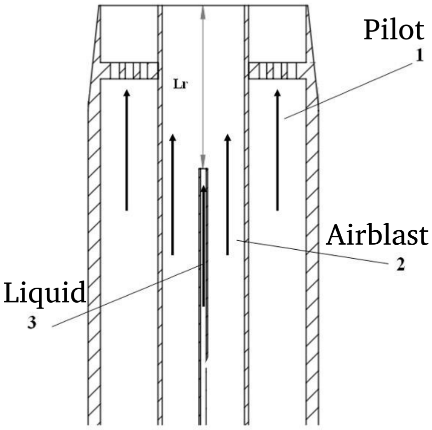

Fig. 5.4 Schematic drawing of the Sydney needle spray burner. Reprinted from Combustion and Flame, Vol 176, A. Lowe, A. Kourmatzis, A.R. Masri, Turbulent spray flames of intermediate density: Stability and near-field structure, Pages 511-520, Copyright (2017), with permission from Elsevier.

the needle and air-blast exit planes are flush. The densities of air and liquid acetone are $\rho_g =$ 1.178kg/m^3 and ρ_l= 784.5kg/m^3 and their kinematic viscosities are ν_g = 1.567e-5m^2/s and ν_l = 3.938e-7m^2/s. The flow parameters for both sprays are given in Table 5.1. The mean burner exit plane velocities in the air-blast and acetone streams are U_g and U_l, respectively, while $Re_g = U_g\left(D-d_j\right)/\nu_g$ and $Re_l = U_l d_j/\nu_l$ are the corresponding Reynolds numbers, and $We = \rho_g\left(U_g-U_l\right)^2 d_j/\sigma$ is the jet Weber number based on the interfacial drift velocity. The surface tension coefficient of the acetone-air interface is specified as 0.023N/m.

Table 5.1 Flow parameters for the N-AS2 and N-AS8 sprays.

Cases	N-AS2	N-AS8
U_g [m/s]	36	48
U_l [m/s]	4.3	2.6
Re_g	21398	28530
Re_l	7491	4529
We	35	72

The computational domain is a three-dimensional cylinder of length $L_x = 50$ mm and diameter $D_{in} = 5$ mm. The mean flow boundary conditions are set according to Table 5.1. A digital filter [134] is used to generate turbulent fluctuations at the liquid and air injection planes. The turbulence intensities of the air-blast in N-AS2 and N-AS8 are $0.11U_g$ and $0.154U_g$, respectively, which are the same as the experimentally observed values. The turbulence intensity for the liquid jet is $0.0525U_l$, which is a characteristic value for turbulent

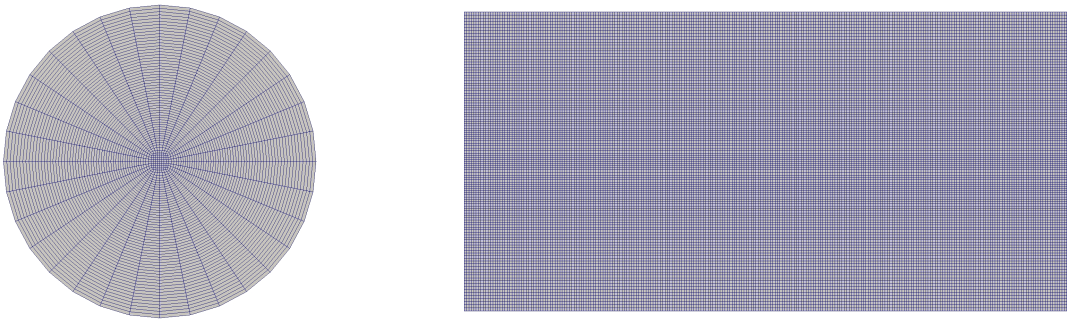

(a) Axial view

(b) Side view

Fig. 5.5 Axial and side views of the mesh scheme at the corresponding cross areas of the computational domain.

pipe flow (experimental data is unavailable). The integral length scales are prescribed as $0.125d_j$ and $0.125D$ for the liquid and air-blast flows, respectively. Note that the air-blast stream diameter in the computations is half the experimental diameter to reduce cost. However, to ensure that the atomization modelling is not unduly affected, the integral length scale in the simulations is based on the experimental air-blast diameter. Three LES meshes are used for testing numerical convergence while the explicit volume length scale, l_v, is kept constant. The liquid jet diameter is resolved by 14, 18 and 24 cells, respectively. The annular gap is resolved by 40, 50 and 62 cells, respectively, and the expansion ratio of the largest and smallest cell size is 1.5. This results in characteristic cell widths near the most important interface region being 49 μm, 38 μm and 30 μm. The domain length in the axial direction is discretized by 1000, 1250 and 1575 cells, respectively, that satisfy the cell lengths in the axial direction almost the same as the characteristic cell widths near the interface region. This grid scheme leads to three LES meshes containing 1.1, 2.3 and 4.5 million cells, respectively. The schematic of the mesh with 2.3 million cells depicting the mesh resolutions is shown in Fig. 5.5.

The explicit volume length scale for EVD cases used for the numerical convergence studies is $l_V = 190$ μm, which is commensurate with the experimentally estimated boundary layer thickness on the gas side of the interface, which are 168 μm and 198 μm, respectively. The empirical correlation for the boundary layer thickness is given by $\delta = 74hRe_g^{-3/4}$ where h is the annular gap thickness of the gas jet [162]. With these settings, the LES to explicit volume size ratios are $\Delta/l_V = 0.263$, 0.206 and 0.164 for the 1.1, 2.3 and 4.5 million cell LES grids, respectively. Based on the findings by Wang et al. [270], these values of Δ/l_V are expected to obtain sufficiently large explicit volume diffusion, which overwhelms the numerical diffusion of VoF such that numerical convergence can be achieved. For sensitivity analysis of variations in explicit length scale, two more values $l_V = 120$ μm (with LES to explicit volume size ratios are 0.449, 0.352 and 0.281 for the 1.1, 2.3 and 4.5 million cell LES grids, respectively) and $l_V = 320\ \mu$m (with LES to explicit volume size ratios are 0.154, 0.120 and 0.096 for the 1.1, 2.3 and 4.5 million cell LES grids, respectively) are used.

Twenty three simulations are performed in total, as set out in Table 5.2. They are named according to the model, the number of LES cells and the spray case. For example, TFVoF1.1L is for the turbulence filtered VoF model with 1.1 million cells applied to the low Weber number spray (N-AS2 with $We = 35$). EVD2.3H is for the explicit volume diffusion model with 2.3 million cells applied to the high Weber number spray (N-AS8 with $We = 72$). EVD cases that are listed with an asterisk, e.g. *EVD1.1L, use the simple surface tension model as implemented by Eq. (5.3) that neglects sub-grid fluctuations. The same simple surface tension model is used in the TFVoF and TF-AC simulations, allowing for a direct comparison of the numerical convergence of the three models. The additional EVD cases named without an asterisk use the complete EVD model with the volume averaged surface tension closure following Wang et al. [270] given by Eq. (4.73). Furthermore, EVD, TFVoF and TF-AC cases listed with double asterisk, e.g. **EVD2.3L,**TFVoF2.3L and **TF-AC2.3L, are simulated by using the Shirani et al. [232] sub-grid surface tension closure as implemented by Eqs. (4.99) and (4.98), respectively.

5.4 Results

A detailed investigation of the grid sensitivity for the three different LES models is presented first in this section. Comparisons are also made to the limited amount of available experimental data. Results are first presented for the TFVoF, TF-AC and EVD models applied to the lower Weber number cases. Then the analysis is made to study the effects of the sub-volume surface tension model for the EVD model, and the findings are compared with the sub-grid closure of Shirani et al. [232]. Moreover, Shirani's closure performance behaviour is also presented for TFVoF and TF-AC formulations. The sensitivity of the EVD solution is tested against three different values of physical volume scales. In the end, performance evaluation of the EVD solution is conducted against the higher Weber number case with and without considering the sub-volume surface tension effects.

5.4.1 Turbulent filtering VoF model (TFVoF)

Figure 5.6 shows instantaneous snapshots of the filtered volume fraction fields on three LES grids for case N-AS2 with the TFVoF model. The amplitude of the wave instability gradually increases along the interface near the nozzle, followed by the break-up of the jet and the

Table 5.2 List of numerical simulations.

TFVoF without sub-grid surface tension Eq. (4.9)	TF-AC without sub-grid surface tension Eq. (4.9)	EVD without sub-grid surface tension Eq. (5.3)
TFVoF1.1L	TF-AC1.1L	*EVD1.1L
TFVoF2.3L	TF-AC2.3L	*EVD2.3L
		*EVD2.3H
TFVoF4.5L	TF-AC4.5L	*EVD4.5L

(a) Numerical simulations for TFVoF, TF-AC and EVD formulations neglecting sub-grid surface tension effects

EVD with sub-grid surface tension Eq. (4.73)
EVD1.1L
EVD2.3L
EVD2.3H
EVD4.5L

(b) Numerical simulations for EVD formulation considering sub-grid surface tension effects following Wang et al. [270]

TFVoF with sub-grid surface tension Eq. (4.98)	TF-AC with sub-grid surface tension Eq. (4.98)	EVD with sub-grid surface tension Eq. (4.99)
**TFVoF2.3L	**TF-AC2.3L	**EVD2.3L

(c) Numerical simulations for formulations considering sub-grid surface tension effects following Shirani et al. [232]

EVD using 1.1M LES cells	EVD using 2.3M LES cells	EVD using 4.5M LES cells
EVD1.1L,$\Delta = 0.154 l_v$	EVD2.3L,$\Delta = 0.120 l_v$	EVD4.5L,$\Delta = 0.096 l_v$
EVD1.1L,$\Delta = 0.263 l_v$	EVD2.3L,$\Delta = 0.206 l_v$	EVD4.5L,$\Delta = 0.164 l_v$
EVD1.1L,$\Delta = 0.449 l_v$	EVD2.3L,$\Delta = 0.352 l_v$	EVD4.5L,$\Delta = 0.281 l_v$

(d) Numerical simulations for EVD formulation with different physical volume length scales

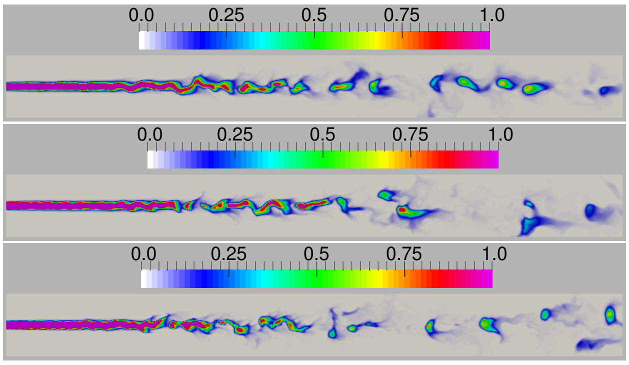

Fig. 5.6 Instantaneous volume fraction fields at the central plane of N-AS2 using the TFVoF model. Top: TFVoF1.1L, Centre: TFVoF2.3L, Bottom: TFVoF4.5L.

evolution of discrete ligaments. With enhanced grid resolution, both numerical diffusion and turbulent diffusion due to filtering are reduced, and it can be seen that the interface is less diffuse; this is especially apparent around the break-up location. It seems the appearance of a discrete liquid structure arises further upstream for finer grids, which can be attributed to two reasons. Firstly, a larger portion of the large eddies, which play a key role in the growth of interface instabilities, is resolved. Secondly, sub-grid fluctuations are neglected in evaluating the filtered surface tension force; that force increases with grid refinement and promotes earlier jet break-up.

The mean and rms of volume fraction in the axial and radial directions are shown in Fig. 5.7. The jet breaks up at around $x/D = 1$, and the volume fraction axial profile decays. The decay rate is close to zero downstream of about $x/D = 5$, indicating the termination of the primary break-up region. The numerical results do not converge monotonically with grid refinement. The coarse and fine grids with 1.1M (million) and 4.5M cells, respectively, are in good agreement with each other but underpredict the experimental data. The results for the 2.3M cell case are noticeably better when compared to the experimental measurements. The statistical similarity of the 1.1M and 4.5M results is interesting. As per the discussion of Fig. 5.6, the increase in the resolved surface tension force with 4.5M cells leads to earlier onset of volume fraction intermittency. At the same time, the volume fraction field is less diffuse, especially near the jet break-up location. These two effects appear to counteract each other leading to some agreement between the 1.1M and 4.5M cell cases along the jet axis, and this is retained for the radial distribution at $x/D = 2$ near the break-up location (see Fig. 5.7b) where a similar trend for the three resolutions is observed. Further downstream of the break-up point ($x/D = 4$, Fig. 5.7c), this counter effect weakens, and the close agreement between the radial profiles for the 1.1M and 4.5M cell simulations disappears. The rms of volume fraction do not have a monotonic convergence with grid refinement either. In

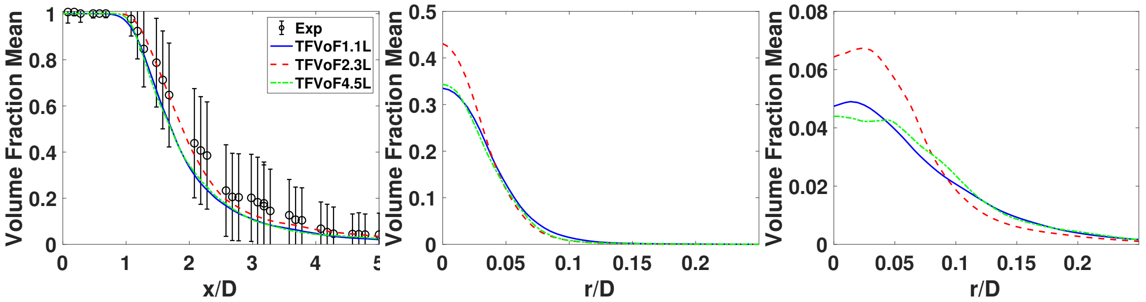

(a) Axial (b) $x/D = 2$ (c) $x/D = 4$

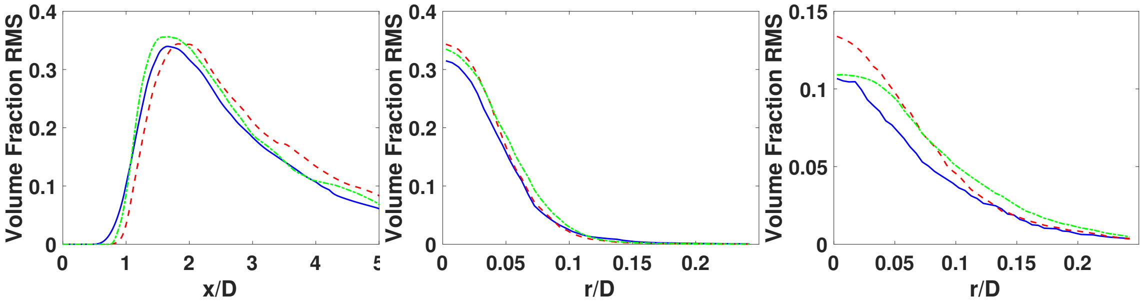

(d) Axial (e) $x/D = 2$ (f) $x/D = 4$

Fig. 5.7 Axial and radial profiles of the mean (1st row) and rms (2nd row) of volume fraction for N-AS2 using the TFVoF model. Radial profiles are shown at two axial stations. Experimental data [236] includes error bars.

Fig. 5.7d, the peak values of rms for the 1.1M and 4.5M cell cases are located at the same axial position, but the peak for the intermediate 2.3M cell case is shifted downstream due to the postponed point of jet break-up.

The axial and radial profiles of mean and rms of the axial component of velocity, U_x, for TFVoF are presented in Fig. 5.8.In contradiction to the volume fraction results, the mean profiles of U_x present a mostly monotonic trend with the refinement of the LES grid, and the results for the intermediate 2.3M cell case and the fine 4.5M cell case are quite close to each other (see Figs. 5.8a-5.8c). However, some visible divergence is evident in the axial centreline profile for $x/D > 3$, where the spray is relatively dilute. The deviation of the mean results in the break-up region ($1 < x/D < 3$) is relatively small. The radial profiles of the mean velocity have somewhat better convergence, but slight differences persist between the 2.3M and 4.5M cell cases. The rms results have similar convergence trends to the mean profiles.

The axial and radial profiles for the mean and rms values of normalized surface density, $\bar{\Sigma}/\bar{\Sigma}_{min}$, are presented in Fig. 5.9. In contradiction to the results of volume fraction mean, $\bar{\Sigma}/\bar{\Sigma}_{min}$ presents a roughly monotonic trend of variation when grids are refined, especially

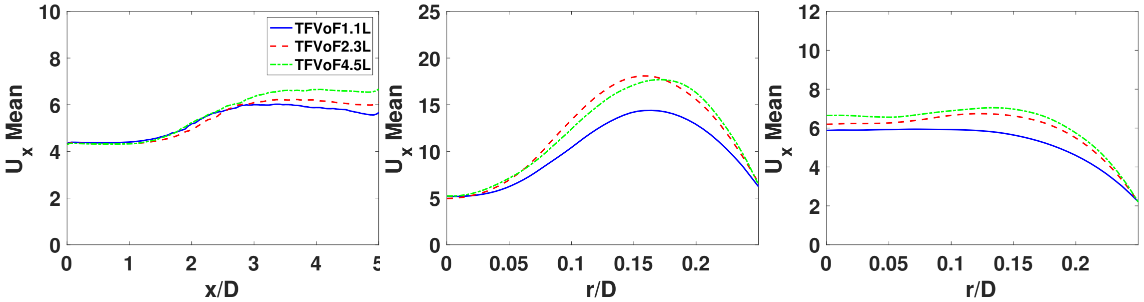

(a) Axial (b) $x/D = 2$ (c) $x/D = 4$

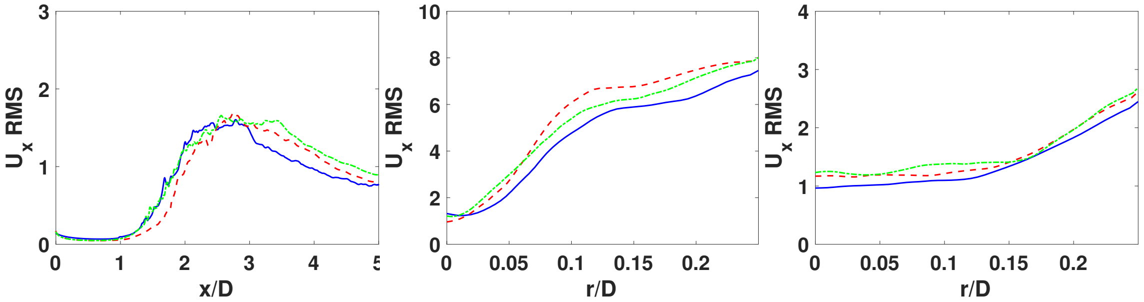

(d) Axial (e) $x/D = 2$ (f) $x/D = 4$

Fig. 5.8 Axial and radial profiles of mean (1st row) and rms (2nd row) of the axial component of velocity for N-AS2 using the TFVoF model. Radial profiles are shown at two axial stations.

for 2.3M and 4.5M. The numerical convergence is highly doubted based on an overall consideration of volume fraction and surface density profiles. In Fig. 5.9a, surface density increases very slowly from the nozzle exit as the surface wave evolves. From the jet break-up point, as determined in Fig. 5.7a, the surface density dramatically increases, and the peak value is located at the position where the highest rms of volume fraction is. Intermittency of the ligaments can be visualized in Fig. 5.6, which gradually grows downstream, leading to a smooth reduction of surface density. In radial directions (see Figs. 5.9b and 5.9c), a peak value is observed that is supposed to be at the radius of the liquid jet. It decreases to the periphery with the same trend as the volume fraction profiles.

Overall, rigorous numerical convergence for TFVoF with the refinement of the LES grid is not established because of the non-monotonic variation in the volume fraction solutions and the inconsistency between the trends for volume fraction, velocity and surface density.

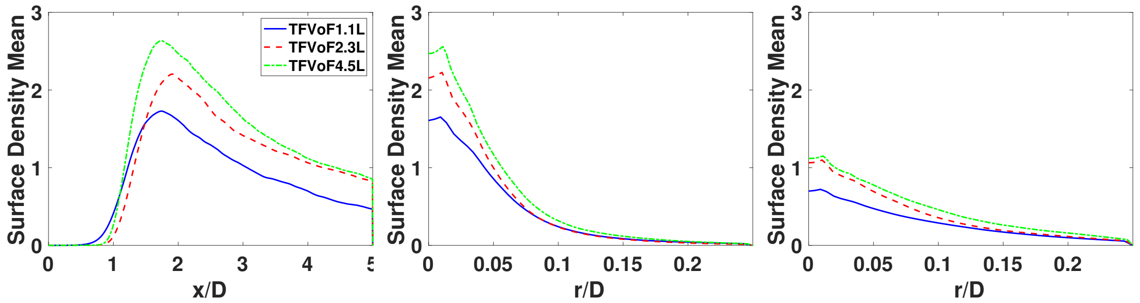

(a) Axial (b) $x/D = 2$ (c) $x/D = 4$

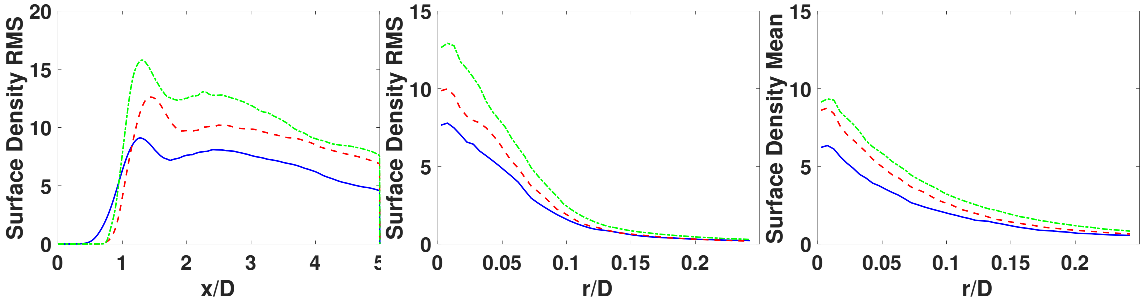

(d) Axial (e) $x/D = 2$ (f) $x/D = 4$

Fig. 5.9 Axial and radial profiles of mean (1st row) and rms (2nd row) of $\bar{\Sigma}/\bar{\Sigma}_{min}$ for N-AS2 using the TFVoF model. Radial profiles are shown at two axial stations.

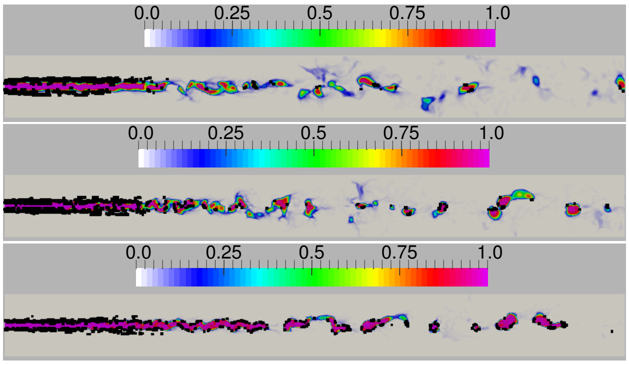

Fig. 5.10 Instantaneous volume fraction fields at the central plane of N-AS2 using the TF-AC model. Top: TF-AC1.1L, Centre: TF-AC2.3L, Bottom: TF-AC4.5L. The black contours indicate the continuous interface region where artificial compression is applied.

5.4.2 Hybrid turbulence filtering and artificial compression model (TF-AC)

Figure 5.10 shows images of the instantaneous volume fraction fields for the TF-AC approach on three LES grids for the N-AS2 spray case. Turbulent diffusion and artificial compression accounting for the sub-filter interface dynamics are switched based on the local value of

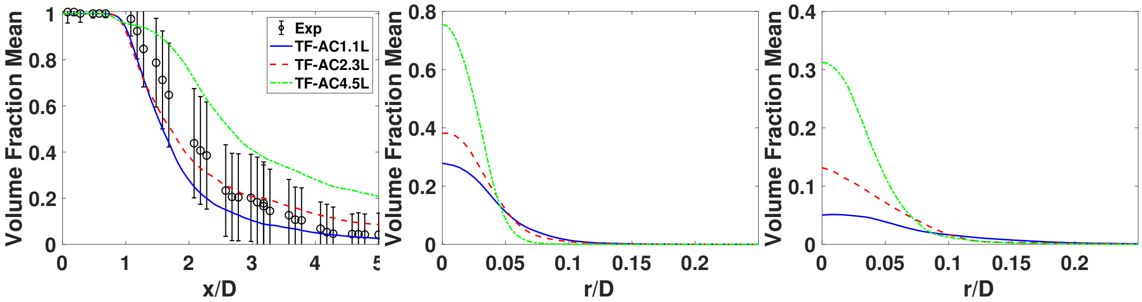

(a) Axial (b) $x/D = 2$ (c) $x/D = 4$

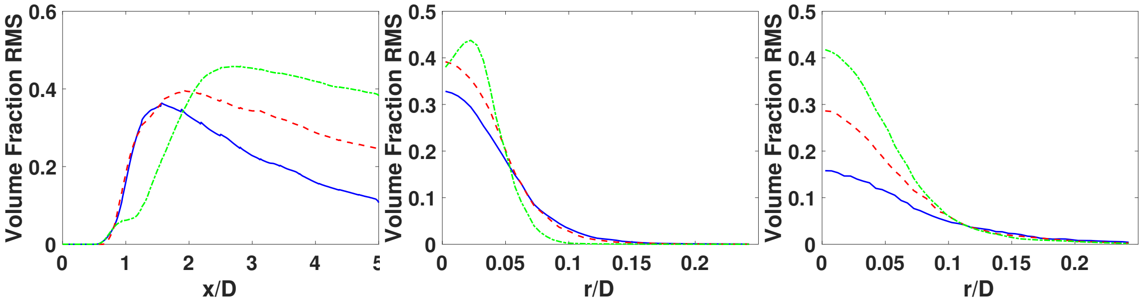

(d) Axial (e) $x/D = 2$ (f) $x/D = 4$

Fig. 5.11 Axial and radial profiles of mean (1st row) and rms (2nd row) of volume fraction for N-AS2 using the TF-AC model. Radial profiles are shown at two axial stations. Experimental data [236] includes error bars.

IRQ_κ (Eq. (4.17)). The black contours represent the continuous interface region where artificial compression is used to sharpen the interface. Elsewhere, turbulent diffusion holds. Along the continuous interface downstream of the injection point, the amplitude of the waves produced by instabilities rises, and a rather abrupt break-up occur for the coarse grid case with 1.1M cells. The interfacial instabilities are restricted to locations further downstream for the 2.3M and 4.5M cell cases which have later break-up points. The continuous interface region is much longer in the 4.5M cell case and persists well downstream of the break-up point on the long ligament structures with quite a sharp volume fraction field compared to the coarse grid results.

Figure 5.11 presents the mean and rms of volume fraction in the axial and radial directions. Figure 5.11a shows that the volume fraction profiles start to decay at the same position for the 1.1M and 2.3M cell cases. Two stages of jet decay can be observed for the refined grid with 4.5M cells. The first stage starts at about the same position that break-up occurs for the other two grids. The similarity of the first break-up points for the three grid resolutions suggests that this process is driven by the combination of inertial and surface tension forces. The second break-up stage for the 4.5M cell grid begins at $x/D = 2$. The rate of volume

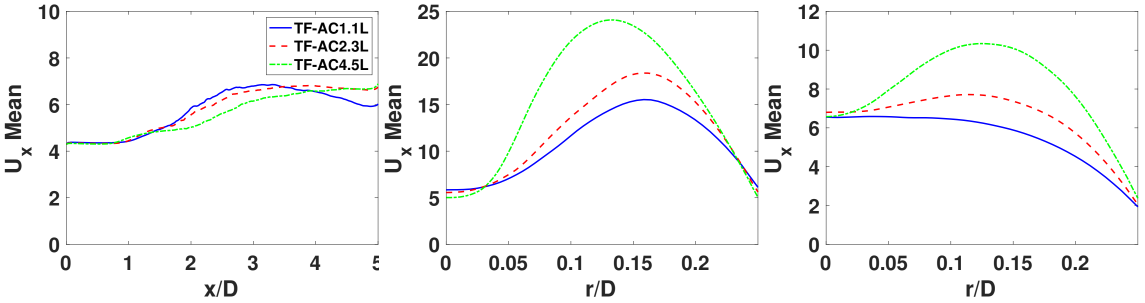

(a) Axial (b) $x/D = 2$ (c) $x/D = 4$

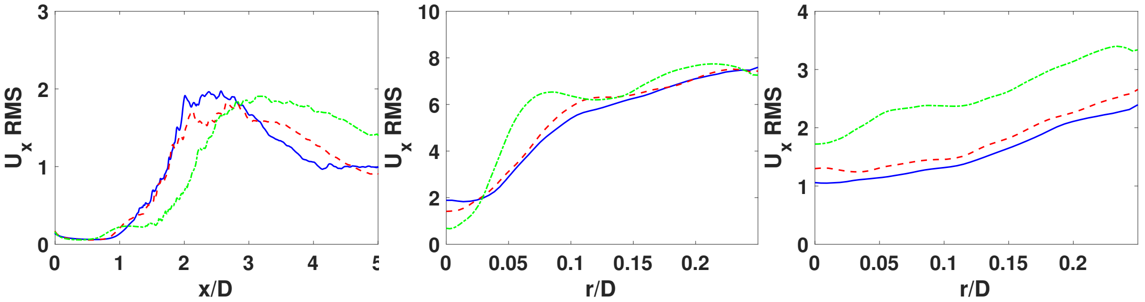

(d) Axial (e) $x/D = 2$ (f) $x/D = 4$

Fig. 5.12 Axial and radial profiles of mean (1st row) and rms (2nd row) of the axial component of velocity for N-AS2 using the TF-AC model. Radial profiles are shown at two axial stations.

fraction decay downstream of the break-up point is very sensitive to the grid resolution, with finer resolution leading to more extended regions of artificial compression along continuous interfaces encompassing a dense jet with less turbulent dispersion (c.f. black contour lines in Fig. 5.10). In combination, artificial compression and the absence of turbulent diffusion along the upstream interface for finer grid TF-AC simulations result in a slower decay rate of the volume fraction. Neither the axial or radial volume fraction profiles in Fig. 5.11 show any sign of convergence with grid refinement.

The mean and rms profiles of U_x are given in Fig. 5.12. Consistent with the volume fraction results, the 1.1M and 2.3M cell cases have a good agreement for $x/D < 2$, but the solutions deviate downstream of that point. The results for the 4.5M cell case are very different, and numerical convergence is not established. The mean and rms profiles of the normalized surface density in axial and radial directions are given in Fig. 5.13. Similar variations from the nozzle to the downstream region and from the jet center to the outer region due to instability growth, jet break-up and intermittency of ligaments can be observed as shown in Fig. 5.9. However, the monotonic shift of the profiles due to grid

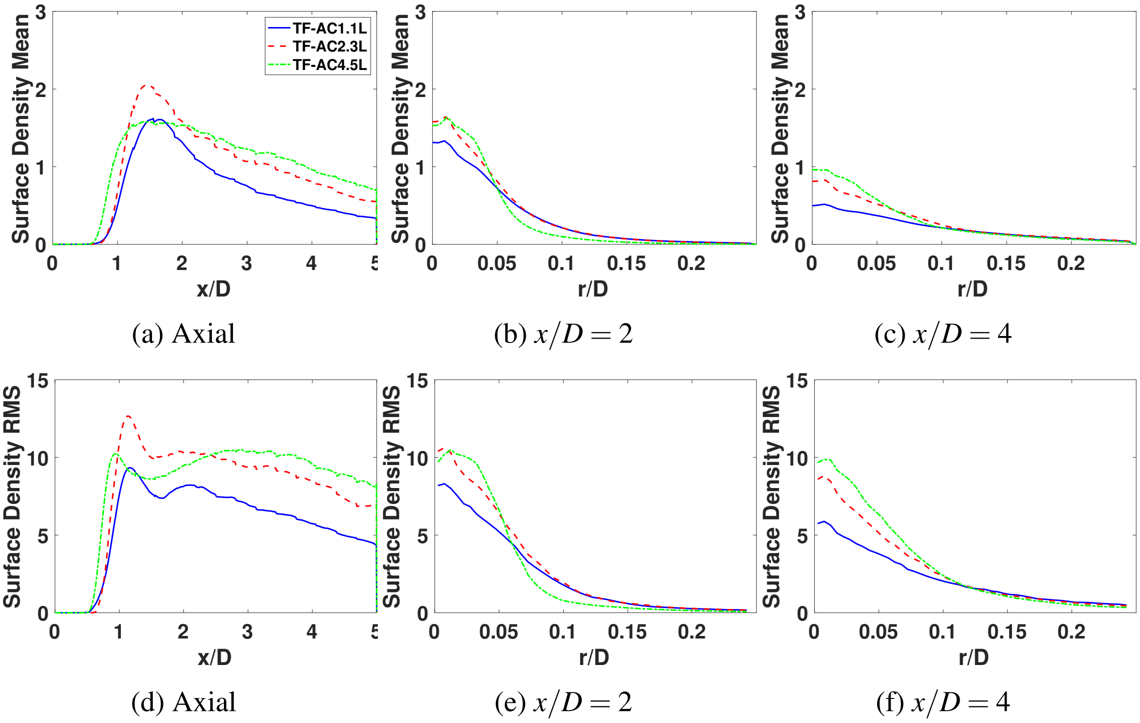

(a) Axial (b) $x/D = 2$ (c) $x/D = 4$

(d) Axial (e) $x/D = 2$ (f) $x/D = 4$

Fig. 5.13 Axial and radial profiles of mean (1st row) and rms (2nd row) of $\bar{\Sigma}/\bar{\Sigma}_{min}$ for N-AS2 using the TF-AC model. Radial profiles are shown at two axial stations.

refinement vanishes. The present results help to explain model performance but the lack of grid convergence for TFVoF and TF-AC lead to some uncertainty.

Although not attempted here, the convergence of the TF-AC model may be possible through varying either C_r in Eq. (4.16) and/or the threshold value of IRQ_κ at which the switch from artificial compression to turbulent diffusion occurs. These parameters are grid-dependent, reducing their usefulness for predictive modelling. Another possibility is to include sub-grid fluctuations in the artificial compression term, replacing the resolved quantity in Eq. (4.15) with a more rigorous model for $\overline{u_r\alpha(1-\alpha)}$.

5.4.3 Explicit volume diffusion (EVD)

The instantaneous volume fraction fields obtained for the EVD model with different grid resolutions are shown in Fig. 5.14 for the N-AS2 spray case. Note that these results are obtained with the simple surface tension closure that neglects sub-volume fluctuations. The fields appear rather diffuse relative to those shown for the TF-AC model, and this behaviour is an expected outcome of volume averaging over an explicitly defined length scale, l_V. The jet break-up location is very similar for all three grids. Further downstream, the ligaments

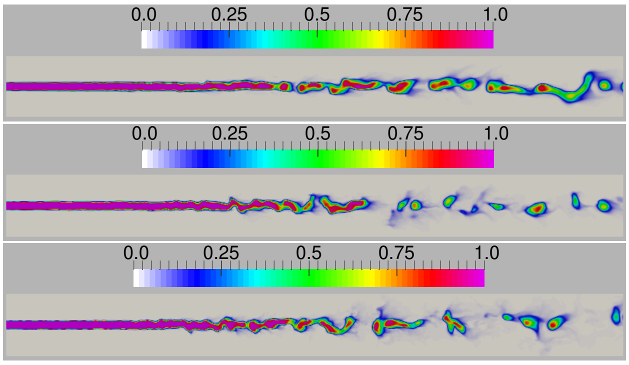

Fig. 5.14 Instantaneous volume fraction fields at the central plane of N-AS2 using the EVD model with the simple surface tension closure that neglects sub-volume fluctuations. Top: *EVD1.1L, Centre: *EVD2.3L, Bottom: *EVD4.5L.

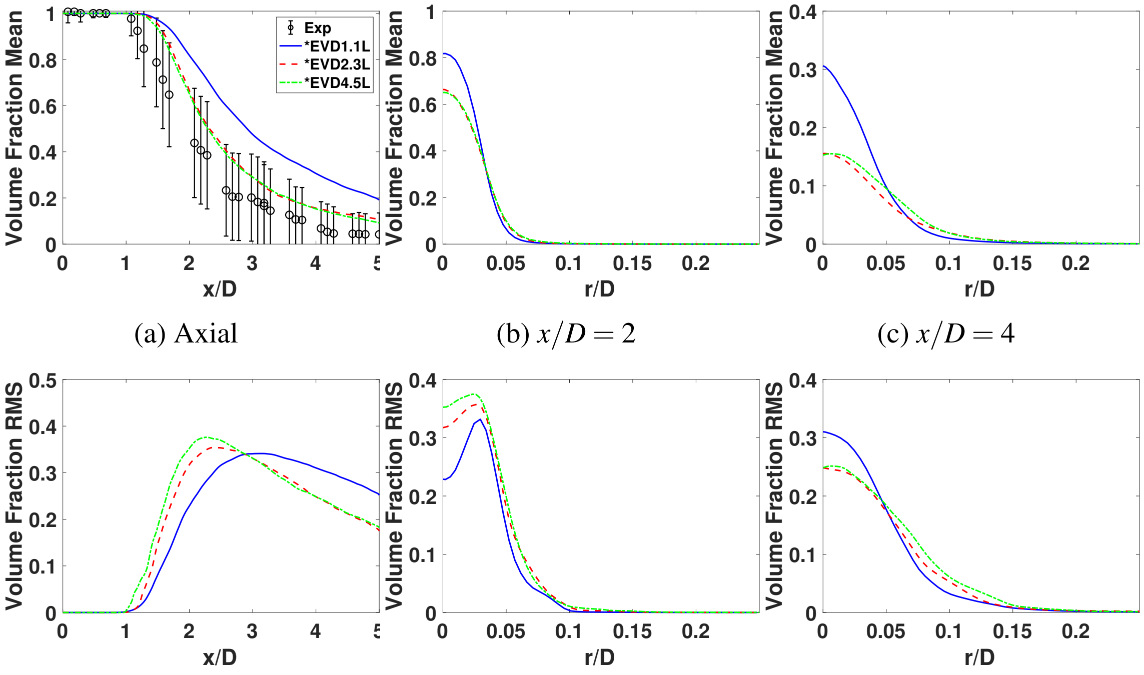

(a) Axial (b) $x/D = 2$ (c) $x/D = 4$

(d) Axial (e) $x/D = 2$ (f) $x/D = 4$

Fig. 5.15 Axial and radial profiles of the mean (1st row) and rms (2nd row) of volume fraction for N-AS2 using the EVD model with the simple surface tension closure that neglects sub-volume fluctuations. Radial profiles are shown at two axial stations. Experimental data [236] includes error bars.

for the 1.1M cell case are more connected than for the two finer grid cases, which appear to be very similar to each other.

Quantitative comparisons are presented in Fig. 5.15, showing axial and radial profiles of the mean and rms of volume fraction. These profiles vary monotonically with increasing grid

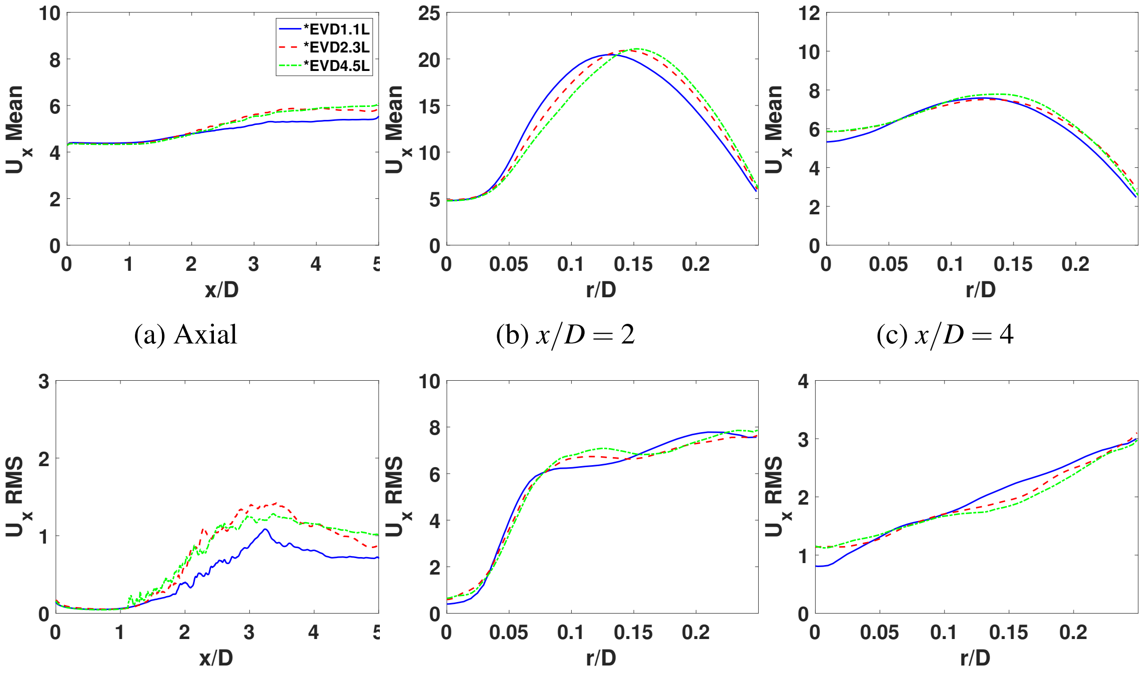

(a) Axial (b) $x/D = 2$ (c) $x/D = 4$

(d) Axial (e) $x/D = 2$ (f) $x/D = 4$

Fig. 5.16 Axial and radial profiles of mean (1st row) and rms (2nd row) of the axial component of velocity for N-AS2 using the EVD model with the simple surface tension closure that neglects sub-volume fluctuations. Radial profiles are shown at two axial stations.

resolution. The 1.1M cell case is not converged, but the mean results for the 2.3M and 4.5M cell cases are in excellent agreement with each other except for some small differences for $r/D < 0.1$ at $x/D = 4$. Similar convergence can be observed for the rms of volume fraction. The grid with 4.5M cells produces slightly higher centreline rms values for $1 < x/D < 2.5$, for $r/D < 0.025$ at $x/D = 2$, and for $r/D > 0.05$ at $x/D = 4$. The numerically converged mean volume fraction profiles along the centreline have a slightly delayed break-up point compared to the data, albeit still within the experimental error margin. The decay rate of the jet downstream of the break-up is well captured. The break-up point is affected by the function $|Q/E|$ in the model for the explicit volume diffusion coefficient in Eq. (4.59). In the upstream region, the interface curvature is close to zero prior to the emergence of interfacial instabilities, and therefore $|Q/E| \to 0$ and $D_V \to 0$. Subsequently, the explicit volume viscosity, ν_V, also approaches zero. This ensures there is no premature dispersion of the interface. In the absence of explicit volume diffusive and viscous transport, the effective turbulent viscosity, ν_t, plays a dominant role in the model sub-volume stress (see Eq. (4.65)) and the growth of initial interfacial instabilities.

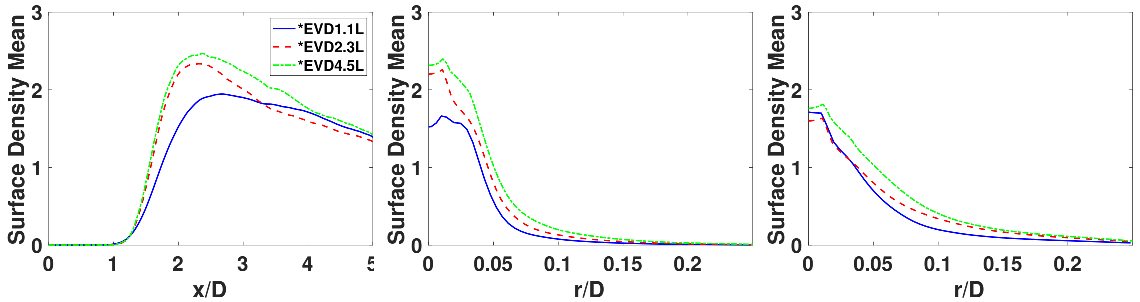

(a) Axial (b) $x/D = 2$ (c) $x/D = 4$

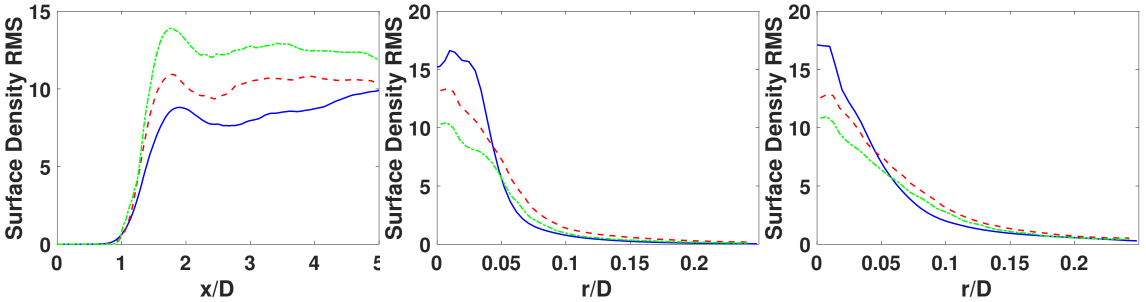

(d) Axial (e) $x/D = 2$ (f) $x/D = 4$

Fig. 5.17 Axial and radial profiles of the mean (1st row) and rms (2nd row) of $\widehat{\Sigma}/\widehat{\Sigma_{min}}$ for N-AS2 using the EVD model with the simple surface tension closure that neglects sub-volume fluctuations. Radial profiles are shown at two axial stations.

The axial and radial profiles of U_x are shown in Fig. 5.16. Consistent with the volume fraction fields, the velocity predictions vary monotonically with grid refinement. The convergence that is evident between the 2.3M and 4.5M grid cell cases is noticeably stronger than the velocity results for the TFVoF model shown in Fig. 5.8, and in contrast to those earlier results, the numerical convergence of the EVD velocity fields is consistent with the convergence of the volume fraction.The axial and radial mean of the normalized surface density, $\widehat{\Sigma}/\widehat{\Sigma_{min}}$, is shown in Fig. 5.17. The same evolution as the other two approaches is not repeated. The solutions shift in a monotonic direction by refining grids and are consistent with the volume fraction profiles. The convergence between 2.3M and 4.5M is better than the results for TFVoF, as shown in Fig. 5.9a.

Overall, the EVD model has superior numerical convergence compared to the TFVoF and TF-AC models. The main reason is that explicit volume diffusion and viscosity coefficients are defined relative to the physical length scale and independent of the LES cell size. The 2.3M cells case, which is numerically converged here, has $\Delta/l_V = 0.2$, which appears to be a sufficient level of grid resolution such that explicit volume diffusion overwhelms both the numerical diffusion and the uncertainty induced by the simple surface tension model. The 2.3M LES grid cell resolution is used as a base case to analyze sub-grid surface tension force.

5.4.4 Richardson Extrapolation analysis

Richardson Extrapolation is a quantitative approach for judging grid convergence of numerical simulations [189, 212, 39]. For three grids with corresponding cell sizes at a local position of $\Delta_1 < \Delta_2 < \Delta_3$, the grid refinement ratios are defined as $r_{21} = \Delta_2/\Delta_1$ and $r_{32} = \Delta_3/\Delta_2$. In the present study, the grid refined ratios are $r_{21} \cong r_{32} = 1.32$ and are approximately uniform across the entire domain. The Richardson Extrapolation relations are presented here for a general flow variable, ϕ, and in the results below, it is applied to the temporally averaged mean of volume fraction and the axial component of velocity for which statistics have been presented already in Sections 5.4.1-5.4.3). For $r_{21} \cong r_{32}$, the apparent local order of the numerical method can be defined as [189, 212]

$$p = \min\left[\max\left(\frac{1}{\ln(r_{21})}\ln\left|\frac{\phi_{32}}{\phi_{21}}\right|, 0.5\right), O(n)\right], \tag{5.4}$$

where $\phi_{32} = \phi_3 - \phi_2$ and $\phi_{21} = \phi_2 - \phi_1$. In case of oscillatory variation of ϕ with Δ, the term $\frac{1}{\ln(r_{21})}\ln\left|\frac{\phi_{32}}{\phi_{21}}\right|$ can diminish to a very low value and is suggested to be clipped at 0.5 [189]. Additionally p should be limited by the order of the numerical scheme [212] and here $O(n) = 2$. The extrapolated solution of ϕ is then defined as [212, 39]

$$\phi_{21}^{ext} = \frac{r_{21}^p \phi_1 - \phi_2}{r_{21}^p - 1}. \tag{5.5}$$

For the volume fraction field, the extrapolated values α_{21}^{ext} are bounded by 0 and 1. The grid convergence index (GCI) is commonly used to quantify the uncertainty of grid convergence and is given by [212, 39]

$$GCI_{21} = \frac{1.25\left|\frac{\phi_1 - \phi_2}{\phi_1}\right|}{r_{21}^p - 1}. \tag{5.6}$$

The axial profiles of GCI_{21} for mean volume fraction and the axial component of mean velocity for the three LES models are presented in Fig. 5.18. For the EVD model, the GCI of the volume fraction (see Fig. 5.18a) is very low along the centreline, indicating little expected sensitivity to further refinement of the grid beyond the most refined grid used here, and is highest for TF-AC, with TFVoF having intermediate GCI. These quantitative measures of convergence uncertainty are consistent with the apparent grid sensitivity of the profiles shown in Figs. 5.11a and 5.15a. As seen earlier in Fig. 5.7a the volume fraction for the

TF-VoF model converges non-monotonic with the refinement of the grid. The oscillations of the relative magnitude among the solutions on the three grids vary at different locations corresponding to the undulations of GCI along the flow axis that are evident in Fig. 5.18. It is interesting to note that the axial velocity predicted by the EVD model has a relatively high uncertainty of convergence, approaching 10%, just downstream of the location of jet break-up at $x/D \sim 2$. This small but notable uncertainty is not easily identified in the velocity profiles shown earlier in Fig. 5.16a. Further downstream, the EVD model consistently gives the lowest GCI of the velocity field amongst the three models. Although the GCI value is low for TF-AC near $x/D = 5$, it cannot by itself support a conclusion that the model is well converged because the GCI of volume fraction is very large there. It is apparent that this GCI analysis further demonstrates the superior numerical convergence of the EVD model in comparison to the TFVoF and TF-AC models.

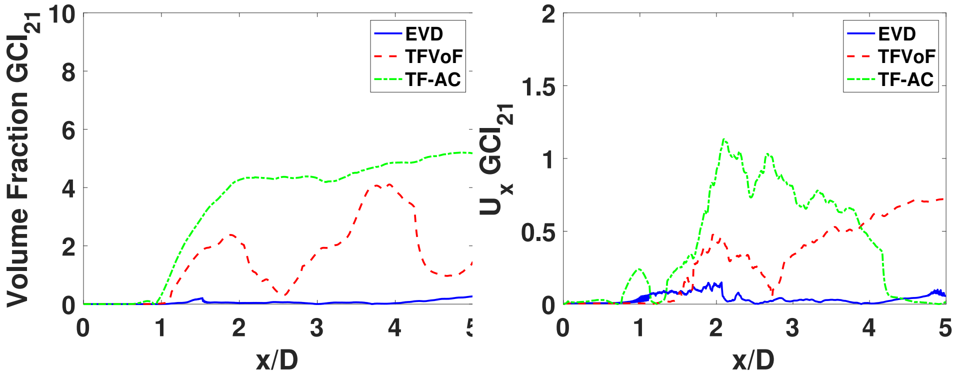

(a) (b)

Fig. 5.18 Axial profiles of the GCI index (GCI_{21}) of volume fraction and the axial component of velocity for the three LES models.

5.4.5 Effects of the sub-grid surface tension

The continuum surface tension model, initially developed by Brackbill et al. [30] has been widely used [230, 94, 47, 184] for LES and DNS of spray atomization with and without considering the sub-grid surface tension effect, but having suitable closure solutions for the sub-grid fluctuations of surface tension is still a challenge. A detailed analysis of the sub-volume closure of Wang et al. [270], termed here as Wang model, and sub-grid closure of Shirani et al. [232], termed here as Shirani model, for the surface tension force is presented here in this Section. Shirani's sub-grid surface tension closure is incorporated here into OpenFOAM for the three differet LES solutions. EVD formulation is tested against both closure models, however, TFVoF and TF-AC solutions are only tested for the solution provided by Shirani et al. [232]. The resulting solutions are compared with those not considering the sub-grid surface tension effects.

Explicit volume diffusion (EVD)

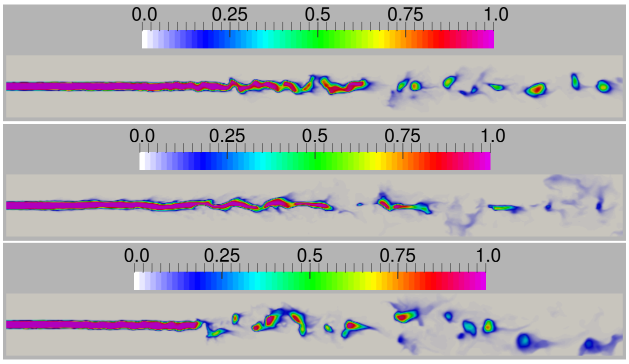

Fig. 5.19 Instantaneous volume fraction fields at the central plane of N-AS2 using the EVD model with the simple surface tension closure given by Eq. (5.3), Wang et al. [270] sub-volume closure given by Eq. (4.73), and Shirani et al. [232] sub-grid closure given by Eq. (4.99) denoted as *EVD2.3L, EVD2.3L and **EVD2.3L, respectively. Top: *EVD2.3L, Middle: EVD2.3L, Bottom: **EVD2.3L.

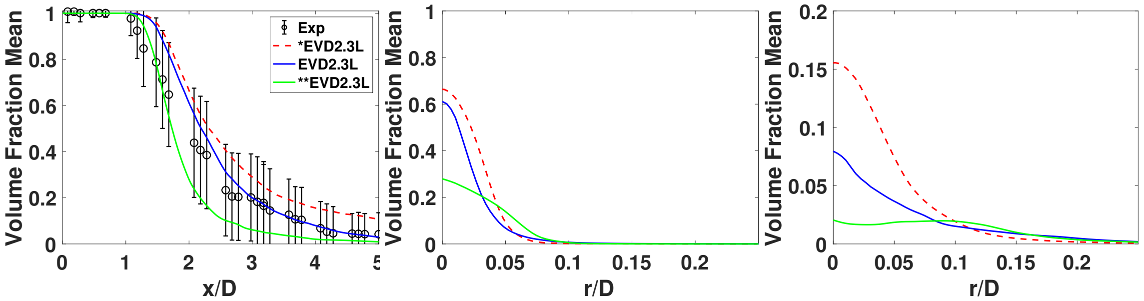

(a) Axial (b) $x/D = 2$ (c) $x/D = 4$

Fig. 5.20 Axial and radial profiles of mean volume fraction for N-AS2 using the EVD model with the simple surface tension closure given by Eq. (5.3), Wang et al. [270] sub-volume closure given by Eq. (4.73), and Shirani et al. [232] sub-grid closure given by Eq. (4.99) denoted as *EVD2.3L, EVD2.3L and **EVD2.3L, respectively. Radial profiles are shown at two axial stations. Experimental data [236] includes error bars.

Figure 5.19 shows instantaneous snapshots of the filtered volume fraction fields for case N-AS2 following the EVD approach in combination with three solutions given by Eqs. (5.3), (4.73) and (4.99) to account for surface tension force. The amplitude of the wave instability

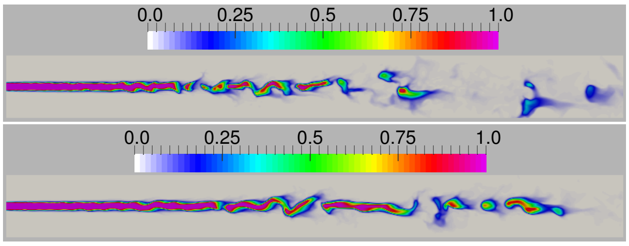

Fig. 5.21 Instantaneous volume fraction fields at the central plane of N-AS2 using the TFVoF model with the simple surface tension closure given by Eq. (4.9) and Shirani et al. [232] sub-grid closure given by Eq. (4.98), denoted as TFVoF2.3L and **TFVoF2.3L, respectively. Top: TFVoF2.3L, Bottom: **TFVoF2.3L.

gradually increases along the interface near the nozzle, followed by the break-up of the jet and the evolution of discrete ligaments. The jet penetration is almost the same for all three solutions, however, the decay rate is faster when the sub-grid effects are considered.

Predictions of the mean volume fraction along the centreline and at two radial locations are shown in Fig. 5.20. The model constant value of $C_{sf} = 1.8$ is used here for the calculations following the Wang model, which was proposed based on a priori analysis of resolved simulations [270]. This also confirms that break-up location is not much sensitive, however, the differences between the models increase further downstream, with the Wang's sub-volume model showing excellent agreement with the data for $x/D > 3$. Shirani's sub-grid solution has shown excellent agreement with the data for $x/D < 1.5$. The prediction of jet break-up and initial decay rate are well aligned with the experimental measurements, however, the much rapid decay rate ,when following Shrani's closure, results in an underprediction of results for the locations $x/D > 1.5$. Overall, Wang's sub-volume closure solution performs better in predicting the realistic surface tension effects both in near-field and far-field regions.

Turbulent filtering VoF model (TFVoF)

Figure 5.21 shows instantaneous snapshots of the filtered volume fraction fields for case N-AS2 following the TFVoF approach in combination with two solutions with and without considering the sub-grid surface tension given by Eqs. (4.98) and (4.9). The amplitude of the wave instability gradually increases along the interface near the nozzle, followed by the break-up of the jet and the evolution of discrete ligaments. The jet penetration is almost the same for both solutions, however, the decay rate is slower when the sub-grid effects are considered. Predictions of the mean volume fraction along the centreline and at two radial locations are shown in Fig. 5.22. These plots also confirm that the break-up location is not sensitive, and the decay rate is significantly reduced when the TFVoF model is coupled with

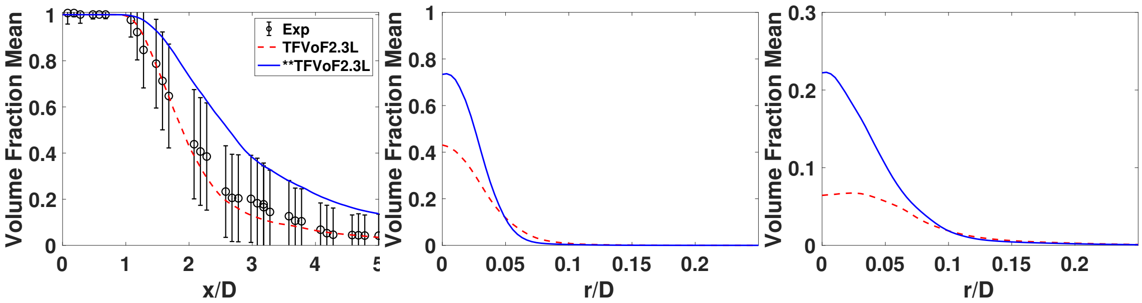

(a) Axial (b) $x/D = 2$ (c) $x/D = 4$

Fig. 5.22 Axial and radial profiles of mean of volume fraction for N-AS2 using the TFVoF model with the simple surface tension closure given by Eq. (4.9) andShirani et al. [232] sub-grid closure given by Eq. (4.98), denoted as TFVoF2.3L and **TFVoF2.3L, respectively. Radial profiles are shown at two axial stations. Experimental data [236] includes error bars.

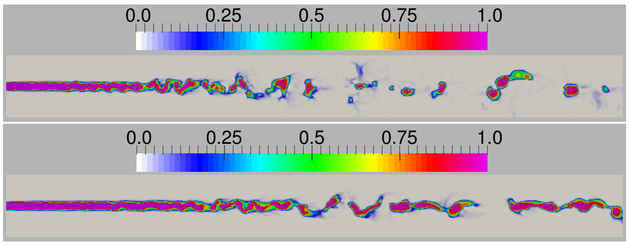

Fig. 5.23 Instantaneous volume fraction fields at the central plane of N-AS2 using the TF-AC model with the simple surface tension closure given by Eq. (4.9) and Shirani et al. [232] sub-grid closure given by Eq. (4.98), denoted as TF-AC2.3L and **TF-AC2.3L, respectively. Top: TF-AC2.3L, Bottom: **TF-AC2.3L.

Shirani's sub-grid solution. This is because of the enhanced sub-grid turbulent diffusion resulting from new surface tension closure coupled with TFVoF formulation.

Hybrid turbulence filtering and artificial compression model (TF-AC)

Figure 5.23 shows instantaneous snapshots of the filtered volume fraction fields for case N-AS2 following the TFVoF approach in combination with two solutions with and without considering the sub-grid surface tension given by Eqs. (4.98) and (4.9). The amplitude of the wave instability gradually increases along the interface near the nozzle, followed by the break-up of the jet and the evolution of discrete ligaments. The jet penetration is almost the same for both solutions, however, the decay rate is much slower when the sub-grid effects are considered. Predictions of the mean volume fraction along the centreline and at two radial locations are shown in Fig. 5.24. These plots also confirm that the break-up location is not much sensitive, and the decay rate is more significantly reduced when the TF-AC model is

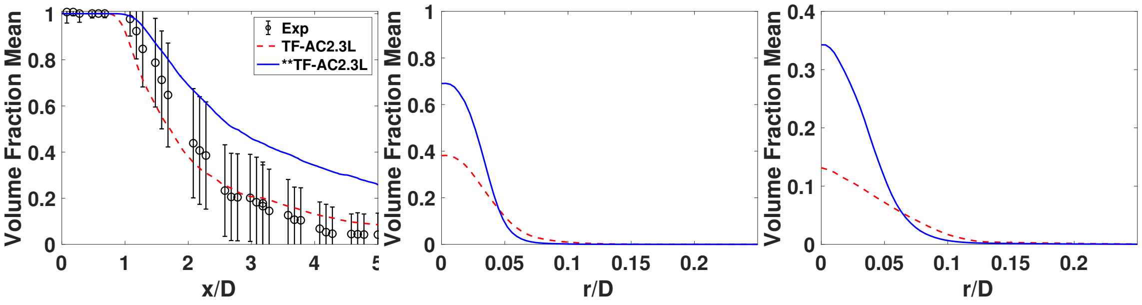

(a) Axial (b) $x/D = 2$ (c) $x/D = 4$

Fig. 5.24 Axial and radial profiles of mean of volume fraction for N-AS2 using the TF-AC model with the simple surface tension closure given by Eq. (4.9) and Shirani et al. [232] sub-grid closure given by Eq. (4.98), denoted as TF-AC2.3L and **TF-AC2.3L, respectively. Radial profiles are shown at two axial stations. Experimental data [236] includes error bars.

coupled with Shirani's sub-grid solution. This is because of the enhanced sub-grid turbulent diffusion resulting from new surface tension closure coupled with TF-AC formulation.

With Shirani's sub-grid closure, the decay rate for TF-AC is slower when compared with TFVoF. However, the trend for both TFVoF and TF-AC is opposite to that of EVD formulation, as in EVD formulation explicit volume diffusion overwhelms the turbulent diffusion and controls the jet decay rate.

5.4.6 Effects of explicit volume length scale (l_v) on EVD solution

To test the sensitivity of EVD to l_v, three different values $112\mu m$, $190\mu m$ and $320\mu m$ are used. Note that this analysis is carried out with Wang's surface tension closure that accounts for the sub-volume fluctuations for the EVD model. Figs. 5.25 and 5.26 present results for simulations with $l_v = 112\mu m$ which is smaller than the boundary layer thickness, $192\mu m$. The jet break-up location is very similar for all three grids, however, further downstream, the ligaments for the 1.1M cell case are more connected than for the two finer grid cases, which appear to be very similar for 2.3M and 4.5M LES cells. Fig. 5.26 shows axial and radial profiles of the mean and rms of volume fraction predictions. Overall, an excellent numerical convergence with grid refinement is observed, and the numerical measurements for the 2.3M and 4.5M cell cases are very close to each other for both the mean and rms fields. The converged axial results are compared with the available experimental data and produce satisfactory predictions of the spray break-up point and the downstream decay of the mean volume fraction. The decay rate predictions are more aligned with experimental findings for the positions of $x/D > 3$.

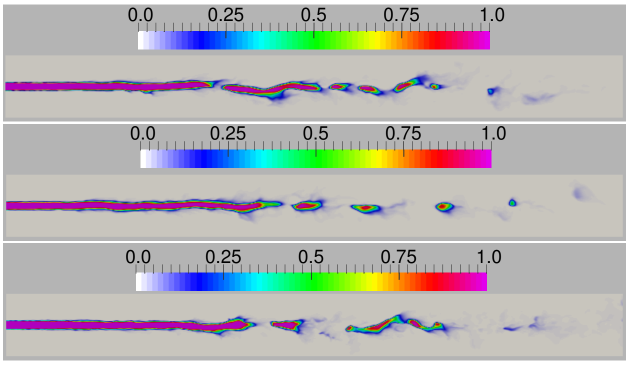

Fig. 5.25 Instantaneous volume fraction fields at the central plane of N-AS2 using the EVD model following Wang et al. [270] sub-volume closure given by Eq. (4.73). The explicit volume length scale is $l_V = 112\mu m$. Top:EVD1.1L,$\Delta = 0.449 l_v$, Centre: EVD2.3L,$\Delta = 0.352 l_v$, Bottom: EVD4.5L,$\Delta = 0.281 l_v$.

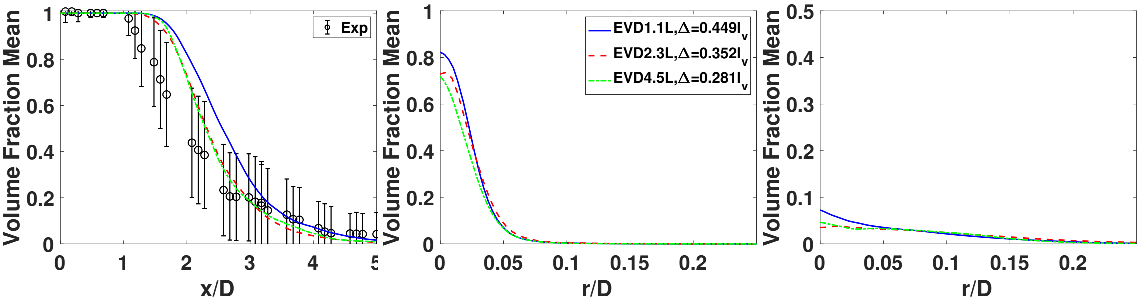

(a) Axial (b) $x/D = 2$ (c) $x/D = 4$

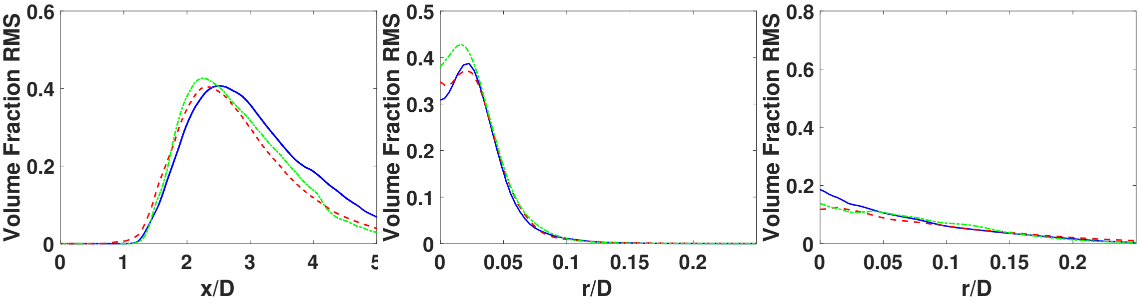

(d) Axial (e) $x/D = 2$ (f) $x/D = 4$

Fig. 5.26 Axial and radial profiles of mean (1st row) and rms (2nd row) of volume fraction for N-AS2 using the EVD model following Wang et al. [270] sub-volume closure given by Eq. (4.73). Radial profiles are shown at two axial stations. Experimental data [236] includes error bars.The explicit volume length scale is $l_V = 112\mu m$.

Figures 5.27 and 5.28 represent the instantaneous volume fraction fields, and mean liquid volume fraction plots of both mean and rms values for the $l_v = 190\mu m$. The decay rate of the volume fraction fields and convergence behaviour for all three LES cells resolutions is

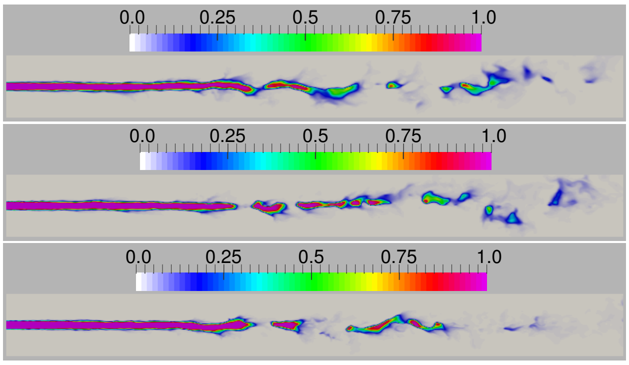

Fig. 5.27 Instantaneous volume fraction fields at the central plane of N-AS2 using the EVD model following Wang et al. [270] sub-volume closure given by Eq. (4.73). The explicit volume length scale is $l_V = 190\mu m$. Top:EVD1.1L,$\Delta = 0.263 l_v$, Centre: EVD2.3L,$\Delta = 0.206 l_v$, Bottom: EVD4.5L,$\Delta = 0.164 l_v$.

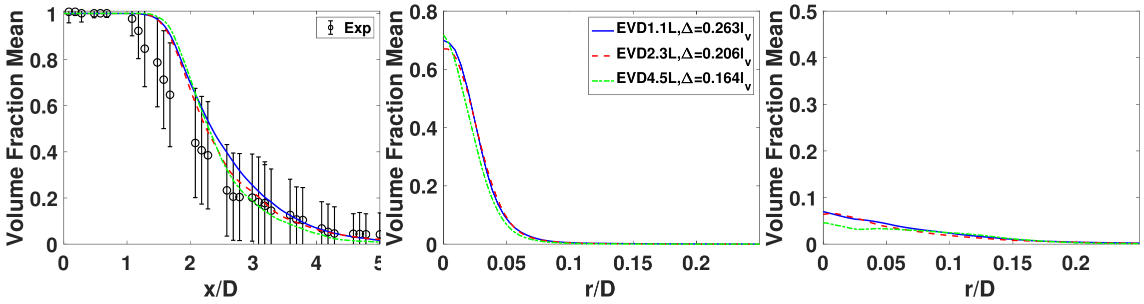

(a) Axial (b) $x/D = 2$ (c) $x/D = 4$

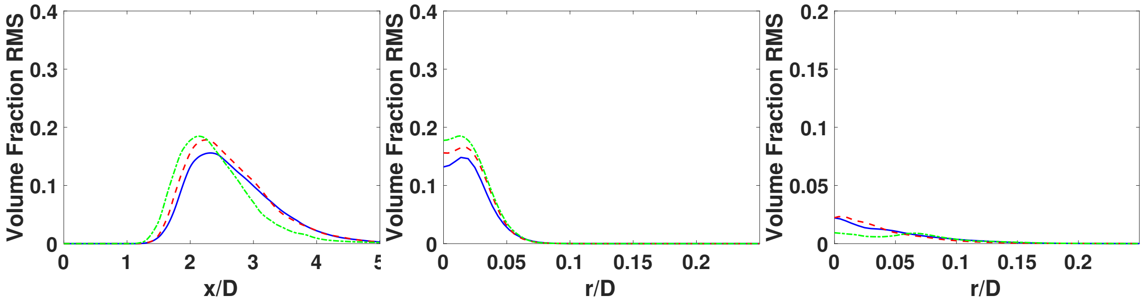

(d) Axial (e) $x/D = 2$ (f) $x/D = 4$

Fig. 5.28 Axial and radial profiles of mean (1st row) and rms (2nd row) of volume fraction for N-AS2 using the EVD model following Wang et al. [270] sub-volume closure given by Eq. (4.73). Radial profiles are shown at two axial stations. Experimental data [236] includes error bars.The explicit volume length scale is $l_V = 190\mu m$.

quite similar to those of the $l_v = 112\mu m$ case, however, the difference between the 1.1M cells and finer resolutions is smaller as the level of explicit volume diffusion is expected to be higher with the increase in explicit volume length scale. Figures 5.29 and 5.30 represent

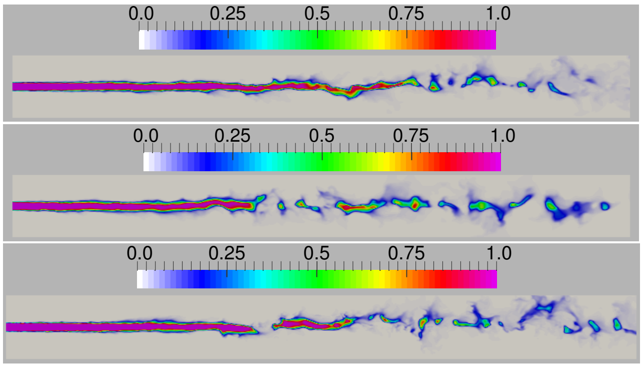

Fig. 5.29 Instantaneous volume fraction fields at the central plane of N-AS2 using the EVD model following Wang et al. [270] sub-volume closure given by Eq. (4.73). The explicit volume length scale is $l_V = 320\mu m$. Top:EVD1.1L,$\Delta = 0.154 l_v$, Centre: EVD2.3L,$\Delta = 0.120 l_v$, Bottom: EVD4.5L,$\Delta = 0.096 l_v$.

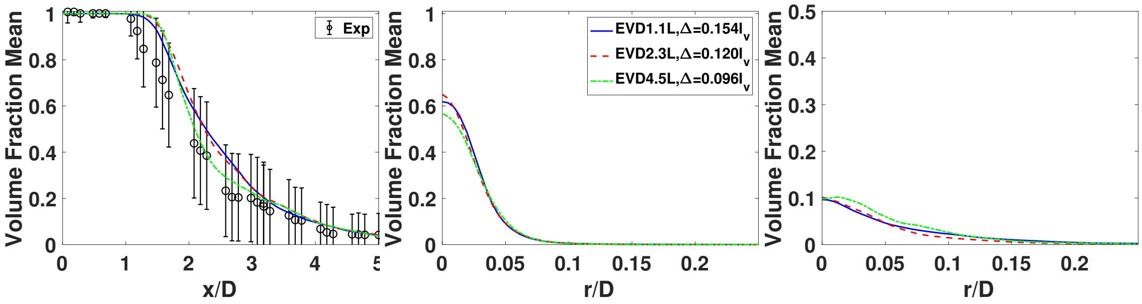

(a) Axial (b) $x/D = 2$ (c) $x/D = 4$

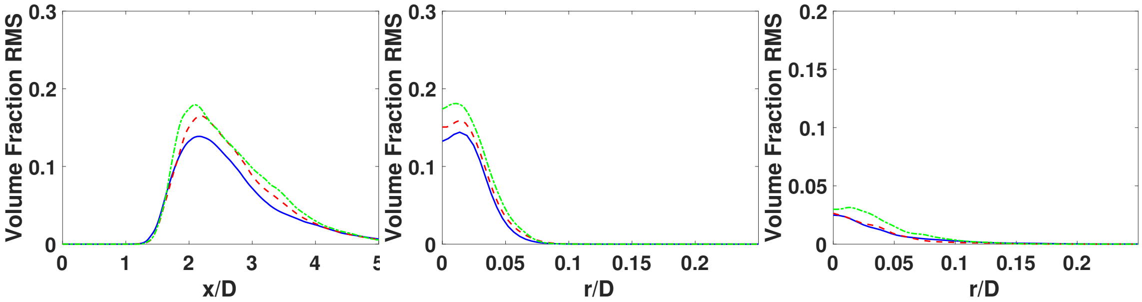

(d) Axial (e) $x/D = 2$ (f) $x/D = 4$

Fig. 5.30 Axial and radial profiles of mean (1st row) and rms (2nd row) of volume fraction for N-AS2 using the EVD model following Wang et al. [270] sub-volume closure given by Eq. (4.73). Radial profiles are shown at two axial stations. Experimental data [236] includes error bars.The explicit volume length scale is $l_V = 320\mu m$.

the instantaneous volume fraction fields, and mean liquid volume fraction plots of both mean and rms values for the $l_v = 320\mu m$. Contrarily, we have observed a different convergence behaviour when the value of l_v is higher than the boundary layer thickness, and profiles for all three resolutions roughly overlap each other. This is because of a higher level of explicit volume diffusion in comparison with the numerical diffusion value. The mean volume fraction plots shown in Fig. 5.30 confirm that the volume fraction decay rate is too fast in the regions of $1.5 < x = D < 2.5$. It is likely that with this much larger value of l_v, the smearing of the interface and boundary layer is excessive, causing the liquid volume fraction to decay too rapidly.

Overall, reasonable convergence is achieved with all three values of l_v compared to TFVoF and TF-AC. However, excellent convergence behaviour is observed for $l_v = 120\mu m$. The convergence for the $l_v = 190\mu m$ case is also reasonable but shows the dominance of explicit volume diffusion over the numerical diffusion for all three resolutions. Upon having a higher value of l_v than the boundary layer thickness (as in the case of $l_v = 320\mu m$), the relative magnitude of numerical diffusion compared with explicit volume diffusion becomes smaller and leads to poor numerical convergence behaviour.

5.4.7 Sensitivity analysis of the model constant, C_{sf}, and application of EVD to the high Weber number case

The sensitivity of the model constant, C_{sf}, is evaluated for both lower Weber number case N-AS2 and higher Weber number case N-AS8. The predictions of the mean volume fraction in the axial direction based on three values of C_{sf} for N-AS2 are shown in Fig. 5.31. Increasing C_{sf} from 1.8 to 3.0 leads to an earlier liquid core break-up and better agreement with the data up to about $x/D = 2$. This is because the surface tension force is increased, leading to an earlier pinch-off of the liquid core as the interfacial instabilities rise. The decay rate of volume fraction downstream of the break-up is similar for all values of C_{sf}. For $x/D > 2$ and

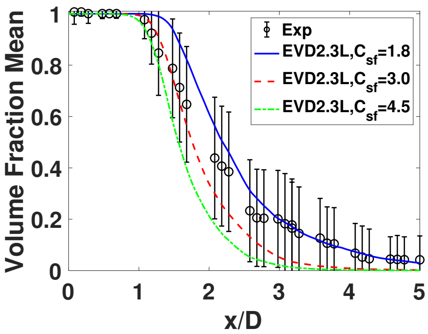

Fig. 5.31 Axial profiles of mean volume fraction for N-AS2 using the EVD model following Wang et al. [270] sub-volume closure given by Eq. (4.73). denoted as EVD2.3L. The EVD2.3L results are for three values of the model constant C_{sf}. Experimental data [236] includes error bars.

the predictions with $C_{sf} = 1.8$ are superior. As C_{sf} is further increased to 4.5, the simulation results approach the lower error margin of experimental data.

The EVD model is now applied to the high Weber number spray case (N-AS8). The predictions of the mean volume fraction in the axial direction based on three values of C_{sf} are shown in Fig. 5.32. Predictions are presented for the EVD model with the simple surface tension closure given by Eq. (5.3) and the EVD model following Wang et al. [270] sub-volume closure given by Eq. (4.73). For the latter, results are provided for three values of the constant, $C_{sf} = 1.8$, $C_{sf} = 3.0$ and $C_{sf} = 4.5$, which are the same as used for N-AS2. When the simple surface tension closure given by Eq. (5.3) is used, the break-up point is predicted very well, but the subsequent decay rate of the jet is overestimated, and the downstream volume fraction is lower than the experimental data and outside the margin of error. Following Wang et al. [270] sub-volume closure given by Eq. (4.73) and model constant value of $C_{sf} = 1.8$, the prediction of the break-up point is much delayed, and the upstream volume fraction values are larger than the data and well outside the margin of error. The decay rate is very similar to the decay rate for the simple surface tension model. Consistent with the findings in Fig. 5.31, further increasing C_{sf} to 3.0 and 4.5 leads to a noticeably earlier break-up compared with $C_{sf} = 1.8$ but does not unduly affect the subsequent decay rate. Overall, the $C_{sf} = 4.5$ result is good and inside the experimental margin of error over most of the length of the atomizing spray.

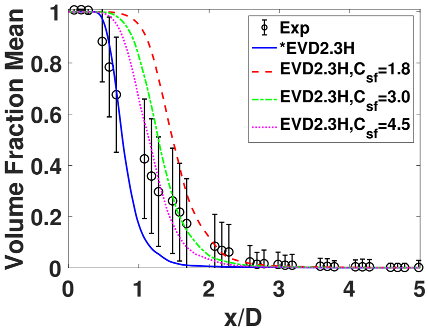

Fig. 5.32 Axial profiles of mean volume fraction for N-AS8 using the EVD model with the simple surface tension closure given by Eq. (5.3) and the EVD model following Wang et al. [270] sub-volume closure given by Eq. (4.73). denoted as *EVD2.3H and EVD2.3H, respectively. The EVD2.3H results are for three values of the model constant C_{sf}. Experimental data [236] includes error bars.

5.5 Summary

A detailed comparison has been conducted of grid sensitivity and accuracy for three VoF-based LES models, including the turbulent filtered VoF model (TFVoF), a hybrid turbulence filtering and artificial compression model (TF-AC), and a new explicit volume diffusion model (EVD). The three approaches are distinguished by different modelling strategies of unresolved fluctuations at the liquid-air interface of a two-phase flow. In general, these fluctuations can be due to interface dynamics and turbulence. TFVoF applies conventional turbulence filtering with a sub-grid turbulent viscosity model to the VoF equations to account for all sub-grid fluctuations. Two significant conceptual shortcomings have been observed. Firstly, the assumption that inertial range turbulent eddies and the energy cascade cross the interface with universal statistical behaviour is not credible. This is particularly relevant in the vicinity of continuous interfaces. Secondly, in regions of low turbulence where turbulent diffusion is small, the numerical solutions are sensitive to artificial diffusion due to the grid. In addition, a couple of other secondary issues may also weaken the numerical convergence of TFVoF. Setting the turbulence filter size to the LES cell size leads to grid dependent value of turbulent viscosity. This is also common with many other LES implementations.

TF-AC attempts to account for more sub-grid interface dynamics by introducing additional artificial compression in the continuous interface region to counteract the numerical diffusion and, thus, sharpen the interface. However, a modelling constant C_r inherent in the artificial compression term is likely to depend on grid resolution. The conventional turbulent viscosity model is only activated in the discrete phase region. A locally evaluated continuous interface indicator, IRQ_κ, defined through the interface curvature, separates the two regions and is likely to be grid dependent. The issues of grid dependent closure of turbulent viscosity and approximated surface tension model mentioned above for the TFVoF model are also inherited into the TF-AC model.

EVD was recently derived based on the concept of averaging the VoF equations over explicitly defined physical volumes [270]. The volume length scale, l_V, is independent of the grid scale and is suggested to be no larger than the boundary layer thickness on the gas side of the liquid-air interface. Sub-volume fluctuations due to inhomogeneous phase fields and mean drift velocity is modelled by a physically derived explicit volume diffusion coefficient and related explicit volume viscosity. The latter is specifically augmented by turbulent viscosity away from the interface. Numerical convergence can be achieved by refining grids while keeping the physical volumes constant so that the explicit volume diffusion overwhelms the numerical diffusion, which reduces as the grid resolution increases. The use of physical length scale based sub-volume closure of surface tension helps to have more realistic predictions of jet decay rate. The analysis also confirms that proper closure for the sub-grid surface tension effects is very important.

A detailed analysis of the sub-volume closure of Wang et al. [270] and sub-grid closure of Shirani et al. [232] for the surface tension force confirms that break-up location is not much sensitive. However, the differences between the models increase further downstream, with the Wang's sub-volume model showing excellent agreement with the data for $x/D > 3$. Shirani's sub-grid solution has shown excellent agreement with the data for $x/D < 1.5$. The prediction of jet break-up and initial decay rate are well aligned with the experimental measurements, however, the much rapid decay rate ,when following Shirani's closure, results in an underprediction of results for the locations $x/D > 1.5$. Overall, Wang's sub-volume closure solution performs better in predicting the realistic surface tension effects both in near-field and far-field regions.

With Shirani's sub-grid surface tension closure, the decay rate for TF-AC is slower when compared with TFVoF. However, the trend for both TFVoF and TF-AC is opposite to that of EVD formulation. The reason behind this is that EVD solution is dominantly controlled by the explicit volume diffusion, which has a physical interpretation, not by the numerical diffusion. However, both TFVoF and TF-AC solutions are dominantly controlled by numerical diffusion. Artificial control of the turbulent diffusion in the case of TF-AC further slow down the decay rate when sub-grid surface tension effects are considered.

Upon analysing the effects of explicit volume length scale (l_v) on EVD solution, reasonable convergence is achieved with all three values of l_v compared to TFVoF and TF-AC. However, excellent convergence behaviour is observed for $l_v = 120\mu m$. The convergence for the $l_v = 190\mu m$ case is also reasonable but shows the dominance of explicit volume diffusion over the numerical diffusion for all three resolutions. Upon having a higher value of l_v than the boundary layer thickness (as in the case of $l_v = 320\mu m$), the relative magnitude of numerical diffusion compared with explicit volume diffusion becomes smaller and leads to poor numerical convergence behaviour.

The performance of EVD model is also evaluated for high Weber number spray case (N-AS8). Results are analysed for three values of the constant, $C_{sf} = 1.8$, $C_{sf} = 3.0$ and $C_{sf} = 4.5$, which are the same as we used for low Weber number spray case (N-AS2). When the simple surface tension closure given by Eq. (5.3) is used, the break-up point is predicted very well, but the subsequent decay rate of the jet is overestimated, and the downstream volume fraction is lower than the experimental data and outside the margin of error. Following Wang et al. [270] sub-volume closure given by Eq. (4.73) and model constant value of $C_{sf} = 1.8$, the prediction of the break-up point is much delayed, and the upstream volume fraction values are larger than the data and well outside the margin of error.

Consistent with the findings for the N-AS2 case, increasing the model constant ,C_{sf}, moves the jet break-up in up stream direction for high Weber number spray case (N-AS8). Overall, the $C_{sf} = 4.5$ result is good and inside the experimental margin of error over most of the length of the atomizing spray. With $C_{sf} = 1.8$, which was proposed based on a priori analysis [270], the data of the jet with $We = 35$ is captured well, but the prediction of the jet break-up with $We = 72$ is much delayed. A higher scaling constant value is needed to achieve optimum results in the high Weber number flow. Further investigation needed to establish suitable mechanism for the selection of scaling constants linked with flow conditions instead of having different values for different Weber number flow conditions. Future work may focus on determining the range of flow conditions for which the surface tension model constants produce good results.

Chapter 6

Conclusions

6.1 Conclusions from the current study

The research work presented in this thesis deals with the development and in-depth investigation of computational tools for modelling interfacial flows, especially in the near-field region. In the past, many approaches were developed to track the interface of a multi-phase/interfacial flow system. Two of them, the volume of fluid (VoF) and the level set (LS), have shown promising findings and have been chosen as a benchmark for further research. VoF methods have been proven viable and flexible solutions that facilitate the tracking of interfacial boundaries with good mass conservation behaviour. Different level of numerical diffusion associated with various grid sizes leads to grid sensitivity issue. Explicit volume diffusion (EVD) based LES modelling solution has shown promising improvements to overcome the shortcomings of two already existing solutions, turbulent filtering VoF model (TFVoF) and hybrid turbulence filtering and artificial compression model (TF-AC). Consideration of sub-grid effects of surface tension force has shown a significant impact on the liquid jet decay rate.

The performance analysis of sub-grid stochastic field PDF-LES solution of Navarro-Martinez [184] against the Sydney needle spray measurements is conducted in Chapter 3. Rigorous numerical convergence for 1.1M LES cells in the combination of increased stochastic fields is not achieved up to 32 stochastic field numbers. As the number of stochastic fields increases, the jet break-up location shifts further downstream. However, reasonable numerical convergence is observed for 2.3M LES cells, and measured values of mean liquid volume fraction and normalized mean surface density for the 16 and 32 stochastic fields are very similar. Overall, very good convergence behaviour can be observed for 4.5M LES cells when measured for the different number of stochastic fields. Here, unlike 1.1M and 2.3M resolution cases, the jet break-up location is less sensitive to the increase in stochastic field numbers. Furthermore, this stochastic field convergence study combined with different mesh resolutions confirms that more stochastic fields are required to achieve a converged solution when a coarser resolution is used. However, convergence can be achieved with fewer stochastic fields for finer mesh resolution. This leads to the conclusion that the stochastic field convergence behaviour depends on the mesh size.

Grid sensitivity is still an issue with the VoF based LES approaches, and the solution is dependent on the LES filter size. The numerical findings of the stochastic fields LES-PDF solution also confirm its grid-dependent behaviour. Using a higher number of stochastic fields in each LES cell has shown some improvements, but the simulation results are still sensitive to LES cell sizes. The main advantage of the sub-grid stochastic field PDF-LES solution is its low computational cost. Calculating filtered moments from a stochastic solution incorporates an error that increases with the increase in sub-grid variance and decreases with the increase in the number of stochastic fields. Increasing the number of stochastic fields leads to more computational time required for the numerical solution [257, 256]. Computational cost limits the maximum number of stochastic fields and LES cell resolution, increasing exponentially with the grid refinement and linearly with the stochastic fields used. Using more stochastic fields permits a better statistical description of the sub-grid structures at a lower computational cost when compared to the cost associated with grid refinement.

Three different LES treatment for unresolved sub-grid fluctuations, including the turbulent filtered VoF model (TFVoF), a hybrid turbulence filtering and artificial compression model (TF-AC), and a new explicit volume diffusion model (EVD), has been analyzed in detail. These approaches are distinguished by different modelling strategies of unresolved fluctuations at the liquid-air interface of a two-phase flow. TFVoF applies conventional turbulence filtering with a sub-grid turbulent viscosity model to the VoF equations to account for all sub-grid fluctuations. Two significant conceptual shortcomings have been observed. Firstly, the assumption that inertial range turbulent eddies and the energy cascade cross the interface with universal statistical behaviour is not credible. This is particularly relevant in the vicinity of continuous interfaces. Secondly, in regions of low turbulence where turbulent diffusion is small, the numerical solutions are sensitive to artificial diffusion due to the grid. Linking the turbulence filter size with LES cell size leads to a grid-dependent value of turbulent viscosity. TF-AC attempts to account for more sub-grid interface dynamics by introducing additional artificial compression in the continuous interface region to counteract the numerical diffusion and thus sharpen the interface. However, a modelling constant C_r inherent in the artificial compression term is likely to depend on grid resolution. The conventional turbulent viscosity model is only activated in the discrete phase region. A locally evaluated continuous interface indicator, IRQ_κ, defined through the interface curvature, separates the two regions, and seems to be grid dependent. The conventional turbulent viscosity model is only activated in the discrete phase region. Additionally, the effects of sub-grid fluctuations of surface tension forces are also neglected in both TFVoF and TF-AC.

The newly developed EVD [270] formulation is based on averaging over explicitly defined physical volumes. The explicit volume length scale, l_V, is independent of the grid scale and should be smaller than the boundary layer thickness on the gas side of the liquid-air interface. The numerical convergence problem can be avoided by refining grids while keeping the physical volumes constant so that the explicit volume diffusion overwhelms the numerical diffusion, which reduces with the refinement of the grid. The EVD model also includes an improved volume averaged surface tension model based on fractal properties of wrinkled sub-volume interfaces. The use of physical length scale based sub-volume closure of surface tension helps to have more realistic predictions of the jet decay rate. The analysis also confirms that proper closure for the sub-grid surface tension effects is very important.

A detailed analysis of the sub-volume closure of Wang et al. [270] and sub-grid closure of Shirani et al. [232] for the surface tension force confirms that break-up location is not much sensitive. However, the differences between the models increase further downstream, with the Wang's sub-volume model showing excellent agreement with the data in the downstream regions. Shirani's sub-grid solution has shown excellent agreement with the data in the upstream region. The prediction of jet break-up and initial decay rate are well aligned with the experimental measurements, however, the much rapid decay rate, when following Shirani's closure, results in an underprediction of results further downstream. Overall, Wang's sub-volume closure solution performs better in predicting the realistic surface tension effects both in near-field and far-field regions. With Shirani's sub-grid surface tension closure, the decay rate for TF-AC is slower when compared with TFVoF. However, the trend for both TFVoF and TF-AC is opposite to that of EVD formulation. The reason behind this is that the EVD solution is dominantly controlled by the explicit volume diffusion, not by the numerical diffusion. However, both TFVoF and TF-AC solutions are dominantly controlled by numerical diffusion. Artificial control of the turbulent diffusion in the case of TF-AC further slows down the decay rate when sub-grid surface tension effects are considered.

Upon analyzing the effects of explicit volume length scale (l_v) on EVD solution, reasonable convergence is achieved with all three values of l_v compared to TFVoF and TF-AC. However, excellent convergence behaviour is observed for $l_v = 120\mu m$. The convergence for the $l_v = 190\mu m$ case is also reasonable but shows the dominance of explicit volume diffusion over the numerical diffusion for all three resolutions. Upon having a higher value of l_v than the boundary layer thickness (as in the case of $l_v = 320\mu m$), the relative magnitude of numerical diffusion compared with explicit volume diffusion becomes smaller and leads to poor numerical convergence behaviour.

The performance of the EVD model is also evaluated for a high Weber number spray case (N-AS8). Results are analyzed for three values of the constant, $C_{sf} = 1.8$, $C_{sf} = 3.0$ and $C_{sf} = 4.5$, which are the same as we used for the low Weber number spray case (N-AS2). When the simple surface tension closure given by Eq. (5.3) is used, the break-up point is predicted very well, but the subsequent decay rate of the jet is overestimated, and the downstream volume fraction is lower than the experimental data and outside the margin of error. Following Wang et al. [270] sub-volume closure given by Eq. (4.73) and model constant value of $C_{sf} = 1.8$, the prediction of the break-up point is much delayed, and the upstream volume fraction values are larger than the experimental data and well outside the margin of error. Consistent with the findings for the N-AS2 case, increasing the model constant, C_{sf}, moves the jet break-up in the upstream direction for the high Weber number spray case (N-AS8). Overall, the $C_{sf} = 4.5$ result is good and inside the experimental margin of error over most of the length of the atomizing spray. With $C_{sf} = 1.8$, which was proposed based on a priori analysis [270], the data of the jet with $We = 35$ is captured well, but the prediction of the jet break-up with $We = 72$ is much delayed. A higher scaling constant value is needed to achieve optimum results in the high Weber number flow.

6.2 Recommendation and future work

Explicit volume diffusion (EVD) solution based on the concept of averaging the VoF equations over explicitly defined physical volumes has shown promising improvements to have the calculations which are grid independent and more reliable. In order to capture better sub-grid interface dynamics, the combination of EVD with either stochastic particle or stochastic field based PDF solution may be a better option. This study confirms that sub-grid/sub-volume surface tension effects are important and reliable sub-models are necessary. EVD based sub-volume surface tension closure helps to have a better prediction of the jet decay rate. However, the solutions are sensitive to the scaling constant. Further investigation is needed to establish a suitable mechanism for the selection of scaling constants linked with flow conditions instead of having different values for different Weber number flows. Future work may focus on determining the range of flow conditions for which the surface tension model constants produce good results.

The recent analysis confirms that the performance of the coupled level set volume of fluid (CLSVOF) method is better than all other available interface-capturing solutions. However, no conclusive findings have been reported regarding grid independence, which is still a big challenge. Furthermore, the computational requirement for CLSVOF based solutions is high, and still not possible to capture the desired statistics for a full scale practical injector. To make these methods practically feasible, there is a need for explicit sub-grid modelling solutions which are grid independent and computationally less expensive. Explicit volume diffusion (EVD) based sub-volume solution for CLSVOF may lead to more realistic predictions applicable to a broader range of flow conditions.

In this study, Shirani's sub-grid/sub-volume closure is investigated for all three TFVoF, TF-AC and EVD formulations. The performance of Shirani's model is satisfactory when the variables are explicitly defined and are not linked with grid resolution. When Shirani's sub-grid closure is coupled with the implicit LES filtered solutions, as in the case of TFVoF and TF-AC, jet decay rate predictions are less realistic. Further improvements are needed to capture more accurate sub-grid surface tension effects for both explicit and implicit formulations.

References

[1] Bp. bp statistical review of world energy 2018. technical report, bp, june 2018. url https://www.bp.com/content/dam/bp/business-sites/en/global/corporate/pdfs/energy-economics/statistical-review/bp-stats-review-2018-full-report.pdf.

[2] International energy agency. world energy outlook. technical report, international energy agency, 2017. url https://www.iea.org/weo/.

[3] U.s. energy information administration. international energy outlook executive summary. technical report, u.s. energy information administration, september 2017.

[4] 4, T. O. F. "openfoam v5 user guide".

[5] Abbas, F., Wang, B., Cleary, M., and Masri, A. (2021). Numerical convergence of volume of fluid based large eddy simulations of atomizing sprays. *Physics of Fluids*, 33(4):042119.

[6] Aboukhedr, M., Gavaises, M., Georgoulas, A., Marengo, M., and Vogiatzaki, K. (2016). Numerical investigation of droplet spreading on porous and non-porous surfaces. In *ILASS Europe–Proceedings of the 23rd Annual Conference on Liquid Atomization and Spray Systems. Brighton, UK*, volume 715.

[7] Aboukhedr, M., Georgoulas, A., Marengo, M., Gavaises, M., and Vogiatzaki, K. (2018). Simulation of micro-flow dynamics at low capillary numbers using adaptive interface compression. *Computers & Fluids*, 165:13–32.

[8] Addessio, F. L., Baumgardner, J. R., Dukowicz, J. K., Johnson, N. L., Kashiwa, B. A., Rauenzahn, R. M., and Zemach, C. (1992). Caveat: A computer code for fluid dynamics problems with large distortion and internal slip. *Unknow*.

[9] Alajbegovic, A. (2001). Large eddy simulation formalism applied to multiphase flows. In *ASME 2001 Fluids Engineering Division Summer Meeting*.

[10] Aliseda, A., Hopfinger, E. J., Lasheras, J. C., Kremer, D., Berchielli, A., and Connolly, E. (2008). Atomization of viscous and non-newtonian liquids by a coaxial, high-speed gas jet. experiments and droplet size modeling. *International Journal of Multiphase Flow*, 34(2):161–175.

[11] Anderson, D. M., McFadden, G. B., and Wheeler, A. A. (1998). Diffuse-interface methods in fluid mechanics. *Annual review of fluid mechanics*, 30(1):139–165.

[12] Anez, J., Ahmed, A., Hecht, N., Duret, B., Reveillon, J., and Demoulin, F. (2019). Eulerian–Lagrangian spray atomization model coupled with interface capturing method for diesel injectors. *International Journal of Multiphase Flow*, 113:325–342.

[13] Arcoumanis, C., Flora, H., Gavaises, M., and Badami, M. (2000). Cavitation in real-size multi-hole diesel injector nozzles. *SAE transactions*, pages 1485–1500.

[14] Ashgriz, N. and Poo, J. (1991). Flair: Flux line-segment model for advection and interface reconstruction. *Journal of computational physics*, 93(2):449–468.

[15] Aulisa, E., Manservisi, S., and Scardovelli, R. (2003). A mixed markers and volume-of-fluid method for the reconstruction and advection of interfaces in two-phase and free-boundary flows. *Journal of Computational Physics*, 188(2):611–639.

[16] Aulisa, E., Manservisi, S., Scardovelli, R., and Zaleski, S. (2007). Interface reconstruction with least-squares fit and split advection in three-dimensional cartesian geometry. *Journal of Computational Physics*, 225(2):2301–2319.

[17] Bachalo, W. (2000). Spray diagnostics for the twenty-first century. *Atomization and Sprays*, 10(3-5):439–474.

[18] Bachalo, W. D., Rudoff, R. C., and Sankar, S. V. (1990). Time-resolved measurements of spray drop size and velocity. In *Liquid Particle Size Measurement Techniques: 2nd Volume*. ASTM International.

[19] Baines, M., Hubbard, M., and Jimack, P. (2011). Velocity-based moving mesh methods for nonlinear partial differential equations. *Communications in Computational Physics*, 10(3):509–576.

[20] Bänsch, E. (1998). *Numerical methods for the instationary Navier-Stokes equations with a free capillary surface*. PhD thesis.

[21] Beau, P., Tanguy, S., Demoulin, F., Berlemont, A., et al. (2005). Primary break-up: DNS of liquid jet to improve atomization modelling. *WIT Transactions on Engineering Sciences*, 50.

[22] Beheshti, N., Burluka, A. A., and Fairweather, M. (2007). Assessment of σ- y liq model predictions for air-assisted atomisation. *Theoretical and Computational Fluid Dynamics*, 21(5):381–397.

[23] Bianchi, G. M., Minelli, F., Scardovelli, R., and Zaleski, S. (2007). 3d large scale simulation of the high-speed liquid jet atomization. *SAE Transactions*, pages 333–346.

[24] Bianchi, G. M., Pelloni, P., Toninel, S., Scardovelli, R., Leboissetier, A., and Zaleski, S. (2005). Improving the knowledge of high-speed liquid jets atomization by using quasi-direct 3d simulation. Technical report, SAE Technical Paper.

[25] Bilger, C., Aboukhedr, M., Vogiatzaki, K., and Cant, R. (2017). Evaluation of two-phase flow solvers using level set and volume of fluid methods. *Journal of Computational Physics*, 345:665–686.

[26] Boeck, T., Li, J., López-Pagés, E., Yecko, P., and Zaleski, S. (2007). Ligament formation in sheared liquid–gas layers. *Theoretical and Computational Fluid Dynamics*, 21(1):59–76.

[27] Boniou, V., Schmitt, T., and Vié, A. (2022). Comparison of interface capturing methods for the simulation of two-phase flow in a unified low-mach framework. *International Journal of Multiphase Flow*, 149:103957.

[28] Boris, J. P. and Book, D. L. (1973). Flux-corrected transport. i. shasta, a fluid transport algorithm that works. *Journal of computational physics*, 11(1):38–69.

[29] Bourlioux, A. (1995). A coupled level-set volume-of-fluid algorithm for tracking material interfaces. In *proceedings of the 6th international symposium on computational fluid dynamics, Lake Tahoe, CA*, volume 15.

[30] Brackbill, J. U., Kothe, D. B., and Zemach, C. (1992). A continuum method for modeling surface tension. *Journal of computational physics*, 100(2):335–354.

[31] Bray, K., Libby, P. A., and Moss, J. (1985). Unified modeling approach for premixed turbulent combustion—part i: General formulation. *Combustion and flame*, 61(1):87–102.

[32] Bulat, G., Jones, W., and Marquis, A. (2013). Large eddy simulation of an industrial gas-turbine combustion chamber using the sub-grid pdf method. *Proceedings of the combustion institute*, 34(2):3155–3164.

[33] Burick, R. (1972). Atomization and mixing characteristics of gas/liquid coaxial injector elements. *Journal of Spacecraft and Rockets*, 9(5):326–331.

[34] Burluka, A., Borghi, R., et al. (2001). Development of a eulerian model for the "atomization" of a liquid jet. *Atomization and sprays*, 11(6).

[35] Callen, H. B. (1985). Thermodynamics and an introduction to thermostatistics 2nd edition, johnwiley & sons.

[36] Candel, S. M. and Poinsot, T. J. (1990). Flame stretch and the balance equation for the flame area. *Combustion Science and Technology*, 70(1-3):1–15.

[37] Canu, R., Duret, B., Reveillon, J., and Demoulin, F.-X. (2020). Curvature-based interface resolution quality (irq) indicator to assess simulation accuracy. *Atomization and Sprays*, 30(1).

[38] Carreau, J.-L., Le Visage, D., Monote, G., Gicquel, P., and Roger, F. (1994). Characterization of the near-injector region of coaxial jets. *Proc. ICLASS-94*, pages 94–101.

[39] Celik, I. B., Ghia, U., Roache, P. J., and Freitas, C. J. (2008). Procedure for estimation and reporting of uncertainty due to discretization in cfd applications. *Journal of fluids Engineering-Transactions of the ASME*, 130(7).

[40] Chan, R. K.-C. (1975). A generalized arbitrary lagrangian-eulerian method for incompressible flows with sharp interfaces. *Journal of Computational Physics*, 17(3):311–331.

[41] Chang, Y.-C., Hou, T., Merriman, B., and Osher, S. (1996). A level set formulation of eulerian interface capturing methods for incompressible fluid flows. *Journal of computational Physics*, 124(2):449–464.

[42] Charlette, F., Meneveau, C., and Veynante, D. (2002). A power-law flame wrinkling model for les of premixed turbulent combustion Part I: non-dynamic formulation and initial tests. *Combustion and Flame*, 131(1-2):159–180.

[43] Chaves, H. and Ludwig, C. (2005). Characterization of cavitation in transparent nozzles depending on the nozzle geometry. In *Proc annu conf inst liq atom spray syst, 18th (ILASS-2005), Orleans, France*, pages 259–4.

[44] Chen, B. and Oevermann, M. (2018). An eulerian stochastic field cavitation model coupled to a pressure based solver. *Computers & Fluids*, 162:1–10.

[45] Chen, T.-F. and Davis, J. R. (1964). Disintegration of a turbulent water jet. *Journal of the Hydraulics Division*, 90(1):175–206.

[46] Chesnel, J. (2010). *Simulation aux Grandes Échelles de l'Atomisation, Application à l'Injection Automobile.* PhD thesis.

[47] Chesnel, J., Reveillon, J., Menard, T., and Demoulin, F.-X. (2011). Large eddy simulation of liquid jet atomization. *Atomization and Sprays*, 21(9).

[48] Chigier, N. (1991). The physics of atomization. plenary lecture. In *Proceedings of the International Conference on Liquid Atomization and Spray Systems, 5th, ICLASS-91, Gaithersburg*, pages 49–64.

[49] Chopp, D. L. (2001). Some improvements of the fast marching method. *SIAM Journal on Scientific Computing*, 23(1):230–244.

[50] Christodoulou, K. and Scriven, L. (1992). Discretization of free surface flows and other moving boundary problems. *Journal of Computational Physics*, 99(1):39–55.

[51] Colagrossi, A. (2005). A meshless lagrangian method for free-surface and interface flows with fragmentation. *These, Universita di Roma.*

[52] Colagrossi, A. and Landrini, M. (2003). Numerical simulation of interfacial flows by smoothed particle hydrodynamics. *Journal of computational physics*, 191(2):448–475.

[53] Colucci, P., Jaberi, F., Givi, P., and Pope, S. (1998). Filtered density function for large eddy simulation of turbulent reacting flows. *Physics of Fluids*, 10(2):499–515.

[54] De Luca, M., Borghi, R., et al. (2009). Pesticide atomization modeling for hollow-cone nozzle. *Atomization and sprays*, 19(8).

[55] De Villiers, E., Gosman, A., and Weller, H. (2004). Large eddy simulation of primary diesel spray atomization. *SAE transactions*, pages 193–206.

[56] DeBar, R. (1974). Fundamentals of the kraken code, lawrence livermore laboratory report. Technical report, Technical Report UCIR-760.

[57] Della Pia, A., Chiatto, M., and de Luca, L. (2020). Global eigenmodes of thin liquid sheets by means of volume-of-fluid simulations. *Physics of Fluids*, 32(8):082112.

[58] Deshpande, S. S., Anumolu, L., and Trujillo, M. F. (2012). Evaluating the performance of the two-phase flow solver interfoam. *Computational science & discovery*, 5(1):014016.

[59] Desjardins, O., McCaslin, J., Owkes, M., and Brady, P. (2013). Direct numerical and large-eddy simulation of primary atomization in complex geometries. *Atomization and Sprays*, 23(11).

[60] Desjardins, O., Moureau, V., and Pitsch, H. (2008). An accurate conservative level set/ghost fluid method for simulating turbulent atomization. *Journal of computational physics*, 227(18):8395–8416.

[61] Ding, H., Spelt, P. D., and Shu, C. (2007). Diffuse interface model for incompressible two-phase flows with large density ratios. *Journal of Computational Physics*, 226(2):2078–2095.

[62] Dodoulas, I. and Navarro-Martinez, S. (2013). Large eddy simulation of premixed turbulent flames using the probability density function approach. *Flow, turbulence and combustion*, 90(3):645–678.

[63] Domann, R. and Hardalupas, Y. (2004). Breakup model for accelerating liquid jets. In *42 nd AIAA Aerospace Sciences Meeting and Exhibit*.

[64] Donea, J., Giuliani, S., and Halleux, J.-P. (1982). An arbitrary lagrangian-eulerian finite element method for transient dynamic fluid-structure interactions. *Computer methods in applied mechanics and engineering*, 33(1-3):689–723.

[65] Druault, P., Lamballais, E., Delville, J., and Bonnet, J.-P. (1999). Development of experiment/simulation interfaces for hybrid turbulent results analysis via the use of dns. In *First Symposium on Turbulence and Shear Flow Phenomena*. Begel House Inc.

[66] du Chéné, A., Min, C., and Gibou, F. (2008). Second-order accurate computation of curvatures in a level set framework using novel high-order reinitialization schemes. *Journal of Scientific Computing*, 35(2):114–131.

[67] Dumond, J., Magagnato, F., and Class, A. (2013). Stochastic-field cavitation model. *Physics of Fluids*, 25(7):073302.

[68] Dumouchel, C. (2008). On the experimental investigation on primary atomization of liquid streams. *Experiments in fluids*, 45(3):371–422.

[69] Duret, B., Reveillon, J., Menard, T., and Demoulin, F. (2013). Improving primary atomization modeling through dns of two-phase flows. *International Journal of Multiphase Flow*, 55:130–137.

[70] Eggers, J. and Villermaux, E. (2008). Physics of liquid jets. *Reports on progress in physics*, 71(3):036601.

[71] Engelbert, C., Hardalupas, Y., and Whitelaw, J. H. (1995). Breakup phenomena in coaxial airblast atomizers. *Proceedings of the Royal Society of London. Series A: Mathematical and Physical Sciences*, 451(1941):189–229.

[72] Enright, D., Fedkiw, R., Ferziger, J., and Mitchell, I. (2002). A hybrid particle level set method for improved interface capturing. *Journal of Computational physics*, 183(1):83–116.

[73] Faeth, G., Hsiang, L.-P., and Wu, P.-K. (1995). Structure and breakup properties of sprays. *International Journal of Multiphase Flow*, 21:99–127.

[74] Fansler, T. D. and Parrish, S. E. (2014). Spray measurement technology: a review. *Measurement Science and Technology*, 26(1):012002.

[75] Fernández, M. A., Gerbeau, J.-F., and Grandmont, C. (2007). A projection semi-implicit scheme for the coupling of an elastic structure with an incompressible fluid. *International Journal for Numerical Methods in Engineering*, 69(4):794–821.

[76] Ferrand, V., Bazile, R., and Boree, J. (2001). Measurements of concentration per size class in a dense polydispersed jet using planar laser-induced fluorescence and phase doppler techniques. *Experiments in fluids*, 31(6):597–607.

[77] Floryan, J. and Rasmussen, H. (1989). Numerical methods for viscous flows with moving boundaries.

[78] Fox, R. O. (2003). *Computational models for turbulent reacting flows*. Cambridge university press.

[79] Francois, M. M., Cummins, S. J., Dendy, E. D., Kothe, D. B., Sicilian, J. M., and Williams, M. W. (2006). A balanced-force algorithm for continuous and sharp interfacial surface tension models within a volume tracking framework. *Journal of Computational Physics*, 213(1):141–173.

[80] Funada, T., Joseph, D., and Yamashita, S. (2004). Stability of a liquid jet into incompressible gases and liquids. *International journal of multiphase flow*, 30(11):1279–1310.

[81] Fuster, D., Bagué, A., Boeck, T., Le Moyne, L., Leboissetier, A., Popinet, S., Ray, P., Scardovelli, R., and Zaleski, S. (2009). Simulation of primary atomization with an octree adaptive mesh refinement and VOF method. *International Journal of Multiphase Flow*, 35(6):550–565.

[82] Gao, F. and O'Brien, E. E. (1993). A large-eddy simulation scheme for turbulent reacting flows. *Physics of Fluids A: Fluid Dynamics*, 5(6):1282–1284.

[83] Georgoulas, A., Koukouvinis, P., Gavaises, M., and Marengo, M. (2015). Numerical investigation of quasi-static bubble growth and detachment from submerged orifices in isothermal liquid pools: The effect of varying fluid properties and gravity levels. *International Journal of Multiphase Flow*, 74:59–78.

[84] Gibou, F., Chen, L., Nguyen, D., and Banerjee, S. (2007). A level set based sharp interface method for the multiphase incompressible navier–stokes equations with phase change. *Journal of Computational Physics*, 222(2):536–555.

[85] Gibou, F., Fedkiw, R., and Osher, S. (2018). A review of level-set methods and some recent applications. *Journal of Computational Physics*, 353:82–109.

[86] Glowinski, R., Le Tallec, P., Ravachol, M., and Tsikkinis, V. (1992). Numerical solution of the navier-stokes equations modeling the flow of two incompressible nonmiscible viscous fluids. *Finite Elements in Fluids. Vol. 8*, 8:137–163.

[87] Gorokhovski, M. and Herrmann, M. (2008). Modeling primary atomization. *Annu. Rev. Fluid Mech.*, 40:343–366.

[88] Gorokhovski, M. and Herrmann, M. (2009). A large eddy simulation subgrid model for turbulent phase interface dynamics. In *11th triennial international annual conference on liquid atomization and spray systems. ICLASS*.

[89] Grandmont, C. and Maday, Y. (2000). Existence for an unsteady fluid-structure interaction problem. *ESAIM: Mathematical Modelling and Numerical Analysis*, 34(3):609–636.

[90] Gueyffier, D., Li, J., Nadim, A., Scardovelli, R., and Zaleski, S. (1999). Volume-of-fluid interface tracking with smoothed surface stress methods for three-dimensional flows. *Journal of Computational physics*, 152(2):423–456.

[91] Guildenbecher, D., López-Rivera, C., and Sojka, P. (2009). Secondary atomization. *Experiments in Fluids*, 46(3):371–402.

[92] Gülder, Ö. L., Smallwood, G. J., and Snelling, D. R. (1992). Diesel spray structure investigation by laser diffraction and sheet illumination. *SAE transactions*, pages 1046–1053.

[93] Harlow, F. H. and Welch, J. E. (1965). Numerical calculation of time-dependent viscous incompressible flow of fluid with free surface. *The physics of fluids*, 8(12):2182–2189.

[94] Hasslberger, J., Ketterl, S., Klein, M., and Chakraborty, N. (2019). Flow topologies in primary atomization of liquid jets: A direct numerical simulation analysis. *Journal of Fluid Mechanics*, 859:819–838.

[95] Hawkes, E. and Cant, R. (2001). Physical and numerical realizability requirements for flame surface density approaches to large-eddy and reynolds averaged simulation of premixed turbulent combustion. *Combustion Theory and Modelling*, 5(4):699.

[96] Haworth, D. C. (2010). Progress in probability density function methods for turbulent reacting flows. *Progress in Energy and Combustion Science*, 36(2):168–259.

[97] Hayashi, M., Hatanaka, K., and Kawahara, M. (1991). Lagrangian finite element method for free surface navier-stokes flow using fractional step methods. *International journal for numerical methods in fluids*, 13(7):805–840.

[98] Hecht, N. (2016). *Simulation aux grandes échelles des écoulements liquide-gaz: application à l'atomisation*. PhD thesis, Rouen, INSA.

[99] Herrmann, M. (2005). Refined level set grid method for tracking interfaces. *annual research briefs*, pages 3–18.

[100] Herrmann, M. (2008a). A balanced force refined level set grid method for two-phase flows on unstructured flow solver grids. *Journal of computational physics*, 227(4):2674–2706.

[101] Herrmann, M. (2008b). Detailed numerical simulations of the primary breakup of turbulent liquid jets. In *Proc. 21st Annual Conf. ILASS-Americas, 2008*.

[102] Herrmann, M. (2011). On simulating primary atomization using the refined level set grid method. *Atomization and Sprays*, 21(4).

[103] Herrmann, M. and Gorokhovski, M. (2009). A large eddy simulation subgrid model for turbulent phase interface dynamics. In *11th International Annual Conference on Liquid Atomization and Spray Systems, ICLASS 2009*. ILASS Americas/Professor Scott Samuelsen UCI Combustion Laboratory ....

[104] Hirt, C. and Cook, J. (1972). Calculating three-dimensional flows around structures and over rough terrain. *Journal of Computational Physics*, 10(2):324–340.

[105] Hirt, C., Cook, J., and Butler, T. (1970). A lagrangian method for calculating the dynamics of an incompressible fluid with free surface. *Journal of Computational Physics*, 5(1):103–124.

[106] Hirt, C. W., Amsden, A. A., and Cook, J. (1974). An arbitrary lagrangian-eulerian computing method for all flow speeds. *Journal of computational physics*, 14(3):227–253.

[107] Hirt, C. W. and Nichols, B. D. (1981). Volume of fluid (VOF) method for the dynamics of free boundaries. *Journal of computational physics*, 39(1):201–225.

[108] Hodges, J., Baritaud, T., and Heinze, T. (1991). Planar liquid and gas fuel and droplet size visualization in a dl diesel engine. *SAE transactions*, pages 1284–1302.

[109] Hoepffner, J., Blumenthal, R., and Zaleski, S. (2011). Self-similar wave produced by local perturbation of the kelvin-helmholtz shear-layer instability. *Physical review letters*, 106(10):104502.

[110] Hong, M. (2003). *Atomisation et mélange dans les jets coaxiaux liquide-gaz*. PhD thesis, Grenoble INPG.

[111] Hong, M., Cartellier, A., and Hopfinger, E. (2002). Atomization and mixing in coaxial injection. In *Proc. 4th Int. Conference on Launcher Technology" Space Launcher Liquid Propulsion", Liege, Belgique*, pages 3–6.

[112] Huang, M., Chen, B., and Wu, L. (2010). A slic–vof method based on unstructured grid. *Microgravity Science and Technology*, 22(3):305–314.

[113] Hunt, J. C., Wray, A. A., and Moin, P. (1988). Eddies, streams, and convergence zones in turbulent flows.

[114] Hyman, J. M. (1984). Numerical methods for tracking interfaces. *Physica D: Nonlinear Phenomena*, 12(1-3):396–407.

[115] Ishii, M. (1975). Thermo-fluid dynamic theory of two-phase flow. *NASA Sti/recon Technical Report A*, 75:29657.

[116] Jamshed, S. (2015). Chapter 4 - High Reynolds Number Flows. In Jamshed, S., editor, *Using HPC for Computational Fluid Dynamics*, pages 81 – 100. Academic Press, Oxford.

[117] Jasak, H. (1996). Error analysis and estimation for the finite volume method with applications to fluid flows.

[118] Jasak, H. (2009). Openfoam: open source cfd in research and industry. *International Journal of Naval Architecture and Ocean Engineering*, 1(2):89–94.

[119] Jasak, H., Jemcov, A., Tukovic, Z., et al. (2007). Openfoam: A c++ library for complex physics simulations. In *International workshop on coupled methods in numerical dynamics*, volume 1000, pages 1–20. IUC Dubrovnik Croatia.

[120] Jasak, H. and Weller, H. (1995). Interface tracking capabilities of the inter-gamma differencing scheme.

[121] Jay, S., Lacas, F., and Candel, S. (2003). Eulerian simulation of coaxial injection using an interfacial surface density balance equation. In *Proc. ICLASS Meeting*.

[122] Jay, S., Lacas, F., and Candel, S. (2006). Combined surface density concepts for dense spray combustion. *Combustion and Flame*, 144(3):558–577.

[123] Jofre, L., Borrell, R., Lehmkuhl, O., and Oliva, A. (2015). Parallel load balancing strategy for volume-of-fluid methods on 3-d unstructured meshes. *Journal of Computational Physics*, 282:269–288.

[124] Jones, W., Lyra, S., and Navarro-Martinez, S. (2012). Numerical investigation of swirling kerosene spray flames using large eddy simulation. *Combustion and Flame*, 159(4):1539–1561.

[125] Jones, W. and Navarro-Martinez, S. (2007). Large eddy simulation of autoignition with a subgrid probability density function method. *Combustion and Flame*, 150(3):170–187.

[126] Jones, W. and Navarro-Martinez, S. (2009). Large eddy simulation and the filtered probability density function method. In *AIP Conference Proceedings*, volume 1190, pages 39–62. American Institute of Physics.

[127] Kang, I. and Leal, L. (1987). Numerical solution of axisymmetric, unsteady free-boundary problems at finite reynolds number. i. finite-difference scheme and its application to the deformation of a bubble in a uniaxial straining flow. *The Physics of fluids*, 30(7):1929–1940.

[128] Kang, M., Fedkiw, R. P., and Liu, X.-D. (2000). A boundary condition capturing method for multiphase incompressible flow. *Journal of Scientific Computing*, 15(3):323–360.

[129] Kataoka, I., Yoshida, K., Naitoh, M., Okada, H., and Morii, T. (2012). Modeling of turbulent transport term of interfacial area concentration in gas–liquid two-phase flow. *Nuclear engineering and design*, 253:322–330.

[130] Ketterl, S., Reißmann, M., and Klein, M. (2019). Large eddy simulation of multiphase flows using the volume of fluid method: Part 2 - A-posteriori analysis of liquid jet atomization. *Experimental and Computational Multiphase Flow*, 1(3):201–211.

[131] Klein, M., Sadiki, A., and Janicka, J. (2000). Direct numerical simulations of plane turbulent jets at moderate reynolds numbers. In *20th IUTAM Congress, ICTAM*.

[132] Klein, M., Sadiki, A., and Janicka, J. (2001a). Influence of the boundary conditions on the direct numerical simulation of a plane turbulent jet. In *Second Symposium on Turbulence and Shear Flow Phenomena*. Begel House Inc.

[133] Klein, M., Sadiki, A., and Janicka, J. (2001b). Influence of the inflow conditions on the direct numerical simulation of primary breakup of liquid jets. *Proc. of ILASS-17-Europe*, 1:475–480.

[134] Klein, M., Sadiki, A., and Janicka, J. (2003). A digital filter based generation of inflow data for spatially developing direct numerical or large eddy simulations. *Journal of computational Physics*, 186(2):652–665.

[135] Klimenko, A. Y. and Bilger, R. W. (1999). Conditional moment closure for turbulent combustion. *Progress in energy and combustion science*, 25(6):595–687.

[136] Kobayashi, H. (2005). The subgrid-scale models based on coherent structures for rotating homogeneous turbulence and turbulent channel flow. *Physics of Fluids*, 17(4):045104.

[137] Kocamustafaogullari, G. and Ishii, M. (1995). Foundation of the interfacial area transport equation and its closure relations. *International Journal of Heat and Mass Transfer*, 38(3):481–493.

[138] Kothe, D., Rider, W., Mosso, S., Brock, J., and Hochstein, J. (1996). Volume tracking of interfaces having surface tension in two and three dimensions. In *34th aerospace sciences meeting and exhibit*, page 859.

[139] Kourmatzis, A., Pham, P. X., and Masri, A. R. (2017). A two-angle far-field microscope imaging technique for spray flows. *Measurement Science and Technology*, 28(3):035302.

[140] Kumar, A. and Sahu, S. (2018). Liquid jet breakup unsteadiness in a coaxial air-blast atomizer. *International journal of spray and combustion dynamics*, 10(3):211–230.

[141] Labourasse, E., Lacanette, D., Toutant, A., Lubin, P., Vincent, S., Lebaigue, O., Caltagirone, J.-P., and Sagaut, P. (2007). Towards large eddy simulation of isothermal two-phase flows: Governing equations and a priori tests. *International journal of multiphase flow*, 33(1):1–39.

[142] Lasheras, J., Villermaux, E., and Hopfinger, E. (1998). Break-up and atomization of a round water jet by a high-speed annular air jet. *Journal of Fluid Mechanics*, 357:351–379.

[143] Lasheras, J. C. and Hopfinger, E. (2000). Liquid jet instability and atomization in a coaxial gas stream. *Annual review of fluid mechanics*, 32(1):275–308.

[144] Lebas, R., Menard, T., Beau, P.-A., Berlemont, A., and Demoulin, F.-X. (2009). Numerical simulation of primary break-up and atomization: DNS and modelling study. *International Journal of Multiphase Flow*, 35(3):247–260.

[145] Lee, S., Lele, S. K., and Moin, P. (1992). Simulation of spatially evolving turbulence and the applicability of taylor's hypothesis in compressible flow. *Physics of Fluids A: Fluid Dynamics*, 4(7):1521–1530.

[146] Lee, T.-W. and Mitrovic, A. (1996). Liquid core structure of pressure-atomized sprays via laser tomographic imaging. *Atomization and Sprays*, 6(1).

[147] Lefebvre, A. H. and McDonell, V. G. (2017). *Atomization and sprays*. CRC press.

[148] Lhuillier, D. (2003). A mean-field description of two-phase flows with phase changes. *International Journal of Multiphase Flow*, 29(3):511–525.

[149] Lilly, K. (1966). The representation of small-scale turbulence in numerical simulation experiments.

[150] Lin, S. P. and Reitz, R. D. (1998). Drop and spray formation from a liquid jet. *Annual review of fluid mechanics*, 30(1):85–105.

[151] Liu, A., Sun, D., Yu, B., Wei, J., and Cao, Z. (2021). An adaptive coupled volume-of-fluid and level set method based on unstructured grids. *Physics of Fluids*, 33(1):012102.

[152] Lopez, J., Hernandez, J., Gomez, P., and Faura, F. (2005). An improved plic-vof method for tracking thin fluid structures in incompressible two-phase flows. *Journal of Computational Physics*, 208(1):51–74.

[153] Lowe, A., Kourmatzis, A., and Masri, A. R. (2017). Turbulent spray flames of intermediate density: Stability and near-field structure. *Combustion and Flame*, 176:511–520.

[154] Lund, T. S., Wu, X., and Squires, K. D. (1998). Generation of turbulent inflow data for spatially-developing boundary layer simulations. *Journal of computational physics*, 140(2):233–258.

[155] Luo, J., Hu, X., and Adams, N. A. (2015). A conservative sharp interface method for incompressible multiphase flows. *Journal of Computational Physics*, 284:547–565.

[156] Luret, G., Menard, T., Berlemont, A., Reveillon, J., Demoulin, F.-X., and Blokkeel, G. (2010). Modeling collision outcome in moderately dense sprays. *Atomization and Sprays*, 20(3).

[157] Mädler, L., Kammler, H., Mueller, R., and Pratsinis, S. E. (2002). Controlled synthesis of nanostructured particles by flame spray pyrolysis. *Journal of Aerosol Science*, 33(2):369–389.

[158] Maitre, E. (2006). Review of numerical methods for free interfaces. *Les Houches*, 27:31.

[159] Mansour, A. and Chigier, N. (1991). Dynamic behavior of liquid sheets. *Physics of Fluids A: Fluid Dynamics*, 3(12):2971–2980.

[160] Marble, F. E. and Broadwell, J. E. (1977). The coherent flame model for turbulent chemical reactions. Technical report, PURDUE UNIV LAFAYETTE IN PROJECT SQUIDHEADQUARTERS.

[161] Marle, C. (1982). On macroscopic equations governing multiphase flow with diffusion and chemical reactions in porous media. *International Journal of Engineering Science*, 20(5):643–662.

[162] Marmottant, P. and Villermaux, E. (2004). On spray formation. *Journal of fluid mechanics*, 498:73.

[163] Márquez Damián, S. (2013). An extended mixture model for the simultaneous treatment of short and long scale interfaces.

[164] Maury, B. and Pironneau, O. (1996). Characteristics ale method for unsteady free surface flows with surface tension. *Zeitschrift für angewandte Mathematik und Mechanik*, 76:613–614.

[165] Maz'ya, V. (2013). *Sobolev spaces*. Springer.

[166] McCarthy, M. and Molloy, N. (1974). Review of stability of liquid jets and the influence of nozzle design. *The Chemical Engineering Journal*, 7(1):1–20.

[167] McKee, S., Tomé, M. F., Ferreira, V. G., Cuminato, J. A., Castelo, A., Sousa, F., and Mangiavacchi, N. (2008). The mac method. *Computers & Fluids*, 37(8):907–930.

[168] McKinley, G. H. (2005). Dimensionless groups for understanding free surface flows of complex fluids.

[169] Melton, L. A. and Verdieck, J. F. (1985). Vapor/liquid visualization in fuel sprays. In *Symposium (International) on Combustion*, volume 20, pages 1283–1290. Elsevier.

[170] Ménard, T., Tanguy, S., and Berlemont, A. (2007). Coupling level set/VOF/ghost fluid methods: Validation and application to 3D simulation of the primary break-up of a liquid jet. *International Journal of Multiphase Flow*, 33(5):510–524.

[171] Mirjalili, S., Ivey, C. B., and Mani, A. (2020). A conservative diffuse interface method for two-phase flows with provable boundedness properties. *Journal of Computational Physics*, 401:109006.

[172] Mirjalili, S., Jain, S. S., and Dodd, M. (2017). Interface-capturing methods for two-phase flows: An overview and recent developments. *Center for Turbulence Research Annual Research Briefs*, 2017(117-135):13.

[173] Monaghan, J. J. (1988). An introduction to sph. *Computer physics communications*, 48(1):89–96.

[174] Monaghan, J. J. (1992). Smoothed particle hydrodynamics. *Annual review of astronomy and astrophysics*, 30(1):543–574.

[175] Monaghan, J. J. (2005). Smoothed particle hydrodynamics. *Reports on progress in physics*, 68(8):1703.

[176] Monaghan, J. J. and Gingold, R. A. (1983). Shock simulation by the particle method sph. *Journal of computational physics*, 52(2):374–389.

[177] Montazeri, H., Bussmann, M., and Mostaghimi, J. (2012). Accurate implementation of forcing terms for two-phase flows into simple algorithm. *International journal of multiphase flow*, 45:40–52.

[178] Montazeri, H. and Ward, C. (2014). A balanced-force algorithm for two-phase flows. *Journal of Computational Physics*, 257:645–669.

[179] Montazeri, H. and Zandavi, S. H. (2018). Derivative of heaviside step function vs. delta function in continuum surface force (csf) models. *International Journal of Multiphase Flow*, 100:196–199.

[180] Morel, C. (2007). On the surface equations in two-phase flows and reacting single-phase flows. *International Journal of Multiphase Flow*, 33(10):1045–1073.

[181] Movaghar, A., Linne, M., Herrmann, M., Kerstein, A. R., and Oevermann, M. (2018). Modeling and numerical study of primary breakup under diesel conditions. *International Journal of Multiphase Flow*, 98:110–119.

[182] Muliadi, A. R. and Sojka, P. E. (2012). Spatially resolved characteristics of pharmaceutical sprays. *AIChE journal*, 58(9):2920–2935.

[183] Mustata, R., Valiño, L., Jiménez, C., Jones, W., and Bondi, S. (2006). A probability density function eulerian monte carlo field method for large eddy simulations: Application to a turbulent piloted methane/air diffusion flame (sandia d). *Combustion and Flame*, 145(1-2):88–104.

[184] Navarro-Martinez, S. (2014). Large eddy simulation of spray atomization with a probability density function method. *International Journal of Multiphase Flow*, 63:11–22.

[185] Noh, W. F. and Woodward, P. (1976). Slic (simple line interface calculation). In *Proceedings of the fifth international conference on numerical methods in fluid dynamics June 28–July 2, 1976 Twente University, Enschede*, pages 330–340. Springer.

[186] Okamoto, T. and Kawahara, M. (1990). Two-dimensional sloshing analysis by lagrangian finite element method. *International Journal for Numerical Methods in Fluids*, 11(5):453–477.

[187] Okulan, N., Henderson, H., and Ahn, C. (1998). A new pulsed-mode micromachined flow sensor for an integrated microfluidic system. In *Proceedings of the Solid State Sensor and Actuator Workshop*, pages 7–11.

[188] Olsson, E. and Kreiss, G. (2005). A conservative level set method for two phase flow. *Journal of computational physics*, 210(1):225–246.

[189] Phillips, T., Derlaga, J., and Roy, C. (2012). Numerical benchmark solutions for laminar and turbulent flows. In *42nd AIAA Fluid Dynamics Conference and Exhibit*, page 3074.

[190] Phinney, R. E. (1973). The breakup of a turbulent liquid jet in a gaseous atmosphere. *Journal of Fluid Mechanics*, 60(4):689–701.

[191] Pilch, M. and Erdman, C. (1987). Use of breakup time data and velocity history data to predict the maximum size of stable fragments for acceleration-induced breakup of a liquid drop. *International journal of multiphase flow*, 13(6):741–757.

[192] Pilliod, J. E. (1992). *An analysis of piecewise linear interface reconstruction algorithms for volume-of-fluid methods*. U. of Calif., Davis.

[193] Pilliod Jr, J. E. and Puckett, E. G. (2004). Second-order accurate volume-of-fluid algorithms for tracking material interfaces. *Journal of Computational Physics*, 199(2):465–502.

[194] Pope, S. (1981). Monte carlo calculations of premixed turbulent flames. In *Symposium (International) on Combustion*, volume 18, pages 1001–1010. Elsevier.

[195] Pope, S. (1988). The evolution of surfaces in turbulence. *International journal of engineering science*, 26(5):445–469.

[196] Pope, S. B. (1985). Pdf methods for turbulent reactive flows. *Progress in energy and combustion science*, 11(2):119–192.

[197] Pringuey, T. and Cant, R. (2010). *High order schemes on 3D mixed-element unstructured meshes*. University of Cambridge, Department of Engineering.

[198] Pringuey, T. and Cant, R. S. (2012). High order schemes on three-dimensional general polyhedral meshes—application to the level set method. *Communications in Computational Physics*, 12(1):1–41.

[199] Pringuey, T. and Cant, R. S. (2014). Robust conservative level set method for 3d mixed-element meshes—application to les of primary liquid-sheet breakup. *Communications in Computational Physics*, 16(2):403–439.

[200] Puckett, E. and Saltzman, J. (1992). A 3d adaptive mesh refinement algorithm for multimaterial gas dynamics. *Physica D: Nonlinear Phenomena*, 60(1-4):84–93.

[201] Puckett, E. G., Almgren, A. S., Bell, J. B., Marcus, D. L., and Rider, W. J. (1997). A high-order projection method for tracking fluid interfaces in variable density incompressible flows. *Journal of computational physics*, 130(2):269–282.

[202] Raees, F., Van der Heul, D., and Vuik, C. (2011). Evaluation of the interface-capturing algorithm of OpenFoam for the simulation of incompressible immiscible two-phase flow. *Reports of the Department of Applied Mathematical Analysis, 11-07*.

[203] Raeini, A. Q., Blunt, M. J., and Bijeljic, B. (2012). Modelling two-phase flow in porous media at the pore scale using the volume-of-fluid method. *Journal of Computational Physics*, 231(17):5653–5668.

[204] Ramaswamy, B. and Kawahara, M. (1986). Arbitrary lagrangian-eulerian finite element method for the analysis of free surface fluid flows. *Computational Mechanics*, 1:103–108.

[205] Ramshaw, J. D. and Trapp, J. A. (1976). A numerical technique for low-speed homogeneous two-phase flow with sharp interfaces. *Journal of Computational Physics*, 21(4):438–453.

[206] Raynal, L. (1997). *Instabilité et entraînement à l'interface d'une couche de mélange liquide-gaz*. PhD thesis, Grenoble 1.

[207] Rehab, H. (1997). *Structure de l'écoulement et mélange dans le champ proche des jets coaxiaux*. PhD thesis, Grenoble 1.

[208] Rehab, H., Villermaux, E., and Hopfinger, E. (1997). Flow regimes of large-velocity-ratio coaxial jets. *Journal of Fluid Mechanics*, 345:357–381.

[209] Reitz, R. and Bracco, F. (1982). Mechanism of atomization of a liquid jet. *The physics of Fluids*, 25(10):1730–1742.

[210] Renardy, Y. and Renardy, M. (2002). Prost: a parabolic reconstruction of surface tension for the volume-of-fluid method. *Journal of computational physics*, 183(2):400–421.

[211] Rider, W. J. and Kothe, D. B. (1998). Reconstructing volume tracking. *Journal of computational physics*, 141(2):112–152.

[212] Roache, P. J. (2009). *Fundamentals of verification and validation*. hermosa publ.

[213] Roenby, J., Bredmose, H., and Jasak, H. (2016). A computational method for sharp interface advection. *Royal Society open science*, 3(11):160405.

[214] Rudman, M. (1997). Volume-tracking methods for interfacial flow calculations. *International journal for numerical methods in fluids*, 24(7):671–691.

[215] Ruschak, K. J. (1980). A method for incorporating free boundaries with surface tension in finite element fluid-flow simulators. *International Journal for Numerical Methods in Engineering*, 15(5):639–648.

[216] Russo, G. and Smereka, P. (2000). A remark on computing distance functions. *Journal of computational physics*, 163(1):51–67.

[217] Sabel'nikov, V. and Soulard, O. (2005). Rapidly decorrelating velocity-field model as a tool for solving one-point fokker-planck equations for probability density functions of turbulent reactive scalars. *Physical Review E*, 72(1):016301.

[218] Sackinger, P. A., Schunk, P. R., and Rao, R. R. (1996). A newton–raphson pseudo-solid domain mapping technique for free and moving boundary problems: a finite element implementation. *Journal of computational physics*, 125(1):83–103.

[219] Saito, H. and Scriven, L. (1981). Study of coating flow by the finite element method. *Journal of Computational Physics*, 42(1):53–76.

[220] Sallam, K., Dai, Z., and Faeth, G. (2002). Liquid breakup at the surface of turbulent round liquid jets in still gases. *International Journal of Multiphase Flow*, 28(3):427–449.

[221] Sallam, K. and Faeth, G. (2003). Surface properties during primary breakup of turbulent liquid jets in still air. *AIAA journal*, 41(8):1514–1524.

[222] Sarwar, M., Cleary, M., Moinuddin, K., and Thorpe, G. (2017). On linking the filter width to the boundary layer thickness in explicitly filtered large eddy simulations of wall bounded flows. *International Journal of Heat and Fluid Flow*, 65:73–89.

[223] Scardovelli, R. and Zaleski, S. (1999). Direct numerical simulation of free-surface and interfacial flow. *Annual review of fluid mechanics*, 31(1):567–603.

[224] Scardovelli, R. and Zaleski, S. (2003). Interface reconstruction with least-square fit and split eulerian–lagrangian advection. *International Journal for Numerical Methods in Fluids*, 41(3):251–274.

[225] Schmidt, H. and Schumann, U. (1989). Coherent structure of the convective boundary layer derived from large-eddy simulations. *Journal of Fluid Mechanics*, 200:511–562.

[226] Sethian, J. A. (1996a). A fast marching level set method for monotonically advancing fronts. *Proceedings of the National Academy of Sciences*, 93(4):1591–1595.

[227] Sethian, J. A. (1996b). Theory, algorithms, and applications of level set methods for propagating interfaces. *Acta numerica*, 5:309–395.

[228] Sethian, J. A. (1999). *Level set methods and fast marching methods: evolving interfaces in computational geometry, fluid mechanics, computer vision, and materials science*, volume 3. Cambridge university press.

[229] Sethian, J. A. and Smereka, P. (2003). Level set methods for fluid interfaces. *Annual review of fluid mechanics*, 35(1):341–372.

[230] Shinjo, J. and Umemura, A. (2010). Simulation of liquid jet primary breakup: Dynamics of ligament and droplet formation. *International Journal of Multiphase Flow*, 36(7):513–532.

[231] Shirani, E., Ghadiri, F., and Ahmadi, A. (2011). Modeling and simulation of interfacial turbulent flows.

[232] Shirani, E., Jafari, A., and Ashgriz, N. (2006). Turbulence models for flows with free surfaces and interfaces. *AIAA journal*, 44(7):1454–1462.

[233] Shopov, P. J., Minev, P. D., and Bazhlekov, I. B. (1992). Numerical method for unsteady viscous hydrodynamical problem with free boundaries. *International journal for numerical methods in fluids*, 14(6):681–705.

[234] Shyy, W., Udaykumar, H., Rao, M. M., and Smith, R. W. (2012). *Computational fluid dynamics with moving boundaries*. Courier Corporation.

[235] Singh, G., Kourmatzis, A., Gutteridge, A., and Masri, A. (2020a). Instability growth and fragment formation in air assisted atomization. *Journal of Fluid Mechanics*, 892.

[236] Singh, G., Kourmatzis, A., and Masri, A. (2020b). Volume measurement of atomizing fragments using image slicing. *Experimental Thermal and Fluid Science*, page 110102.

[237] Smagorinsky, J. (1963). General circulation experiments with the primitive equations: I. The basic experiment. *Monthly weather review*, 91(3):99–164.

[238] Smallwood, G. J., Gülder, Ö. L., and Snelling, D. R. (1994). The structure of the dense core region in transient diesel sprays. In *Symposium (International) on Combustion*, volume 25, pages 371–379. Elsevier.

[239] Smith, J. N., Flagan, R. C., and Beauchamp, J. (2002). Droplet evaporation and discharge dynamics in electrospray ionization. *The Journal of Physical Chemistry A*, 106(42):9957–9967.

[240] Smolianski, A. (2001). *Numerical modeling of two-fluid interfacial flows*. University of Jyväskylä.

[241] Sochnikov, V. and Efrima, S. (2003). Level set calculations of the evolution of boundaries on a dynamically adaptive grid. *International Journal for Numerical Methods in Engineering*, 56(13):1913–1929.

[242] Srinivasan, V., Salazar, A. J., and Saito, K. (2008). Numerical investigation on the disintegration of round turbulent liquid jets using les/vof techniques. *Atomization and Sprays*, 18(7).

[243] Stahl, M., Damaschke, N., and Tropea, C. (2006). Experimental investigation of turbulence and cavitation inside a pressure atomizer and optical characterization of the generated spray. *ICLASS-2006, Aug.*

[244] Stahl, M., Gnirß, M., Damaschke, N., and Tropea, C. (2005). Laser doppler measurements of nozzle flow and optical characterisation of the generated spray. *ILASS-2005, Orleans, France.*

[245] Stanley, S. and Sarkar, S. (2000). Influence of nozzle conditions and discrete forcing on turbulent planar jets. *AIAA journal*, 38(9):1615–1623.

[246] Strain, J. (1999). Tree methods for moving interfaces. *Journal of Computational Physics*, 151(2):616–648.

[247] Strobel, R. and Pratsinis, S. E. (2007). Flame aerosol synthesis of smart nanostructured materials. *Journal of Materials Chemistry*, 17(45):4743–4756.

[248] Sussman, M., Fatemi, E., Smereka, P., and Osher, S. (1998). An improved level set method for incompressible two-phase flows. *Computers & Fluids*, 27(5-6):663–680.

[249] Sussman, M. and Puckett, E. G. (2000). A coupled level set and volume-of-fluid method for computing 3d and axisymmetric incompressible two-phase flows. *Journal of computational physics*, 162(2):301–337.

[250] Sussman, M. and Smereka, P. (1997). Axisymmetric free boundary problems. *Journal of Fluid Mechanics*, 341:269–294.

[251] Sussman, M., Smereka, P., and Osher, S. (1994). A level set approach for computing solutions to incompressible two-phase flow. *Journal of Computational physics*, 114(1):146–159.

[252] Sussman, M., Smith, K. M., Hussaini, M. Y., Ohta, M., and Zhi-Wei, R. (2007). A sharp interface method for incompressible two-phase flows. *Journal of computational physics*, 221(2):469–505.

[253] Tezduyar, T. E., Behr, M., Mittal, S., and Liou, J. (1992a). A new strategy for finite element computations involving moving boundaries and interfaces—the deforming-spatial-domain/space-time procedure: Ii. computation of free-surface flows, two-liquid flows, and flows with drifting cylinders. *Computer methods in applied mechanics and engineering*, 94(3):353–371.

[254] Tezduyar, T. E., Behr, M., Mittal, S., and Liou, J. (1992b). A new strategy for finite element computations involving moving boundaries and interfaces—the deforming-spatial-domain/space-time procedure: Ii. computation of free-surface flows, two-liquid flows, and flows with drifting cylinders. *Computer methods in applied mechanics and engineering*, 94(3):353–371.

[255] Tornberg, A.-K. and Engquist, B. (2000). A finite element based level-set method for multiphase flow applications. *Computing and Visualization in Science*, 3(1):93–101.

[256] Tretola, G., Navarro-Martinez, S., and Vogiatzaki, K. (2022). Primary break-up characterisation and droplet statistics of multi-hole sprays using a probabilistic surface density methodology. *International Journal of Multiphase Flow*, 152:104039.

[257] Tretola, G., Vogiatzaki, K., and Navarro-Martinez, S. (2021). Implementation of a probabilistic surface density volume of fluid approach for spray atomisation. *Computers & Fluids*, 230:105121.

[258] Tryggvason, G., Bunner, B., Esmaeeli, A., Juric, D., Al-Rawahi, N., Tauber, W., Han, J., Nas, S., and Jan, Y.-J. (2001). A front-tracking method for the computations of multiphase flow. *Journal of computational physics*, 169(2):708–759.

[259] Tryggvason, G., Scardovelli, R., and Zaleski, S. (2011). *Direct numerical simulations of gas–liquid multiphase flows*. Cambridge University Press.

[260] Ubbink, O. and Issa, R. (1999). A method for capturing sharp fluid interfaces on arbitrary meshes. *Journal of computational physics*, 153(1):26–50.

[261] Unverdi, S. O. and Tryggvason, G. (1992). A front-tracking method for viscous, incompressible, multi-fluid flows. *Journal of computational physics*, 100(1):25–37.

[262] Valino, L. (1998). A field monte carlo formulation for calculating the probability density function of a single scalar in a turbulent flow. *Flow, turbulence and combustion*, 60(2):157–172.

[263] Vallet, A. and Borghi, R. (1999). Modélisation eulerienne de l'atomisation d'un jet liquide. *Comptes Rendus de l'Académie des Sciences-Series IIB-Mechanics-Physics-Astronomy*, 327(10):1015–1020.

[264] Van Wachem, B. and Schouten, J. (2002). Experimental validation of 3-d lagrangian vof model: Bubble shape and rise velocity. *AIChE journal*, 48(12):2744–2753.

[265] Varga, C. M. (2002). *Atomization of a small-diameter liquid jet by a high-speed gas stream*. University of California, San Diego.

[266] Varga, C. M., Lasheras, J. C., and Hopfinger, E. J. (2003). Initial breakup of a small-diameter liquid jet by a high-speed gas stream. *Journal of Fluid Mechanics*, 497:405–434.

[267] Versteeg, H. K. and Malalasekera, W. (2007). *An introduction to computational fluid dynamics: the finite volume method*. Pearson education.

[268] Vervisch, L., Bidaux, E., Bray, K., and Kollmann, W. (1995). Surface density function in premixed turbulent combustion modeling, similarities between probability density function and flame surface approaches. *Physics of Fluids*, 7(10):2496–2503.

[269] Vincent, S., Caltagirone, J.-P., Lubin, P., and Randrianarivelo, T. N. (2004). An adaptative augmented lagrangian method for three-dimensional multimaterial flows. *Computers & fluids*, 33(10):1273–1289.

[270] Wang, B., Cleary, M., and Masri, A. (2021). Modeling of interfacial flows based on an explicit volume diffusion concept. *Physics of Fluids*, 33(6):062111.

[271] Wang, Y., Liu, X., Im, K.-S., Lee, W.-K., Wang, J., Fezzaa, K., Hung, D. L., and Winkelman, J. R. (2008). Ultrafast X-ray study of dense-liquid-jet flow dynamics using structure-tracking velocimetry. *Nature Physics*, 4(4):305–309.

[272] Weller, H. G. (2008). A new approach to VOF-based interface capturing methods for incompressible and compressible flow. *OpenCFD Ltd., Report TR/HGW*, 4.

[273] Wilcox, D. C. et al. (1998). *Turbulence modeling for CFD*, volume 2. DCW industries La Canada, CA.

[274] Wu, P.-K., Miranda, R., and Faeth, G. (1995). Effects of initial flow conditions on primary breakup of nonturbulent and turbulent round liquid jets. *Atomization and sprays*, 5(2).

[275] Xiao, F., Dianat, M., and McGuirk, J. J. (2014). LES of turbulent liquid jet primary breakup in turbulent coaxial air flow. *International Journal of Multiphase Flow*, 60:103–118.

[276] Xiao, F., Ii, S., and Chen, C. (2011). Revisit to the thinc scheme: a simple algebraic vof algorithm. *Journal of Computational Physics*, 230(19):7086–7092.

[277] Yamamoto, K. and Kawahara, M. (1998). Free surface analysis based on ale finite element method(arbitrary lagrangian-eulerian). In *International Conference on Finite Elements in Fluids, 10 th, Tucson, AZ*, pages 64–69.

[278] Yecko, P. and Zaleski, S. (2005). Transient growth in two-phase mixing layers. *Journal of fluid mechanics*, 528:43–52.

[279] Youngs, D. L. (1982). Time-dependent multi-material flow with large fluid distortion. *Numerical methods for fluid dynamics*.

[280] Youngs, D. L. (1984). An interface tracking method for a 3d eulerian hydrodynamics code. *Atomic Weapons Research Establishment (AWRE) Technical Report*, 44(92):35.

[281] Zalesak, S. T. (1979). Fully multidimensional flux-corrected transport algorithms for fluids. *Journal of Computational Physics*, 31(3):335–362.

[282] Zhang, T., Wu, J., and Lin, X. (2019). An interface-compressed diffuse interface method and its application for multiphase flows. *Physics of Fluids*, 31(12):122102.

[283] Zhang, W. and Ahn, C. H. (1996). A microfabricated planar magnetic particle separator with optically inspectable flow channel. In *Proceedings of 18th Annual International Conference of the IEEE Engineering in Medicine and Biology Society*, volume 1, pages 252–253. IEEE.

[284] Zhao, H. (2005). A fast sweeping method for eikonal equations. *Mathematics of computation*, 74(250):603–627.

[285] Zhao, L., Khuc, H., Mao, J., Liu, X., and Avital, E. (2018). One-layer particle level set method. *Computers & Fluids*, 170:141–156.

[286] Zuzio, D., Estivalezes, J.-L., Villedieu, P., and Blanchard, G. (2013). Numerical simulation of primary and secondary atomization. *Comptes Rendus Mécanique*, 341(1-2):15–25.